Title

Characterizing the Dynamic Interactions of Biological and Biologically-Inspired Surfaces and Interfaces

Author

Cadirov, Nicholas

Publication Date

2017

UNIVERSITY OF CALIFORNIA

Santa Barbara

Characterizing the Dynamic Interactions of Biological and Biologically-Inspired Surfaces and Interfaces

A dissertation submitted in partial satisfaction of the
requirements for the degree Doctor of Philosophy
in Chemical Engineering

by

Nicholas Anthony Cadirov

Committee in charge:
Professor Jacob N. Israelachvili, Chair
Professor Kimberly L. Foster
Professor Matthew E. Helgeson
Professor Samir Mitragotri

January 2018

The dissertation of Nicholas Anthony Cadirov is approved.

Professor Kimberly L. Foster

Professor Matthew E. Helgeson

Professor Samir Mitragotri

Professor Jacob N. Israelachvili, Committee Chair

December 2017

Characterizing the Dynamic Interactions of Biological and Biologically-Inspired Surfaces and Interfaces

by

Nicholas Anthony Cadirov

ACKNOWLEDGEMENTS

The success of my research and personal growth have been influenced by the guidance, support, and friendship of many people. I would first and foremost like to thank my advisor, Prof. Jacob Israelachvili. It has been an honor to work with and learn from such an intelligent and supportive scientist who applies the perfect balance of seriousness and humor in the lab. I would also like to thank my committee members, Prof. Kimberly Foster, Prof. Matthew Helgeson, and Prof. Samir Mitragotri, for their continued support and interest in my research as well as learning directly from Kimberly and Matt through collaborations with their labs.

I couldn't have made it through graduate school without the guidance of many past lab members. I owe a huge thank you to my lunch buddy and mentor Prof. Dong-Woog Lee for introducing me to Korean food and really taking me under his wing as a young graduate student. I can't forget my other past mentors and friends including Dr. Mike Rapp, Dr. Matt Gebbie, Dr. Steve Donaldson, Prof. Xavier Banquy, Dr. Saurabh Das, Prof. Yair Kaufman, Prof. Himanshu Mishra, and Dr. Nadine Martinez. My current lab mates and collaborators have kept me energized and excited every day including Dr. Alex Schrader, Dr. Kai Kristiansen, Jamie Booth, Sandy Chen, Tom Cristiani, George Degen, Howie Dobbs, Zach Berkson, DJ Seo, and Roberto Andresen Eguiluz.

I was able to surround myself with great friends that helped keep me motivated and balanced throughout my graduate career. Thank you to Doug for always being willing to go for an early morning surf session, Geoff for enjoying two of my favorite passions with me (sports and food), and John for introducing me to the world of craft beer. I am also so thankful for Kelsey for her support, encouragement, patience, and for all the adventures we have been on together these past five years.

Finally, I would like to thank my parents and my twin sister Chelsea for their continuous support and love and for working tirelessly to give me the opportunities to make it possible to earn a PhD. You have been my greatest inspiration for hard work and dedication and I sincerely owe my personal and academic growth and success to you.

VITAE OF NICHOLAS ANTHONY CADIROV

December 2017

EDUCATION

University of California Santa Barbara (UCSB), Santa Barbara, California
Ph.D. in Chemical Engineering 2012-2017
Specialization in Dynamic Interfacial Phenomena
Advisor: Professor Jacob N. Israelachvili

University of Massachusetts Amherst (UMass), Amherst, Massachusetts
B.S. in Chemical Engineering, 2008-1012
Summa Cum Laude, Departmental Honors, Biochemical Engineering Concentration

RESEARCH EXPERIENCE

Doctoral Research: Chemical Engineering, UCSB, 2012-2017
Advisor: Professor Jacob N. Israelachvili

- Versatile Gecko-Inspired Adhesive Design: Led a collaboration with mechanical and electrical engineers that influenced the design of more versatile gecko-mimetic adhesives for climbing robotics applications by testing and characterizing adhesive interactions in real-world environments
- Multi-functional Oil Lubricant Additive (Collaboration with Mitsubishi Chemical Company): Designed and characterized a multi-functional molecule additive that improves engine oil lubricity and temperature stability with a team of polymer chemists and rheologists
- Characterizing the Interfacial Properties of Skincare Products and Hair (Collaborations with P&G): Developed equipment and analyses to quantify thin film properties of skin creams and moisturizers as well as determine friction and adhesion behavior between single hair fibers
- Direct Visualization of Lipid Membrane Hemifusion: Created a device that resulted in direct visualization and force measurement during membrane hemifusion which has furthered the understanding of cell-cell interactions
- Lubrication Properties of Hyaluronic Acid (HA) in Model Joint (Cartilage) Systems: Investigated wear and boundary lubrication properties of different molecular weight HA to determine new arthritis treatments

Undergraduate Research: Chemical Engineering, UMass, 2010-2012
Advisor: Professor Susan Roberts

- Utilized sterile technique and hemocytometry to characterize the growth of single cell suspensions of Taxus cells
- Established a method for reculturing protoplasts in plant cell culture to study heterogeneity in production of the anti-cancer agent paclitaxel

Research Internships in Science and Engineering: Chemical Engineering, UCSB, Summer 2011

Advisor: Professor Jacob Israelachvili

- Developed a method for imaging modeled myelin sheaths utilizing Langmuir-Blodgett technique and fluorescence microscopy
- Discovered differences in lipid domains between models of healthy and diseased myelin

Research Experience for Undergraduates: Chemical Engineering, USC, Summer 2010

Advisor: Professor Branko Popov

- Synthesized and characterized titanium dioxide-supported catalysts for the oxygen reduction reaction in polymer electrolyte membrane fuel cells
- 1st place prize in Research Symposium oral presentation competition

FELLOWSHIPS & AWARDS

Art of Science People's Choice Award (UCSB), 2015
Heslin Fellowship (UCSB), 2012
Commonwealth Honors College Recognition Award (UMass), 2011
Chemical Engineering Endowment Scholarship (UMass), 2011-2012
John and Abigail Adams Scholarship (UMass), 2008-2012

TEACHING EXPERIENCE

Teaching Assistant: Introduction to Thermodynamics, UCSB, 2016

- Held office hours and prepared homework solutions
- Presented a full lesson to the class

Teaching Assistant: Chemical Engineering Undergraduate Laboratory, UCSB, 2014

- Instructed and supervised students during distillation lab experiments

Teaching Assistant: Colloids, Biomolecules, and Biosurfaces, UCSB, 2014

- Held office hours and assisted students on homework assignments

OUTREACH & OTHER ORGANIZATIONS

UCSB Chemical Engineering Graduate Student Association, UCSB, 2017

- Helped with organizing and giving senior input on events to foster departmental community and professional development

9th Annual Clorox-Amgen Graduate Student Symposium, UCSB, 2016

- Organizing committee member

ScienceLine "Ask a Scientist": Materials Research Lab, UCSB, 2014-2017

- Answer weekly questions from local K-12 students and teachers about science and engineering related topics

PUBLICATIONS

1. *Effects of Salinity on Oil Recovery (the "Dilution Effect"): Experimental and Theoretical Studies of Crude Oil/Brine/Carbonate Surface Restructuring and Associated Physiochemical Interactions.* Chen, SY; Kaufman, Y; Kristiansen, K; Seo, DJ; Schrader, AM; Alotaibi, MB; Dobbs, HA; **Cadirov, N**; Boles, JR; Ayirala, SC; Israelachvili, J; Yousef, A; (2017) ***Energy & Fuels*** DOI: 10.102/acs.energyfuels.7b00869
2. *Influence of Humidity on Grip and Release Adhesion Mechanisms for Gecko-Inspired Microfibrillar Surfaces.* **Cadirov, N**; Booth, JA; Turner, KL; Israelachvili, J; (2017) ***ACS Applied Materials & Interfaces*** DOI: 10.1021/acsami.7b01624
3. *Stick-slip friction of gecko-mimetic flaps on smooth and rough substrates.* Das, S*; **Cadirov, N* (co-1st author)**; Chary, S; Kaufman, Y; Hogan, J; Turner, K; Israelachvili, J; (2015) ***Journal of The Royal Society Interface*** DOI: 10.1098/rsif.2014.1346
4. *Real time intermembrane force measurements and imaging of lipid domain morphology during hemifusion.* Lee, DW; Kristiansen, K; Donaldson, SH; **Cadirov, N**; Banquy, X; Israelachvili, J; (2015) ***Nature Communications*** DOI: 10.1038/ncomms8238
5. *Effects of molecular weight of grafted hyaluronic acid on wear initiation.* Lee, DW; Banquy, X; Das, S; **Cadirov, N**; Jay, G; Israelachvili, J; (2014) ***Acta Biomaterialia*** 10 (5):1817-1823
6. *Development of supported bifunctional oxygen electrocatalysts with high performance for unitized regenerative fuel cell applications*. Huang, SY; Ganesan, P; Jung, WS; **Cadirov, N**; Popov, B; (2010) ***ECS Transactions*** 33 (1):1979-1987

PUBLICATIONS IN PREPARATION

1. *Characterizing dynamic, high-frequency friction components in thin complex-fluid lubricating films.* Cristiani, T*; **Cadirov, N* (co-1st author)**; Erhman, M; Jamadagni, SN; Scott, J; Kristiansen, K; Israelachvili, J;
2. *Designing and characterizing a triple-functional motor oil lubricant additive.* Zerdan, R; van Ravensteijn, B; Seo, DJ; **Cadirov, N**; Gerbec, J; Israelachvili, J; Hawker, C; Koga, S; Watanabe, T; Helgeson, M;
3. *Single fiber hair-hair friction and adhesion.* Cristiani, T*; **Cadirov, N* (co-1st author)**; Koenig, P; Kristiansen, K; Scott, J; Gizaw, Y; Meinert, K; Israelachvili, J;
4. *Physicochemical changes of carbonate surfaces in diluted seawater for improved oil recovery*. Chen, SY; Kristiansen, K; Seo, DJ; **Cadirov, N**; Alotaibi, MB; Dobbs, HA; Schrader, AM; Kaufman, Y; Boles, JR; Ayirala, SC; Yousef, A; Israelachvili, J;

PRESENTATIONS

1. Oral Presentation 2016 AICHE Annual Meeting, San Fransisco CA, Influence of humidity on gecko inspired adhesives
2. Oral Presentation 2016 Chemical Engineering Graduate Student Symposium, UCSB, Characterizing the surface interactions of gecko inspired adhesives on diversified substrates
3. Oral Presentation 2016 ACS Colloids and Interfacial Science Conference, Harvard University, MA, Influence of humidity on gecko inspired adhesives
4. Poster presentation 2015 Chemical Engineering Graduate Student Symposium, UCSB, Influence of humidity on gecko inspired adhesives
5. Poster presentation 2015 Gordon Conference Science of Adhesion, Mount Holyoke College, MA, Influence of humidity on gecko inspired adhesives
6. Poster presentation 2014 Chemical Engineering Graduate Student Symposium, UCSB, Stick-slip friction of gecko-mimetic structured surfaces on smooth and rough substrates
7. Poster presentation 2014 Surface Forces Apparatus Conference Cancun, Mexico, Stick-slip friction of gecko-mimetic structured surfaces on smooth and rough substrates

ABSTRACT

Characterizing the Dynamic Interactions of Biological and Biologically-Inspired Surfaces and Interfaces

by

Nicholas Anthony Cadirov

Most fundamental theories on interfacial interactions consist of equilibrium phenomena, yet many processes and interactions in practice occur outside of these equilibria in a dynamic state. This thesis explores how biological and biologically-inspired surfaces and interfaces interact with each other under dynamic conditions during adhesion, friction, and lubrication. Using a surface forces apparatus, new methodologies and analyses have been designed to study such dynamic interactions. This thesis takes a tour from fully dry systems, to humidified, lubricated, and finally fully submerged systems underwater.

The chapters are divided into unique systems including gecko-inspired adhesives (Chapter 2), complex moisturizing fluids (skin creams) (Chapter 3), and lipid membranes (Chapter 4). Chapter 2 investigates the frictional adhesion characteristics of microfibrillar gecko-mimetic adhesives in diverse environments. The discovery of the underlying mechanisms for attaining grip against rough surfaces and in humid conditions has led to new design principles for future gecko-mimetic adhesives.

Chapter 3 explores how to test for and quantify high frequency dynamic friction force components in a complex lubricating film of skin cream. The instrumentation and analysis methods can be applied to any such high-speed friction experiment to uncover and unambiguously differentiate stick-slip and oscillatory friction behavior in a diverse range of systems.

Lastly, Chapter 4 discusses the discovery of dynamic lipid membrane domain rearrangements during hemifusion. New instrumentation (Fluorescence Surface Forces Apparatus – FL-SFA) was developed to simultaneously measure the interfacial forces between apposing membranes and visualize *in situ* morphological changes occurring at the interface. This study discovered lipid rearrangements that occur in cell-cell interactions including cellular transport. The thesis concludes with the future potential of the newly developed FL-SFA device and technique.

TABLE OF CONTENTS

Chapter 1: Surface Interactions in Biological and Biologically Inspired Materials

Biological and biologically inspired materials and surfaces are complex and are involved in processes outside of equilibrium. Analyzing and understanding the interfacial phenomena involved in the interactions in these systems requires a clear consideration of the dynamic effects that occur in time and space, and how these govern overall system behaviors. This thesis aims to achieve fundamental understandings of complex interactions in adhesion, friction, and lubrication in systems ranging from gecko-mimetic adhesives (Chapter 2), to complex fluid lubrication between viscoelastic surfaces (Chapter 3), to lipid bilayer membranes (Chapter 4). The basic concepts and techniques used to characterize these phenomena are briefly described in this introduction and are further expanded upon in the subsequent chapters.

1.1 Adhesion

On a fundamental level, surfaces will attract or repel each other depending on the individual contributions from non-specific and specific interactions between atoms and molecules in the system. The root of all the intermolecular interactions emerges from electronic properties of atoms that act at a distance and can be divided into different molecular interactions such as van der Waals forces, electrostatic forces, hydrogen bonding, and hydrophobic forces[1]. Van der Waals forces involve the dipoles, polarizability, and dispersion forces between atoms, and electrostatic interactions are typically considered between charged species with Coulomb interactions. Collectively, van der Waals and electrostatic forces in a liquid medium are described by the DLVO theory (Derjaguin, Landau, Verwey, and Overbeek) which encapsulates the distance dependence of these colloidal forces[2,3]. Hydrogen bonding and hydrophobic forces are less fully understood at a fundamental level, but recent progress has been made in deriving a full interaction potential[4].

Capillary forces become present when a liquid bridge forms between two surfaces, giving rise to adhesive contributions from the Laplace pressure and surface tension and how the liquid interacts with each surface. The combination of van der Waals and capillary forces are discussed in detail in Chapter 2 in relation to the grip and release states of gecko-mimetic adhesives in humid environments. The capillary forces are dependent on the properties of the liquid as well as the hydrophilic/phobic nature of the surfaces. The surface structure of the adhesive is found to create a humidity dependence on the capillary force when the bridging asperities are on similar length scales as the capillary itself.

A full interaction potential between lipid membranes in solution is further discussed in Chapter 4 consisting of a full DLVO and hydrophobic interaction analysis. These forces dictate the equilibrium separation of membranes in solution, as well as the forces needed for bilayer fusion or hemifusion as occurs in processes such as membrane transport and other dynamic cellular interactions.

1.2 Friction and Lubrication

Friction forces are entirely different from typical force-distance laws between molecules and surfaces and only arise as a reaction to motion or other forces. On a molecular level, friction can be thought of as the force required to move a molecule from one lattice site to the next. This process involves a lateral force to initiate lateral motion as well as an additional force to break the adhesion between the molecule and lattice site. From a macroscopic view, surfaces must separate or dilate to slide past each other, and the force required to perform this motion is the friction force[5]. The dynamics of sliding and molecular collisions play a large role in the experienced friction of biological surfaces that are often chemically and physically complex. In Chapter 2 surface structure is found to effect how a gecko-mimetic adhesive grips and slides across a smooth or rough glass surface, resulting in load and velocity dependent stick-slip friction.

When shearing or sliding with a thin film or lubricant between surfaces, the ordering and confinement of molecules changes the resistance to shear by altering the local viscosity or the mobility of molecules trying to slide past each other[6]. This results in friction or lubrication behavior that can increase, decrease, or stay constant with increasing shear velocity. The Deborah number is commonly used to relate time scales of energy dissipation to characteristic time scales of molecular rearrangements and mobility[7]. Thin film lubrication is analyzed further in Chapter 3 with skin creams between soft skin-mimicking surfaces. A new analysis technique and instrumentation is implemented to decipher all frequency components of the friction force and differentiate surface effects from systematic resonant and oscillatory frequencies that may be detected in sensory perception.

1.3 Techniques: The Surface Forces Apparatus

The surface forces apparatus (SFA) is used to measure and analyze the dynamic behavior in each of the systems studied[8]. In the basic setup (Figure 1.1), the SFA measures the interaction forces (attractive or repulsive) between two surfaces as they are brought together and retracted. One of the surfaces is held by a double cantilever spring that deflects upon a force which can be measured using Hooke's Law, $F = k\Delta x$, where F is the force (mN),

k is the spring constant (mN*m), and Δx is the deflection of the spring (m)[9]. The surfaces can be positioned using piezoelectric elements for < 1 Angstrom control.

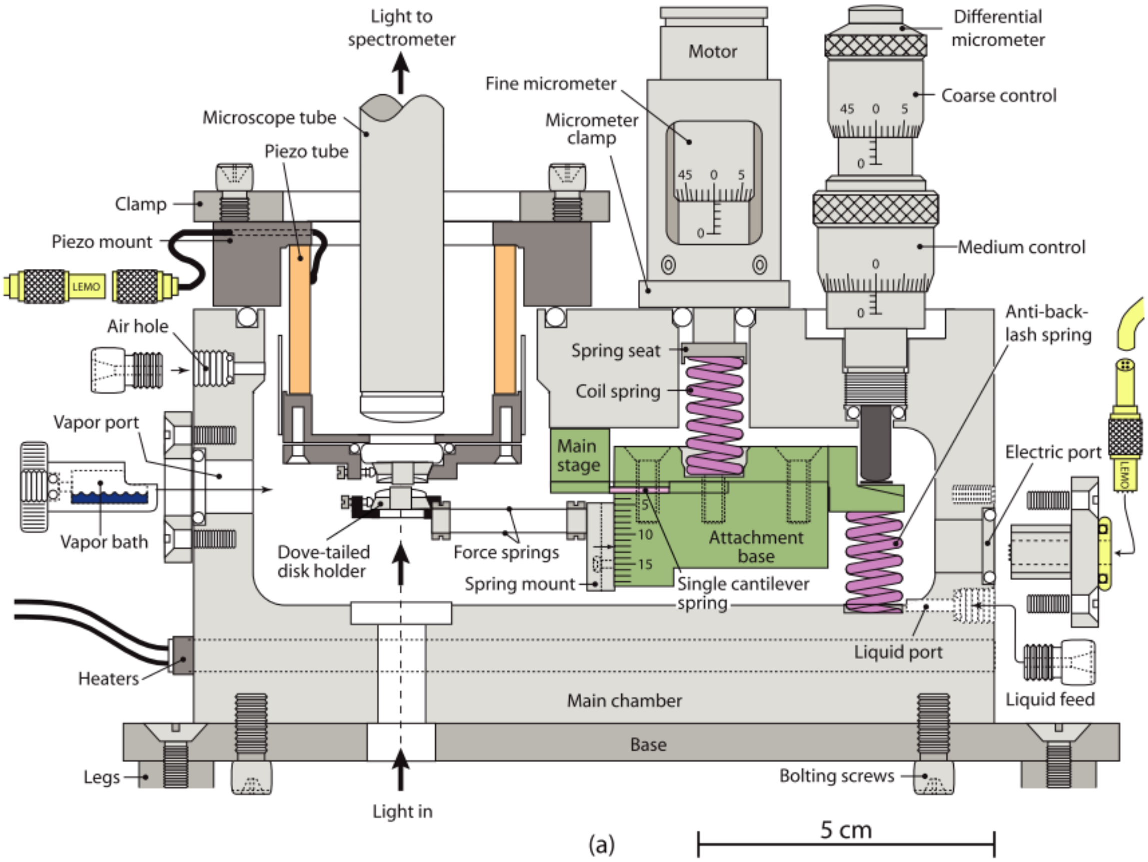

Figure 1.1 Front view of the surface forces apparatus (Adapted from Reference 8). The SFA contains many features for force measurements including positional control and spring architecture. Various ports are used to control the environment including temperature, vapor content, and humidity, as well as for electrical connections to positional elements or extra force measuring capabilities.

The surfaces typically have a semi-reflective layer that create an optical interferometer which can be used to calculate the absolute distance between the surfaces. White light passes through the surfaces where it reflects and then transmits an interference pattern into a spectrometer known as fringes of equal chromatic order (FECO) depicted in Figure 1.2[10]. The wavelengths of the fringes will shift as the surfaces are brought closer together or further apart, and can be analyzed to calculate the separation distance between the surfaces. This technique gives rise to distance measurements with Angstrom level resolution resulting in force resolution of 10^{-8} N. While depicting distances across the whole surface, the FECO technique can visualize the entire contact area and any surface deformations or film adsorption throughout an experiment.

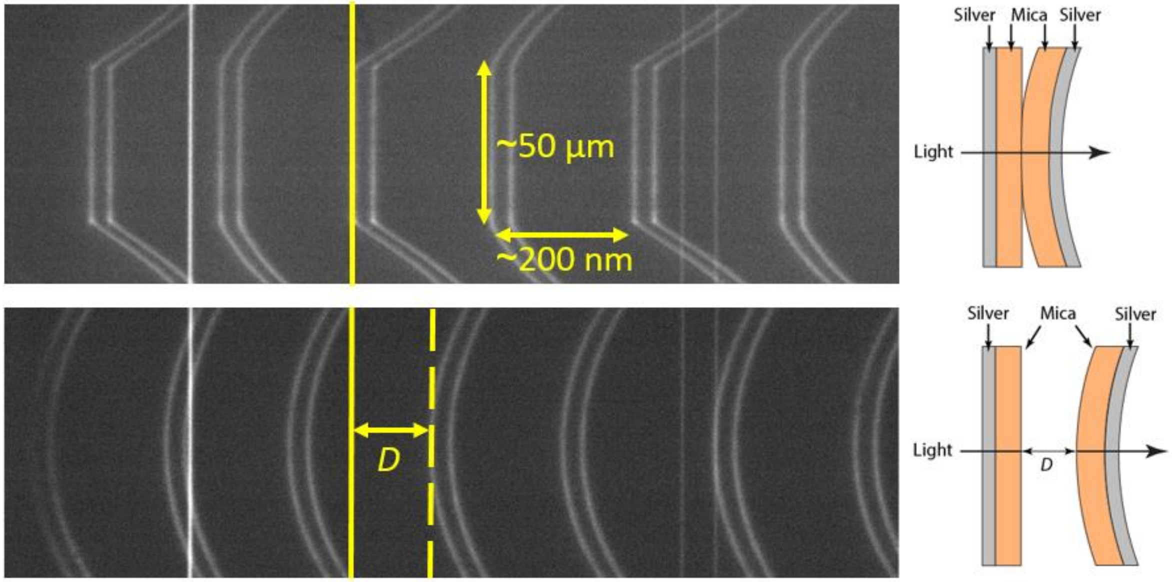

Figure 1.2 Multiple beam interferometry technique between two back-slivered mica surfaces, typical in the SFA. White light passes through the two surfaces creating an interference pattern that is projected into a spectrometer to produce fringes of equal chromatic order (FECO).

1.4 Additional SFA Capabilities and Instrumentation Development

The basic normal force measuring technique (adhesion and repulsion) has been expanded upon in multiple ways throughout this thesis. In cases where opaque surfaces are implemented that are unable to form an interferometer with light, strain gauges are employed on the cantilever springs to directly measure their deflection and thus the force. However, the resulting separation between the surfaces remains unknown in this setup. To measure friction forces, a bimorph slider is used to slide one surface back and forth laterally and is coupled with a special lateral force measuring top mount to hold the upper surface as shown in Figure 1.3.

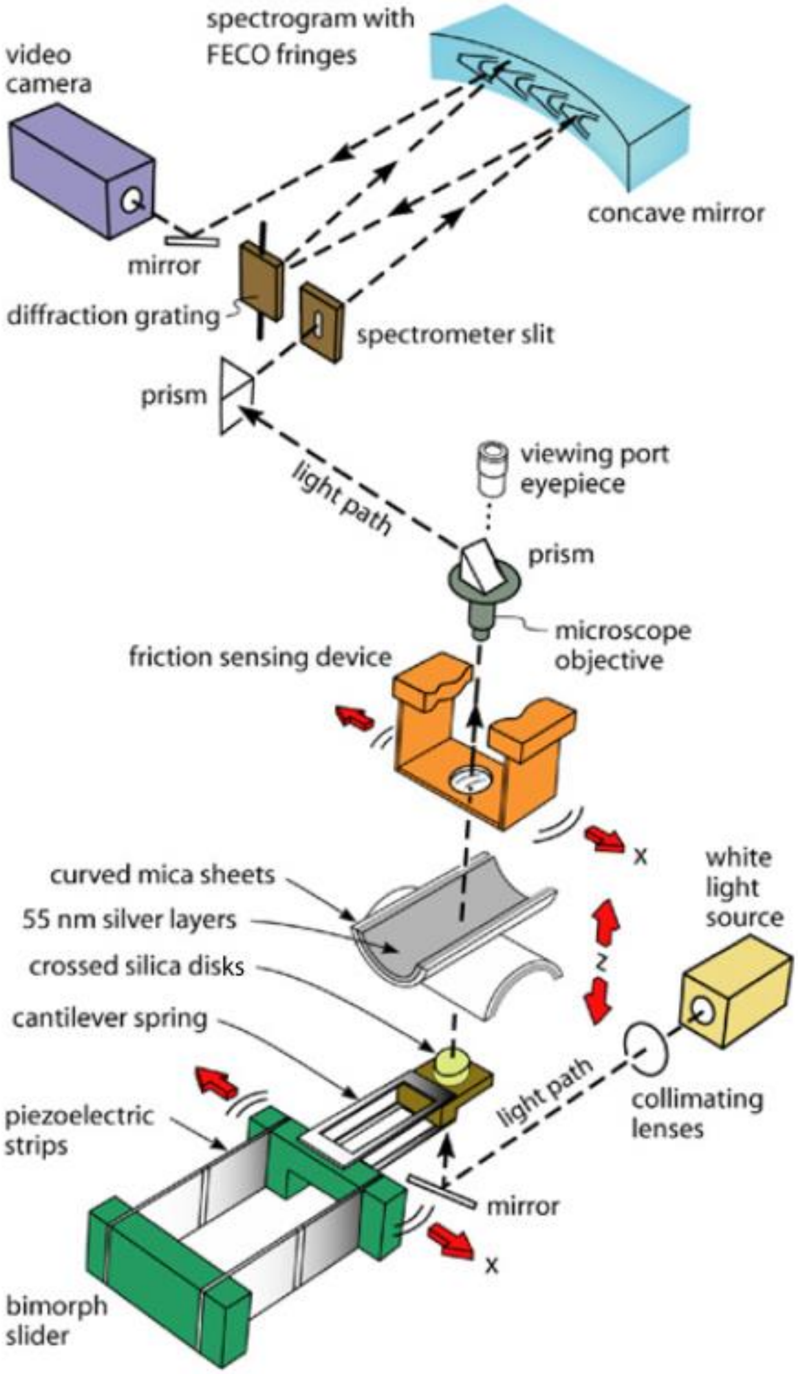

Figure 1.3 Full light path and schematic to show the creation and detection of FECO fringes (Adapted from reference 8). The bimorph slider and friction sensing device are also depicted to show how the surfaces can laterally shear and measure friction during an experiment.

The strain gauge setup and bimorph were used to perform adhesion and friction measurements on gecko mimetic adhesives in Chapter 2. A new rotating disk was also developed to use in high-speed, large distance, friction experiments, which were performed in Chapter 3 with skin creams. Finally, fluorescent imaging was simultaneously coupled with the SFA technique to visualize lateral spatial rearrangements of lipid domains upon membrane confinement in Chapter 4.

References

(1) Feynman, R. P. Forces in Molecules. *Phys. Rev.* **1939**, *56* (4), 340–343.

(2) Derjaguin, B. V.; Churaev, N. V.; Muller, V. M. The Derjaguin—Landau—Verwey—Overbeek (DLVO) Theory of Stability of Lyophobic Colloids. In *Surface Forces*; Springer US: Boston, MA, 1987; pp 293–310.

(3) Verwey, E. J. W. *Theory of the Stability of Lyophobic Colloids; the Interaction of Sol Particles Having an Electric Double Layer,*; Elsevier Pub. Co.,: New York, 1948.

(4) Donaldson, S. H.; Røyne, A.; Kristiansen, K.; Rapp, M. V.; Das, S.; Gebbie, M. A.; Lee, D. W.; Stock, P.; Valtiner, M.; Israelachvili, J. Developing a General Interaction Potential for Hydrophobic and Hydrophilic Interactions. *Langmuir* **2015**, *31* (7), 2051–2064.

(5) Dowson, D. *History of Tribology*; Professional Engineering Pub, 1998.

(6) Ruths, M.; Steinberg, S.; Israelachvili, J. Effects of Confinement and Shear on the Properties of Thin Films of Thermotropic Liquid Crystal. **1996**.

(7) Poole, R. The Deborah and Weissenberg Numbers. *Rheol. Bull.* **2012**, *53* (2), 32–39.

(8) Israelachvili, J. Recent Advances in the Surface Forces Apparatus (SFA) Technique. *Reports Prog. Phys.* **2010**, *73* (3).

(9) Tabor, D.; Winterton, R. H. S. The Direct Measurement of Normal and Retarded van Der Waals Forces. *Proc. R. Soc. A Math. Phys. Eng. Sci.* **1969**, *312* (1511), 435–450.

(10) Israelachvili, J. Thin Film Studies Using Multiple-Beam Interferometry. *J. Colloid Interface Sci.* **1973**, *44* (2), 259–272.

Chapter 2: Characterizing the Surface Interactions between Gecko-Inspired Structures and Diversified Substrates

2.1 Stick-Slip Friction of Gecko Mimetic Flaps on Smooth and Rough Surfaces

Reproduced with permission from Saurabh Das, Nicholas Cadirov, Sathya Chary, Yair Kaufman, Jack Hogan, Kimberly L. Turner, Jacob Israelachvili, *J. R. Soc. Interface* 2015, *12* (104), 20141346. Copyright©2015, The Royal Society

2.1.1 Abstract

The discovery and understanding of gecko's 'frictional-adhesion' adhering and climbing mechanism has allowed researchers to mimic and create gecko-inspired adhesives. A few experimental and theoretical approaches have been taken to understand the effect of surface roughness on synthetic adhesive performance, and the implications of stick-slip friction during shearing. This work extends previous studies by utilizing a modified Surface Forces Apparatus (SFA) to quantitatively measure and model frictional forces between arrays of polydimethylsiloxane (PDMS) gecko footpad-mimetic tilted micro-flaps against smooth and rough glass surfaces. Constant attachments and detachments occur between the surfaces during shearing, as described by an *Avalanche* model. These detachments ultimately result in failure of the adhesion interface and have been characterized in this study. Stick-slip friction disappears with increasing velocity when the flaps are sheared against a smooth silica surface; however, stick-slip was always present at all velocities and loads tested when shearing the flaps against rough glass surfaces. These results demonstrate the significance of preload,

shearing velocity, shearing distances, commensurability, and shearing direction of gecko-mimetic adhesives and provide a simple model for analyzing and/or designing such systems.

2.1.2 Introduction

Reversible adhesives, which exhibit high adhesion and minimal effort to detach, are vital to systems that need to stick and detach repeatedly with high speeds for fast movement. Smart and reversible adhesives are in growing demand for use in responsive robotics that can climb on walls and ceilings in precarious environments. The motivation for this specialized type of adhesive comes from the long-observed ability of geckos to effortlessly run and climb on trees, rocks, walls, and ceilings and maintain attachment while stationary and in motion. The gecko's ability to adhere and climb so flawlessly stems from the hierarchical structure of their toe pads and the mechanism they use to actuate and disengage this very high adhesion. The hierarchical system of the toe pads can form and adhere to micro- and nano- asperities on rough surfaces and create a clean contact, and the reliance of van der Waals forces can allow geckos to adhere to hydrophobic and hydrophilic surfaces as long as the polarizability of the surface is not low (e.g., Teflon)[1–3].

The mechanisms for attachment and high adhesive forces of gecko spatula and setae have been measured and modeled by Johnson-Kendall-Roberts (JKR)-type theories[4,5], while the ease of detachment from surfaces requires a peel-off theory[6–8]. The effect of end-shape and size of microfibers on adhesion has been investigated experimentally[9,10] and theoretically[11]. It has been found that the frictional forces (parallel to the surface) also contribute to the adhesive force (perpendicular to the surface), giving rise to the model of frictional adhesion. According to this model, the adhesion of a gecko foot-pad[12] or its mimic to a substrate depends on the applied shear force[4,6] and explains the very low detachment forces observed in climbing geckos. Anisotropic fibrillar synthetic adhesives mimicking the gecko footpad functionality have been previously fabricated[5,13–24] and were used to study adhesion and frictional properties on silica surfaces. The mechanism of operation of these structures involved application of a small preload (several milli-Newtons) followed by shearing the structures against the surface of interest for several microns to allow the real surface area of contact to be maximized and hence, attain a good grip. However, the stick-slip between the structured surface and the substrate was not taken into consideration during the shearing process in any of the previous work on gecko mimetic structures. Stick-slip sliding of surfaces is an undesirable property which can cause catastrophic failure if slip occurs while a robotic device is moving on an inclined surface or inverted ceiling. When a constant force (gravity) is acting on the surfaces, there is no restoring force to 'catch' and reattach the failed adhesion contact. Hence, determining the conditions (sliding velocities, preloads, sliding distance of the microstructures during movement of the robot, etc.) for avoiding stick-slip motion during the shearing of structured or patterned surfaces on a substrate are essential.

A common form of friction, stick-slip friction, occurs when the static friction force is higher than the kinetic friction force and is found in everyday phenomena such as squeaking doors or the sound produced from a bow sliding across a violin string. Stick-slip sliding occurs over a certain range of driving velocities when the friction force vs. velocity shows a negative slope which also depends on the compliance of the surfaces (Fig. 2.1). When the shearing drive moves towards the right by a distance Δx at a velocity v (Fig. 2.1A), the force in the spring connecting the drive to the PDMS base increases and this will pull the base by a distance ΔD at a velocity less than v because the friction force is increasing with displacement. The force that the spring experiences will be $f = k(\Delta x - \Delta D)$ and can be measured with the progress of time or displacement of the drive (point a to b in Fig. 2.1B). When the displacement increases beyond point b, the force required to cause sliding will be less than the force in the spring (slope, $k < k_0$) and this inbalance of the forces will accelerate the PDMS base and the slip will occur. Beyond point c, the friction force exceeds the spring force and the PDMS base will decelerate and come to a rest and stable sliding will reinitiate. For infinitely stiff spring (e.g., a stiff beam or an elastic string connecting the drive to the PDMS base), stick-slip cannot be measured since the slope of force-displacement curve for friction forces will never fall at a rate greater than what the loading system is capable of following. Hence, in Amonton's experiment, where a string was used to connect the rider to the drive, stick-slip phenomenon was never observed even though the static and kinetic coefficient of friction forces were different.

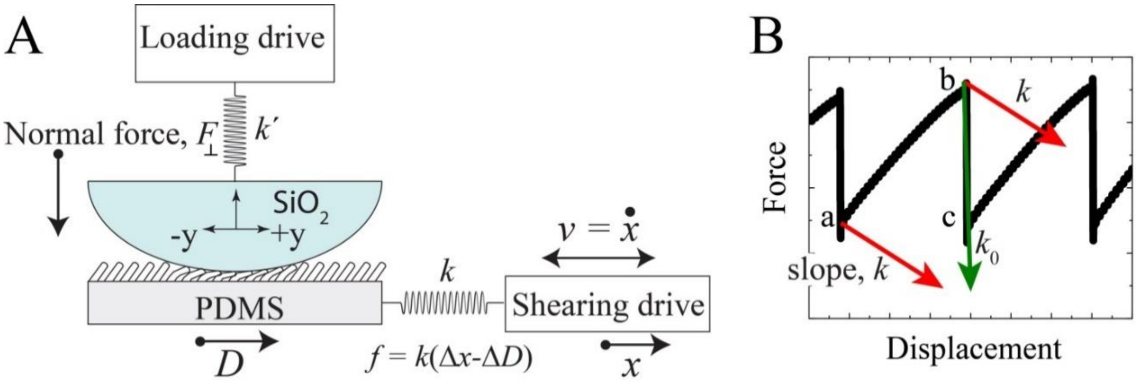

Figure 2.1 Schematics of the friction force measurement explaining the cause of stick-slip friction.

Stick-slip friction can arise by three different mechanisms during frictional sliding (1) a rough surface mechanism[25] (topography), (2) distance-dependent mechanism, and (3) a phase transition mechanism[26]. The first model describes when a rapid slip occurs as one surface goes over the top of an asperity on the opposing surface after "sticking" for the period due to interlocks prior to the slip. The distance-dependent model describes how a characteristic distance and time scale are observed as two surfaces increase adhesion strength after coming into contact, which may occur for smooth or rough surfaces. During shearing, the surfaces creep the characteristic distance before sliding occurs. These systems are related to the Deborah Number, De, which relates the intrinsic relaxation times of the materials to the time scales of movement and measurement in the system[27,28]. The time scales can easily be converted to a characteristic relaxation velocity and sliding velocity in the system. Lastly, the phase transition model is typically only present in lubricated systems or thin films confined between two surfaces which do not pertain to the presented system.

In this study, the friction properties of tilted biomimetic gecko flaps were investigated by measuring and characterizing the friction force as a function of the applied loads and shearing velocities using a Surface Forces Apparatus (SFA) in order to determine the optimum shearing conditions against smooth and rough surfaces. Here we also propose an *Avalanche mechanism* of stick-slip friction. We attribute the stick-slip behavior in our system to be a combination of surface topography effects as well as characteristic length and time scales related to the material properties of PDMS and intermolecular forces between PDMS and SiO_2.

2.1.3 Experimental

Large arrays of tilted PDMS micro flaps with an areal density of 6410 flaps/mm^2 mimicking the adhesive and frictional properties of a gecko foot pad were fabricated and have been described elsewhere[16,29]. A modified surface forces apparatus[16,30] (SFA, SurForce LLC) was used to measure the normal $F_\perp$ (adhesion and loads) and the lateral forces $F_\parallel$ between the arrays of the fabricated micro-flaps and a spherical silica disc of radius of curvature, $R = 2$ cm, and three different RMS roughnesses of 10 ± 8 nm (smooth), 133 ± 20 nm (rough) and

308 ± 56 nm (very rough). The detailed characterization of the roughnesses is given in Table 2.1. The asperities were identified as peaks from the AFM images. The reference is a peak to valley height measurement, not center line average. The mean distance is a center peak to center peak measurement averaged over 50 cross sections between two asperities of the AFM image (with no asperities in between the ones being considered). This type of description of surface roughness gives a more direct picture of the size and distribution of the asperities compared to RMS roughness. Calculations were made using AFM software (Gwyddion v.2.36).

Details of the force measurements have been described in previous work[16,29]. Briefly, the spherical glass disc was mounted to the top friction device that measures the lateral forces $F_{\parallel}$ on the fabricated flaps. The PDMS flaps were glued to a flat glass disc, which sits on a double cantilever spring with strain gauges that can measure the normal forces. The double cantilever spring was mounted on a bimorph device that can slide laterally over a distance of 1-700 µm at different sliding speeds (0.01-200 µm/s). A CCD camera was mounted on a microscope to visualize the contact area during loading, unloading and sliding of the spherical silica disc against the arrays of the fabricated PDMS micro-flaps.

In the SFA experiment, the PDMS micro-flaps were pressed against the top spherical silica disc at a constant speed of ~ 10 µm/s until the desired pre-load, L was reached. The flaps were then sheared against the smooth and the rough spherical glass disc at different velocities (0.08-200 µm/s). Stick-slip friction force and the instantaneous normal loads $F_{\perp}$ were measured simultaneously. The measured normal load $F_{\perp}$ was different from the applied pre-load L during sliding due to the deformation of the micro-flaps and adhesion/interlocking of the flaps to the glass surface. The flaps did not get damaged even after many sliding cycles

(100-1000) at a given contact point and the friction force was reproducible between different contact points on the flap surface. The surfaces were prepared in a clean dust free environment (under Laminar flow hood).

2.1.4 Results

The effect of normal loads ($F_{\perp}$) and driving velocities (v) on the stick-slip frictional properties of the synthetic tilted PDMS flaps against silica surfaces of different roughness (Table 2.1) were tested in a modified Surface Forces Apparatus (SurForce®, LLC) (Fig.2.2). Here, we characterize the surfaces with different roughness based on the height of the surface features (asperities), the spacing between them, the slope of the features, and RMS roughness as shown in Table 2.1.

Table 2.1 Comparison of roughness of borosilicate glass disks used to shear against the gecko-mimetic adhesive flaps. Roughness values were measured using an AFM.

Disk	**Avg. height of asperities (µm)**	**Avg. distance between asperities (µm)**	**Avg. slope of asperity edges**	**RMS Roughness (nm)**
Smooth	<0.01	N/A	N/A	11 ± 10
Rough	0.33 ± 0.06	6.7 ± 3.5	0.80 ± 0.45	133 ± 20
Very Rough	0.52 ± 0.09	1.5 ± 1.5	1.2 ± 0.9	308 ± 56

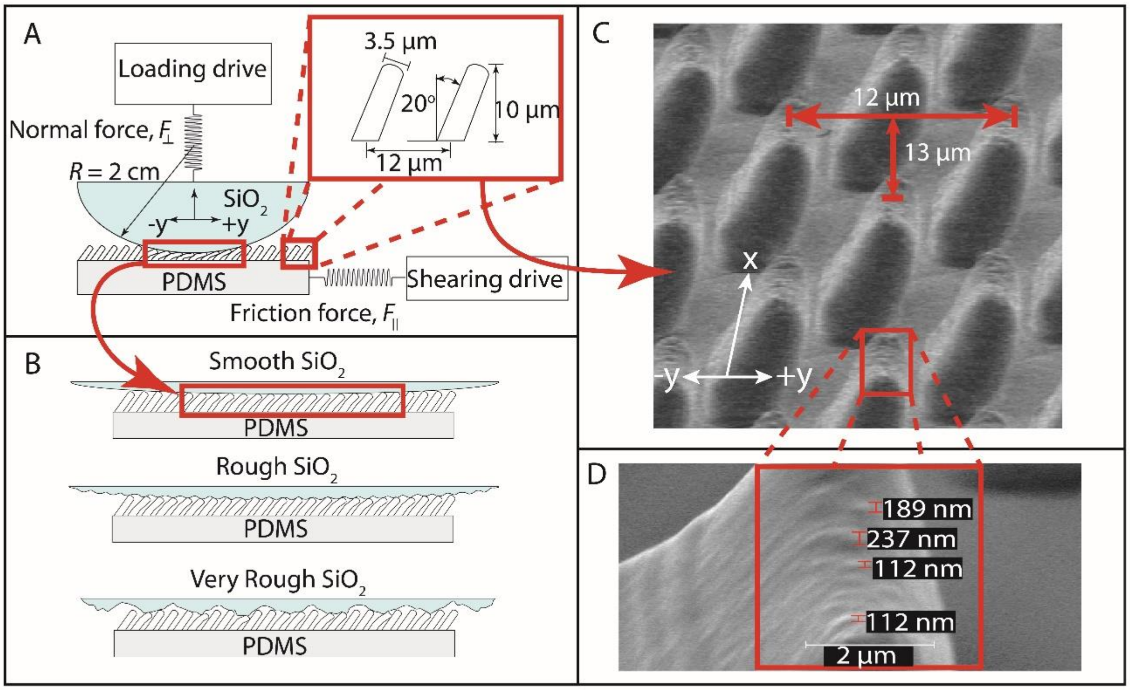

Figure 2.2 (A) Schematic representation of experimental setup in the SFA. Two opposing surfaces are sheared against each other: the bottom being the tilted PDMS gecko flaps and the top as the smooth or rough glass disk. (B) Schematic of the fitting of PDMS flaps into the different rough disk asperities. There is an interlocking mechanism due to spacing of the roughness on the glass disk that occurs with the rough (middle) disk. (C) SEM image of the biomimetic flaps depicting the in-plane distribution of the fibrillar structures showing the distance between the flaps along the x and y directions. (D) A zoom in on the tip of one pillar depicting submicron scale roughness (red bars) on its surface (scale bar in while, 2 µm).

The fluctuations in the lateral force (or friction force, $F_\parallel$) were measured in the SFA and the changes in the friction properties of the flaps shearing against the silica surface were monitored as v was increased at a given compressive force in the normal direction (pre-load, $F_\perp = L$). A close look at the measured friction forces as a function of time indicates that $F_\parallel$ can be resolved into three different components, (1) f_{st}, the stiction spike, (2) f_s, the static friction force, and (3) f_k, the kinetic friction force (Fig. 2.3).

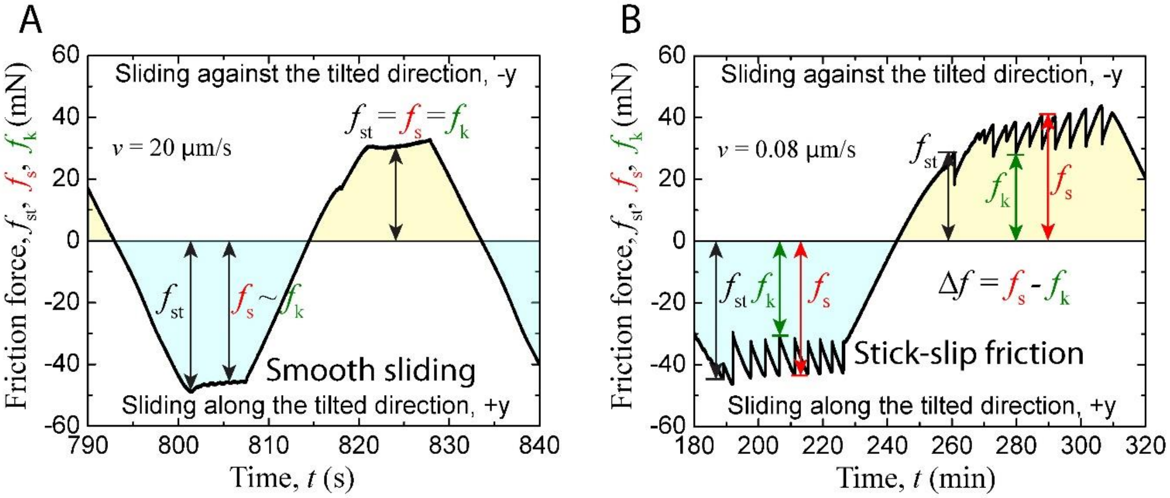

Figure 2.3 Friction traces of the smooth glass disks with a pre-load, L ~10 mN against gecko-mimetic tilted flaps, where friction forces, ($F_{\|} = f_{st}, f_s, f_k$) were measured as a function of time. Note that negative forces are not negative in magnitude, but result from the direction of shear during measurement. Smooth sliding (A) is observed at velocities greater than 20 μm/s compared to stick-slip friction which is present at lower drive velocities less than 20 μm/s (B) for the given pre-load.

The stiction spike (f_{st}) is the static friction force that must be overcome before any sliding begins between two stationary surfaces and could be higher or lower than the rest of the friction forces measured during shearing. The kinetic friction force (f_k) and the static friction force (f_s) are the minimal and the maximum magnitude of the measured lateral stresses respectively when the surfaces are in relative motion during shearing. The kinetic friction force and static friction force are equal during smooth sliding ($f_s = f_k$) [31]. When referring to stick-slip friction, the static force is the maxima of the friction trace (the "stick") and the kinetic friction force is the minima where interfacial sliding occurs (the "slip"). This distinction between kinetic friction in smooth and stick-slip sliding is important to note because the measured value of f_k in stick-slip is not necessarily the "true" value of f_k experienced between the surfaces[32]. It should be noted that the friction force (static and kinetic) increases in magnitude (up to 4 mN) while sliding against the direction of the tilt of the flaps (Fig. 2.3B). This is due to the small aberrations in the thickness of the PDMS base over which the flaps sit and is an artifact of the fabrication process. However, the friction forces do not change significantly (< 2 mN) while shearing along the tilt direction due to the strong adhesion of the flaps to the silica surface and hence the variation in the friction force due to minor misalignments is minimal.

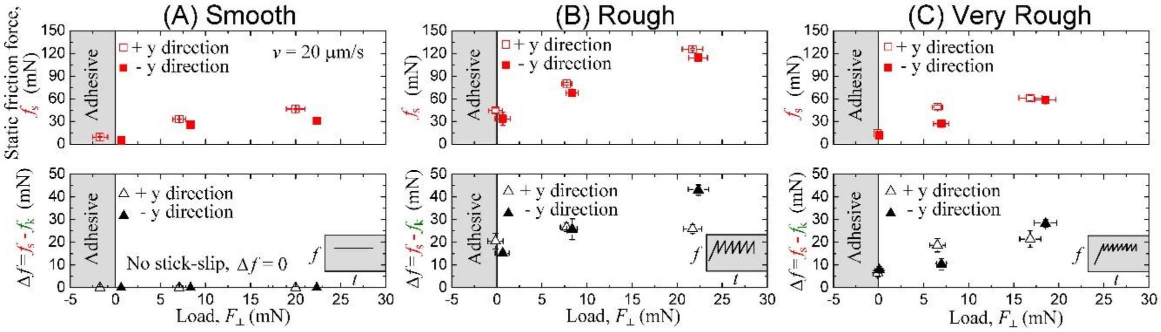

Figure 2.4 Plots of the static friction force (f_s "red") as a function of the load, $F_\perp$, for three varying levels of rough surfaces (A, B, C) sheared at a constant velocity, v = 20 μm/s, in the direction along the tilt of the gecko-mimetic flaps (+y) and against the direction of tilt (-y). The lower plots depict the magnitude of stick-slip friction by the relation $\Delta f = f_s - f_k$ where f_s is the static friction force and f_k is the kinetic friction force. The error bars indicate the standard deviation in the measurements from 3 different experiments including the variations in a given experiment (See Fig. 2.3B).

2.1.4.1 Effect of load on friction force at a constant driving velocity (v = 20 μm/s)

The tilted PDMS micro-flaps exhibited smooth sliding ($\Delta f = f_s - f_k = 0$) against a smooth silica disk for $F_\perp \leq 20$ mN and $v > 20$ μm/s (Fig. 2.4A). Stick-slip friction is always observed for the shearing of the flaps against the rough and the very rough silica surfaces for all loads (Fig. 2.4B and C). The friction forces ($F_\parallel$) are proportional to the normal loads ($F_\perp$) indicating that Amontons' law is followed [31] in the system under consideration (2.4A and C). The coefficient of friction, μ (slope of $F_\parallel$ vs. $F_\perp$), is higher for sliding of the flaps against the rough (static friction coefficient along +y direction, μ_{+y} = 3.4±0.2; static friction coefficient –y direction, μ_{-y} = 3.5±0.2) and the very rough (μ_{+y} = 3.1±0.9; μ_{-y} = 2.5±0.1) silica surfaces compared to the smooth surface (μ_{+y} = 1.7±0.7; μ_{-y} = 1.9±0.9). The magnitude of stick-slip friction increased as the load increased when shearing the flaps against the rough and the very rough surfaces. Interestingly, the flaps demonstrated similar (within 35% of the highest difference) magnitudes of $F_{\|}$ for a given $F_{\perp}$ on the smooth and the very rough silica surface which is significantly smaller than the $F_{\|}$ measured on the rough surface. However, when comparing the magnitude of stick-slip friction, Δf (triangle in lower plots in Fig. 2.4), the very rough surface exhibits high values of stick-slip compared to the smooth surface where no stick-slip is observed at any loads ($F_{\perp} \leq 20$ mN) at $v = 20$ μm/s. The flaps display maximum stick-slip during sliding on the rough silica surface, which is as high as double that of the very rough disk. At higher loads, the magnitude of stick-slip is greater for shearing along the –y direction (against the tilt of the flaps) compared to the +y direction (along the tilt of the flaps).

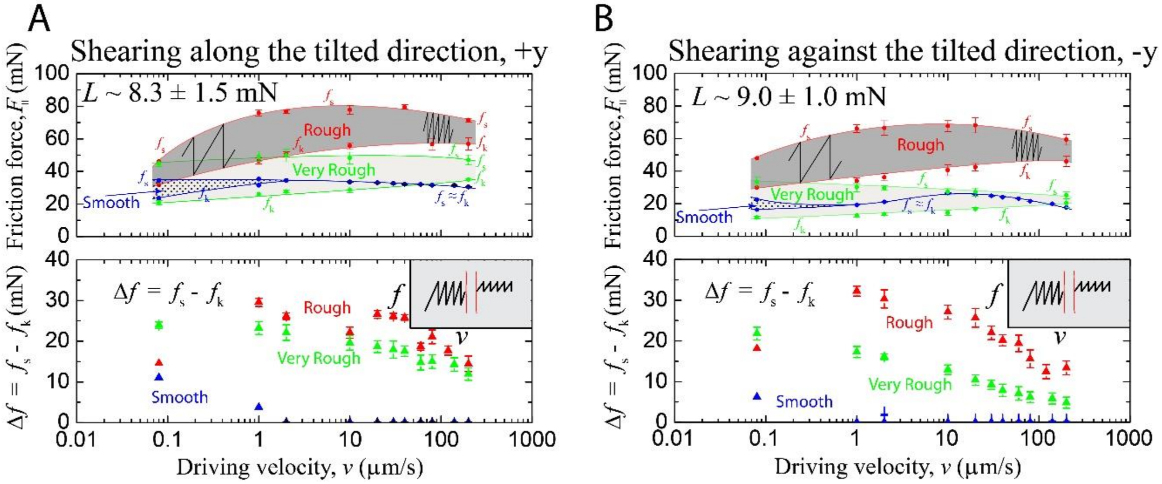

Figure 2.5 Plots of the static friction force (f_s) and kinetic friction force (f_k) from the friction traces as a function of the shear driving velocity, v, for three different rough surfaces of varying roughness (smooth (blue), rough (red), and very rough (green)) sheared at a constant load in the direction (A) along (+y direction) and (B) against (-y direction) the tilt of the tilted PDMS flaps. The lower plot depicts the magnitude of stick-slip friction by the relation $\Delta f = f_s - f_k$ where f_s is the static friction force and f_k is the kinetic friction force.

2.1.4.2 Effect of shear drive velocity on friction force

The tilted PDMS micro-flaps do not undergo stick-slip sliding ($\Delta f = f_s - f_k = 0$) against a smooth silica disk for $F_\perp \leq 20$ mN and $v \geq 20$ µm/s, however at lower driving velocities (v = 0.08-20 µm/s), the surfaces exhibit stick-slip motion ($\Delta f > 0$) (Fig. 2.5). Stick-slip is always present for shearing the micro-flaps against the rough and the very rough silica disks. The rough disk displays an increasing and then decreasing magnitude of stick-slip with increasing velocity (red triangles in Fig. 2.5). The magnitude of Δf is similar for shearing the flaps along the +y and –y direction on the rough disks. The very rough disk shows a higher magnitude of Δf along the +y direction relative to the –y direction of shear. Interestingly, even though the magnitude of stick-slip friction typically decreases with increasing velocities, the static friction force does not change significantly. This is contrary to a typical stick-slip phenomenon between sliding surfaces where the static force decreases to the magnitude of kinetic friction. In these experiments, the kinetic friction force is thus increasing to match the static friction force values.

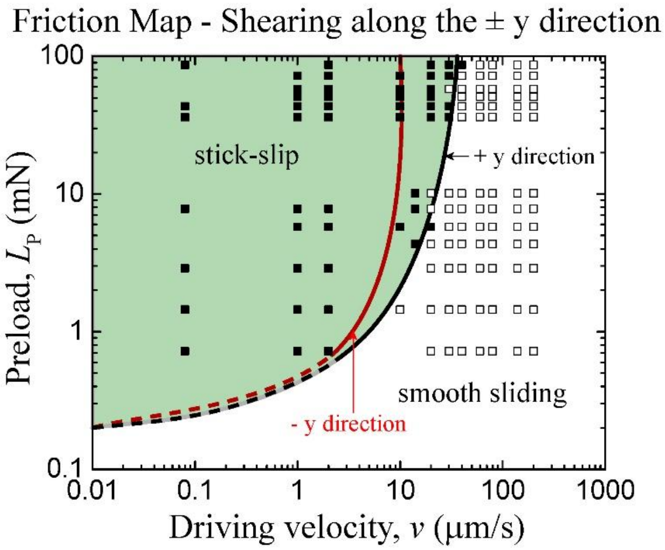

Figure 2.6 Friction map depicting stick-slip and smooth sliding regimes for the +y (along the tilt) and –y (against the tilt) shearing directions as a function of preload and driving velocity, *v*, for a smooth glass disk. Increasing driving velocity leads to smooth sliding. The dashed line is a continuation of the solid curve and extends in a regime where theoretically, for extremely low loads and low velocities, stick-slip during sliding should disappear; however, it cannot be measured due to experimental limitations.

2.1.4.3 Friction map

Depending on the nature of motion between the micro-flaps and the silica surface, a map can be constructed to indicate the regime of smooth sliding conditions and stick-slip friction (Fig. 2.6). The transition from stick-slip motion to smooth sliding is observed only when the micro-flaps are sheared against a smooth silica surface. The surfaces always show stick-slip friction between the flaps and the rough or the very rough surfaces in the velocity regime of the measurements. However, it should be noted that the magnitude of stick-slip decreases with increasing velocity during shearing, indicating that the sliding will eventually show a smooth motion for high shearing velocities. The 'smooth sliding' regions of the friction map may be interpreted as an indicator for the operating conditions of sliding velocities when actuating the foot of a robot with the gecko-mimetic pad attached to enable a secure stick to a surface and easy release. These results also stress the importance of the sliding distance during the operation of a gecko-mimetic footpad on robotic devices and are discussed later.

2.1.5 Discussion

Two very interesting phenomena are evident from the friction force measurements as a function of load. First, the rough surfaces exhibit the highest friction forces and stick-slip magnitude. This can be explained through an interlocking mechanism[29] (Fig. 2.7) where the roughness of the surface matches with the interspacing of the array of flaps. Based on the values in Table 1, the average distance between asperities on the rough surface (6.7 ± 3.5 μm) shows that it is possible to fit the flap dimensions (10 μm × 3.5 μm) in between some spots where the asperities are more spread out. The interlocking mechanism and fitting of flaps between surface asperities are compared in Fig. 2.7. The smooth disk does not have these asperities and the very rough disk has asperities too large and close together to allow for interlocking to occur. Another feature present in the data is that the friction values for the smooth and very rough surfaces are very comparable. It appears that the friction between the flaps and the pair of surfaces (smooth and very rough) follow Amontons' law, which states that friction forces are independent of the apparent area of contact. Molecular Dynamics (MD) simulations suggest that for non-adhering surfaces above a certain load, the coefficient of friction is independent of the detailed nature of the surface roughness[33]. These surfaces have previously been tested for adhesion and exhibit adhesion only once the surfaces have been sheared[4,16]. The very rough surfaces contain asperities that are too close together and too large for the full interlocking mechanism to take place, thus allowing Amontons' law to hold true.

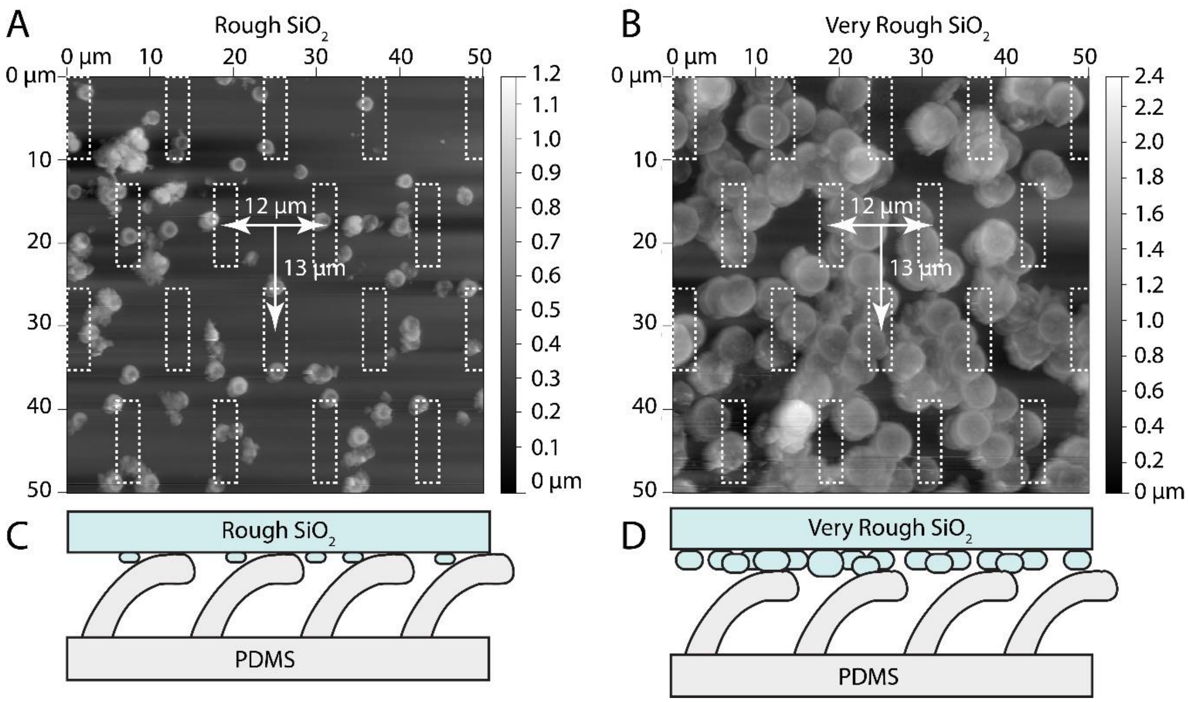

Figure 2.7 AFM images of the rough surfaces ((A) rough and (B) very rough) with an overlay of the gecko flap tip dimensions and spacing. The interlocking mechanism is displayed schematically where the rough disk (C) and PDMS flaps have commensurate spacing compared with the very rough disk (D), starting to approximate a "smooth" surface.

2.1.5.1 Stick-slip mechanism: The Avalanche Model

Here we present the *Avalanche Model* which explains that stick-slip instabilities at the macro level are initiated by the micro-instabilities at the contact junction between the individual micro-flaps and the silica surface (Fig. 2.8A and B). Stick-slip at individual micro contacts between two 'dry' surfaces in relative motion ensues due to creep instabilities[34], brittle fracture[35,36] or viscoelastic shear failure[37] of the interlocked asperities as they detach (Fig. 2.8A).

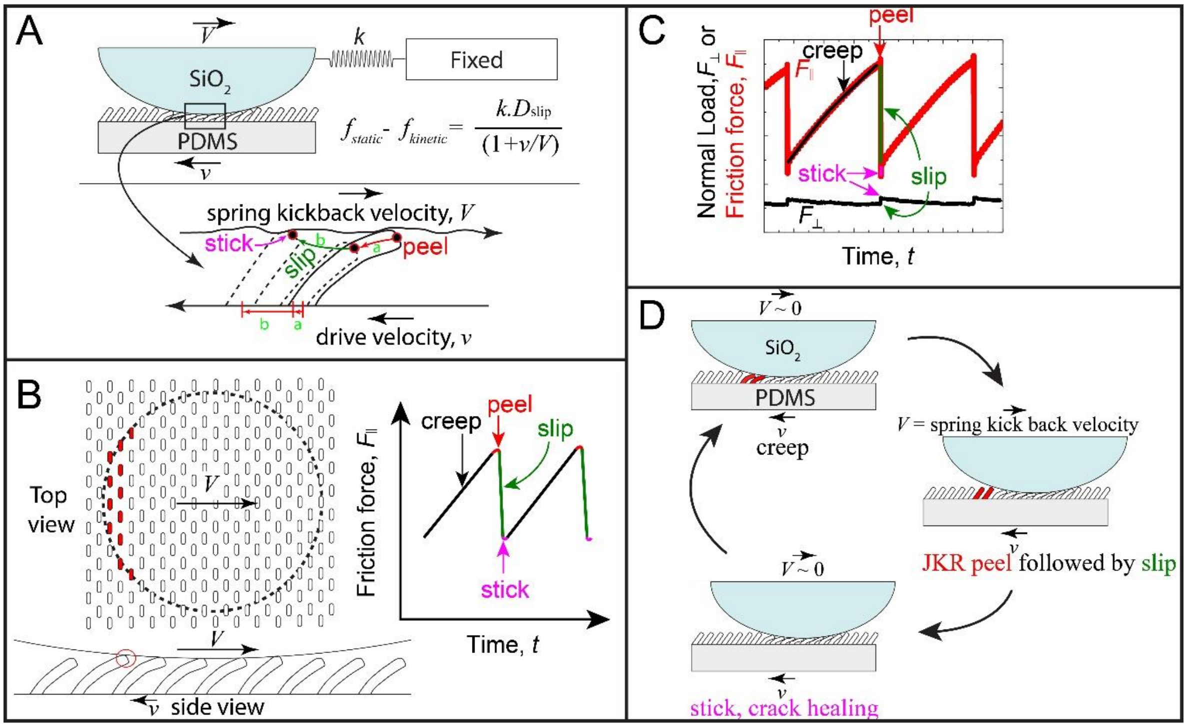

Figure 2.8 The *Avalanche* stick-slip of the arrays of PDMS flaps from the silica surface. (A) The PDMS micro-flaps peeling (JKR) from the silica surface during the *Avalanche* slip at the micro-scale that causes the force measuring spring to kick-back with a velocity *V*. (B) The flaps that are about to detach from the silica surface are shown in red along with a cartoon of the stick-slip friction trace showing the creep, JKR-peel, slip and stick regimes. (C) An illustration of the normal load ($F_{\perp}$) and friction force ($F_{\parallel}$) measured in the SFA during shearing of the micro-flaps against a silica surface showing the different regimes (creep, JKR-peel, slip and stick) during the *Avalanche* slip. It should be noted that the load fluctuates during sliding along the +y and –y directions similar to that observed for gecko setae[8]. (D) *Avalanche* slip as visualized at the macro-scale when the spherical silica surface is sheared against the PDMS micro-flaps.

The creep instability mechanism assumes that the stick-slip magnitude ($\Delta f = f_s - f_k$) is determined by the size of the contact area and not by f_s or the shear force required to break the adhesive interface. Even though the *apparent* area of the contact between the smooth silica surface and the PDMS flaps is larger than that between the rough/very rough disks for the same load, stick-slip sliding disappears when shearing the PDMS flaps against the smooth silica surface, unlike sliding on the rough/very rough surface. Hence, creep instability is not a plausible explanation for the stick-slip in our system. A brittle fracture mechanism can also be ruled out since the contact under consideration is soft and deformable. During sliding of the PDMS flaps on the silica surface, viscoelastic instability causes the contact junction to grow when the surfaces slide past each other and the friction force (or stress) increases during this stage from f_k to f_s. Depending on the relative displacement between the sliding surfaces, the contact junction dilates and breaks when a critical stress is reached, leading to a crack-like contact instability followed by the release of the elastic strain energy at the contact junction.

The trailing edge of a contact junction is associated with detachment of the individual flaps from the silica surface in a JKR peeling fashion[4,5]. The flaps that are about to detach from the silica surface are shown in red in Fig. 2.8B and D. When a critical stress is reached for a few micro-flaps at the contact boundary, they detach and trigger other near critical detachments, and the surfaces slip for a distance d or nd, where d = distance between the arrays of the flaps and n is an integer (See supporting Fig. 2.9). The slip is also associated with the propagation of Schallamach[38,39] waves from the front to the rear end of the contact. This propagation causes the viscoelastic PDMS flaps to release the shear stresses at the trailing edge of the contact junction and stick at the advancing edge of the contact to the silica surface. Hence, each slip is associated with a Schallamach wave and the frequency of stick-slip (φ) is equal to the rate of propagation of the waves. Each of these slips is associated with an increase and decrease in the apparent contact junction area and is evident from monitoring the top view.

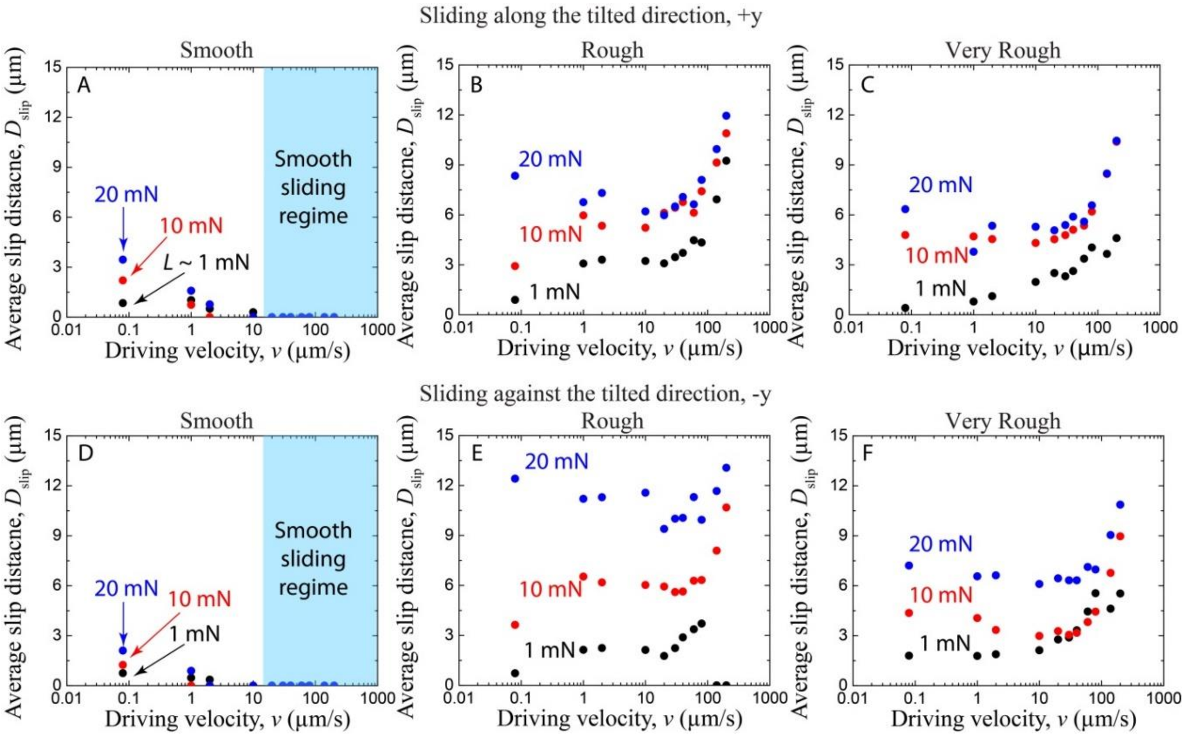

Figure 2.9 Average slip distances, D_{slip}, for three varying loads (1 (black), 10 (red), and 20 mN (blue)) as a function of shear driving velocity, *v*, for sliding of the smooth (A and D), rough (B and E), and very rough (C and F) glass disks along the direction of tilt (+y) and against the direction of tilt (-y) of the PDMS micro-flaps.

When Schallamach waves are responsible for the peeling (JKR mechanism) [4,5] and sticking of an adhesive interface, the work of adhesion can be estimated by[40],

$$F_{\square}v \sim \frac{f_s + f_k}{2} v = A_{\text{app}} \Delta W \varphi \qquad \text{(Eqn. 2.1)}$$

where φ = frequency of the Schallamach waves (s^{-1}), ΔW = Work of adhesion during *Avalanche stick-slip* (or energy dissipated during *Avalanche rupture* of the adhesive interface, not the thermodynamic work of adhesion) between the surfaces (J/m^2), v = velocity of the driving surface (m/s), and A_{app} is the apparent area of contact (m^2).

The work of adhesion for the shearing of the flaps against the silica surfaces was estimated using eq. (1). It should be noted that the rate of shearing affects the work of adhesion drastically over five orders of magnitude (See supporting Fig. 2.10). Energy dissipation (ΔW)

during sliding of the surfaces is maximal for the rough silica surface compared to the smooth and the very rough silica for similar loads and shearing velocities. The calculated ΔW for $v < 1$ µm/s is less than the thermodynamic work of adhesion between silica and PDMS since thermal energy provides a mechanism for the interfacial bonds between the surfaces to overcome a fixed energy barrier during the slow shearing process[28,41]. We also find that the energy dissipation shows a linear relationship with the sliding velocity (v) (Fig. 2.10).

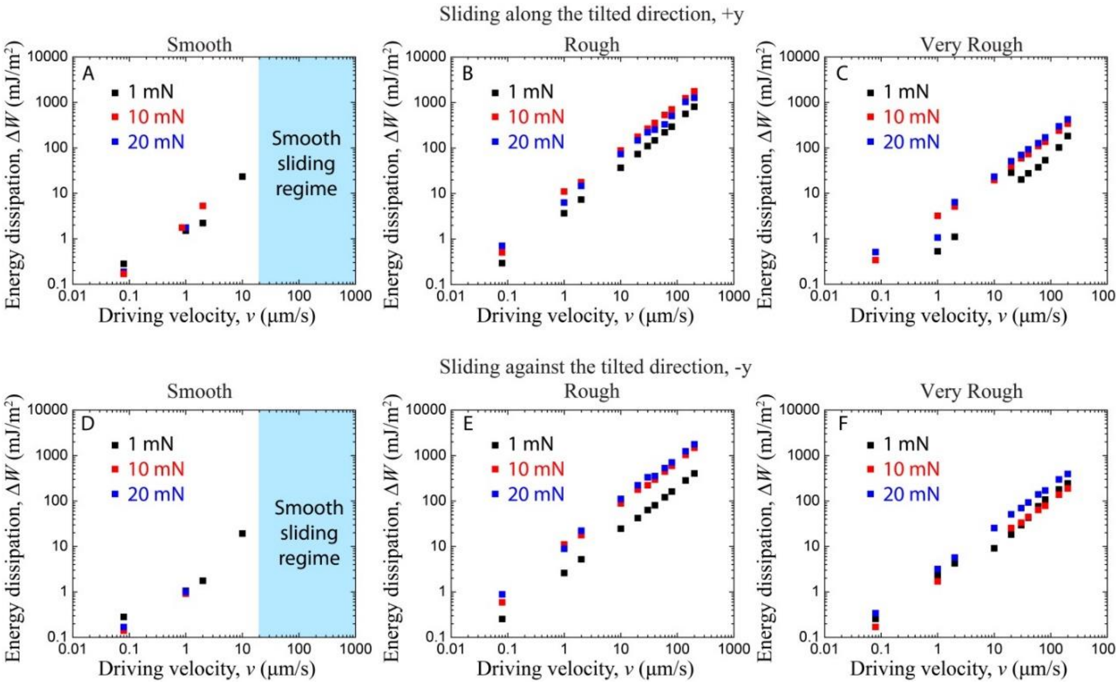

Figure 2.10 Work of adhesion, ΔW, during *Avalanche stick-slip* (or energy dissipation during *Avalanche rupture* of the adhesive interface, not the thermodynamic work of adhesion), for three varying loads (1 (black), 10 (red), and 20 mN (blue)) as a function of shear driving velocity, v, for the sliding of smooth (A and D), rough (B and E), and very rough (C and F) glass disks along the direction of tilt (+y) and against the direction of tilt (-y) of the PDMS micro-flaps.

The relative slip distance, D_{slip}, between the flaps and the silica surface can be used to characterize stick-slip friction. To calculate this value, the velocities of the two surfaces (v = drive velocity (m/s), V = spring kick-back velocity in the *opposite* direction of shear (m/s)) and time during the slip, t_{slip} (s), must be known, and can be related by

$$D_{\text{slip}} = t_{\text{slip}}\left(v+V\right) \qquad \text{(Eqn. 2.2)}$$

Here the only unknown value is the spring kick-back velocity, V, i.e., the average speed at which the lateral force measuring spring retracts back during the slip between the surfaces, which can be calculated from experimental data given by

$$V = \frac{f_{\text{s}} - f_k}{k t_{\text{slip}}} \qquad \text{(Eqn. 2.3)}$$

where t_{slip} = slip time (s), k = spring constant of the lateral force measuring spring (N/m), and f_{s} and f_{k} are the static and kinetic friction (N) as described previously. This is a complex relationship that also depends on surface roughness, load, and shearing velocity, which affects the values of f_{s} and f_{k} as seen from Figs. 2.4 and 2.5.

The slip time (t_{slip}) in our experiments was 60-80 µs for $v \leq 10$ µm/s and 40 µs for $v \geq 20$ µm/s when shearing against silica surfaces of different roughness. Thus, the *Avalanche* slip is characterized by a specific slip distance ($D_{\text{slip}} = nd$) and slip times (t_{slip}). The slip distance, D_{slip} is more dependent on the flap spacing compared to the distribution of silica surface asperities since D_{slip} shows similar length scales when sliding against both the rough and very rough surfaces (Fig. 2.9). The slip times are dependent on the elastic material properties of the flap's surface, where they are equivalent regardless of the surface roughness. These characteristic length and time scales give rise to a stick-slip sliding behavior that is less reliant on the commensurability between the shearing surfaces; however, the surface commensurability is a crucial property that determines the magnitude of friction (and adhesion) forces[29].

While shearing the PDMS micro-flaps against the silica surfaces (both smooth and rough), $f_{\text{s}} - f_{\text{k}}$ decreased and f_{k} increased as v was increased (Fig. 2.5). When sliding against the smooth surface, $f_{\text{s}} - f_{\text{k}} \rightarrow 0$ for $v > 20$ µm/s (Fig. 4 and 5). However, we did not observe smooth sliding for the rough and the very rough silica surfaces for v = 0.08-200 µm/s at all loads, L, tested. Theoretically, higher sliding velocities are required to reach the smooth sliding regime ($\Delta f = f_s - f_k = 0$), which were not attainable due to the limitations of the apparatus. A guaranteed approach to eliminate stick-slip in this system would be to only shear the surfaces for a specified distance, $D < D_c$, that never reaches the highest static friction value, f_s ($D = D_c$ at f_s), where stick-slip initiates. Clearly from the experiments performed, f_s varies as a function of load and velocity, which indicates that the critical distance, D_c, would also change based on the varying loads and velocities. Hence, an all-encompassing D_c should be the smallest sliding distance for any load and velocity combination tested prior to a stick-slip event. This will ensure that the surface does not shear past an f_s limit. The distance D_c can easily be calculated from the experiment as the average time it takes for f_k to transition to f_s multiplied by the shearing drive velocity, v. In our experiments, we calculate this critical sliding distance to be $D_c \leq 40$ µm for the rough surface and ≤ 15 µm for the very rough surface to encompass all v = 0.08-200 µm/s and L = 1-20 mN. Thus, to avoid *slip* failure on a rough surface, a robot with the reversible gecko-mimetic adhesive footpads should be sheared for a distance less than the critical sliding distance. To avoid slip failure on a smooth surface, it is simpler to increase the sliding velocity $v > 20$ µm/s for all loads examined in this study.

2.1.6 Conclusions

In this work, we demonstrate the effect of roughness and shearing velocities (v = 0.08-200 µm/s) on the stick-slip friction between tilted PDMS micro-flaps and silica surfaces. We show that Amontons' law is obeyed when the shearing between both smooth and very rough silica surfaces against the tilted micro-flaps. The flaps showed similar values for the static friction for shearing against the smooth and the very rough silica surfaces, and were characterized with an *Avalanche* stick-slip friction model with energy dissipation showing a linear relationship with the sliding velocity. Stick-slip sliding was always observed ($\Delta f = f_s - f_k > 0$) when shearing the flaps on the rough and very rough surfaces. Sliding the micro-flaps on the rough surface showed maximum Δf due to the interlocking-detachment cycles of the flaps with the surface asperities. The characteristic avalanche slip distances and times are determined by the topography and elastic properties respectively of the patterned flaps, and are independent of the commensurability between the surfaces. However, the commensurability determines the magnitude of friction.

Stick-slip friction is detrimental to the performance of the gecko-mimetic adhesives since slipping would result in the failure of the contact, and not allow the surfaces to grip again in the absence of a restoring force. Stick-slip friction of flaps on smooth surfaces can be eliminated by increasing the sliding velocity above a critical value (v_c = 20 μm/s in our experiments). The friction between the micro-flaps and the smooth silica surface was translated into a 'friction' map that may be interpreted as an indicator for the conditions of desirable sliding velocities when actuating the foot of a robot with the gecko-mimetic pad to enable both a secure stick to a surface and easy release. Stick-slip between the rough surfaces and the flaps can be eliminated by shearing the surfaces for a distance less than D_c, which is 40 μm and 15 μm for the rough and the very rough surfaces respectively. However, quantitative micromechanical mechanisms that can predict the critical distances (D_c) and sliding velocities (v_c) to circumvent stick-slip friction need further investigation and theoretical modeling based on the interface stiffness and topographical commensurability of the interacting surfaces. Our results stress the importance of the preloads, shearing distance, commensurability, sliding direction and velocities for the safe operation of gecko-mimetic footpads on robotic devices.

2.2 Influence of Humidity on Grip and Release Adhesion Mechanisms for Gecko Inspired Surfaces

Reprinted with permission from Nicholas Cadirov, Jamie A. Booth, Kimberly L. Turner, Jacob N. Israelachvili, *ACS Appl. Mater. Interfaces* 2017, 9 (16), 14497-14505.

2.2.1 Abstract

Geckos have developed foot pads that allow them to maintain their unique climbing ability despite vast differences of surfaces and environments, from dry desert to humid rainforest. Likewise, successful gecko-inspired mimics should exhibit adhesive and frictional performance across a similarly diverse range of climates. In this work we focus on the effect of relative humidity (RH) on the 'frictional-adhesion' behavior of gecko-inspired adhesive pads. A surface forces apparatus (SFA) was used to quantitatively measure adhesion and friction forces of a microfibrillar cross-linked polydimethylsiloxane (PDMS) surface against a smooth hemispherical glass disk at varying relative humidity, from 0 – 100 % (including fully submerged under water). Geometrically anisotropic tilted half-cylinder microfibers yield a 'grip state' (high adhesion and friction forces after shearing along the tilt of the fibers, F_{ad}^{+} and $F_{||}^{+}$) and a 'release state' (low adhesion and friction after shearing against the tilt of the fibers, F_{ad}^{-} and $F_{||}^{-}$). By appropriate control of the loading path, this allows for transition between strong attachment and easy detachment. Changing the preload and shear direction gives rise to differences in the effective contact area at each fiber and the microscale and nanoscale structure of the contact, while changing the relative humidity results in differences in the relative contributions of van der Waals and capillary forces. In combination, both effects lead to interesting trends in the adhesion and friction forces. Up to 75 % RH the grip state adhesion force remains constant and ratio of grip to release adhesion force does not drop below

4.0. Also, the friction forces, $F_{||}^{+}$ and $F_{||}^{-}$, and the release state adhesion force, F_{ad}^{-}, exhibit a maximum at intermediate relative humidity between 40 % and 75 %.

2.2.2 Introduction

Gecko-inspired adhesive technology has seen great progress in recent years. Since the discovery of the gecko's unique hierarchical foot pad structure[42], researchers have been able to understand the frictional adhesion mechanism[1,6,8,43] which facilitates climbing and thus develop their own gecko-inspired adhesive systems[44].

The current state of the art includes commercial adhesives such as Geckskin™,[45] and Gecomer®,[46]. These adhesive systems work quite well, scaling to support heavy loads in shear for attachment to walls in the case of Geckskin™, and supporting normal forces sufficient for application in pick and place manipulators in the case of Gecomer®. Similar adhesives have been integrated on climbing robots, more closely following the way in which the gecko exploits its adhesive system. A variety of climbing mechanisms have been employed, including roller tracks[47] (similar to tanks), and adhesive pads attached on the bottom of feet-like structures[48]. The main drawback in climbing systems has been the energy and force they require for detachment from a surface, thus hindering their speed. They do not completely take advantage of the gecko's ability to attach strongly, while also being able to detach swiftly and efficiently with low energy cost.

Common to these systems is an inability to maintain optimal function in non-ideal environments. The surfaces must be dry, clean, and smooth for best adhesive and frictional performance. There is broad intent to utilize gecko-inspired adhesives in changing environments - wet, dry, smooth, rough, and chemically varying surfaces – for which the gecko itself maintains climbing and perching ability.

In the adhesion community, much work has focused on general experimental and theoretical aspects of capillary effects and adhesion in humid environments[49–57]. In dry environments van der Waals forces typically dominate the adhesion force, compared to humid environments where capillary forces may be present and comparable in magnitude to van der Waals forces, with the latter being modified by the presence of intermediate water layers. Some work has also focused on the impact rough/microstructured surfaces and contact geometry have on the formation of capillary bridges and the resulting magnitude of adhesion forces[58–69]. These studies have shown that multi-asperity contacts induce humidity-dependent adhesion forces, especially with the presence of surface features on the nanometer- to micron-scale.

Examination of the influence of relative humidity on adhesion and friction in natural fibrillar systems has led to conflicting results. In the gecko, for example, it was proposed that the role of capillary forces was minor as a result of consistency in friction and adhesion measurements for single setae on hydrophobic and hydrophilic substrates, yet measurements were only performed at a single relative humidity[3] . It was later shown that single spatulae in load-shear-unload experiments exhibited a monotonic increase in the adhesion force over the range 0 – 60 % relative humidity[70]. Results for the friction force at the whole animal level[71] are consistent with this increase at intermediate humidity, but reveal a reduction at higher humidity (RH 85 %) in certain species. A similar non-monotonic trend has been revealed for some species of spider[72] and beetle[73]. However, whole gecko friction measurements by Niewiarowski *et al.*[71] are not consistent with the examination of isolated setal arrays[74]. The friction force is approximately consistent between 0 % and 100 % relative humidity, with the discrepancy likely being the result of differences in loading conditions[71]. Hypotheses on the underlying mechanisms are varied, and include changes in short range interactions in the presence of adsorbed water[70], alteration of capillary contributions[69], water-induced surface chemistry changes[74], and humidity-induced softening[75].

What *is* clear from this body of work is the complexity of fibrillar systems in humid environments, and the difficulty in making comparisons across systems where there exist differences in surface chemistry, geometry, and loading conditions. In the context of synthetic systems, the majority of studies have focused on adhesion forces on geometrically isotropic fibers (hemisphere-, flat- and mushroom-tipped cylinders) designed to generate high forces during normal approach and retraction[76,77]. The adhesion force tends to decay slightly with increasing relative humidity, with the reduction being sensitive to the tip geometry. Similar adhesives have recently been tested in shear[78], and display a non-monotonic behavior similar to that observed in natural systems[71]. There have also been some studies on insect-inspired switchable adhesives that use porous fibrillar adhesive pads[79,80]. These adhesives demonstrate high adhesion in humid environments and low adhesion in dry environments due to a combination of capillary formation and humidity-induced pad softening. Yet to receive significant attention is the use of geometrically anisotropic fibers in humid environments, and the ability to maintain grip and release capability through load path dependent adhesion and friction. In addition, some of the prior investigations of synthetic systems do not capture the full picture - looking at a small range of humidity[58,68], using single contact points with AFM to try to explain macroscopic effects[58], or using short humidity equilibration times[76].

Our work aims to address these topics while also exploring the grip-release mechanisms of our gecko-inspired adhesives in humid and wet environments. Geometrically anisotropic half-cylinder microfibers[81,82], as well as tilted half-cylinder microfibers[83], yield high adhesion and low adhesion states by controlling the loading path (approach-shear-retraction). Shear in one direction results in a large contact area and high friction and adhesion, referred to as the ‘grip state’. Shear in the opposite direction yields a small contact area and low friction and adhesion, referred to as the ‘release state’. This adhesive system aims to uniquely mimic the gecko’s ability to detach with little effort during climbing, and has previously demonstrated high durability over thousands of continuous loading and unloading cycles with high anisotropic friction and adhesion forces[83]. The goal of this study is to facilitate more extensive use of these adhesives by developing a greater understanding of how microstructured surfaces perform in humid and wet conditions and to verify if anisotropy in the grip and release state is maintained.

2.2.3 Methods

2.2.3.1 Fabrication of microfiber arrays

Arrays of angled half-cylinder microfibers (pictured in Figure 2.11) were fabricated from polydimethylsiloxane (PDMS) using a technique previously reported[83]. A negative mold was first prepared by patterning a glass substrate with a photoresist bilayer. A layer of PMGI SF-15 photoresist (MicroChem Corp., Newton, MA), approximately 12 µm in thickness, serves as the structural material for the mold. A top layer of AZ 5214 image reversal photoresist (AZ Electronic Materials, Branchburg, NJ), approximately 1.4 µm in thickness, was used to pattern the fiber cross-section. Taking advantage of the differing sensitivity of each layer to UV light, the AZ 5214 was patterned by photomask in an i-line stepper with a regular hexagonal array of semicircles. The desired fiber spacing, a, and radii, r, are 15 µm and 5 µm respectively, as shown in the schematic of Figure 2.11A. Upon development, this layer served as a mask for subsequent deep UV exposure of the PMGI resist. During this exposure, the wafer was mounted at an angle such that, upon molding, the flat side of the fiber faces toward the surface with which it will contact.

The mold was prepared for casting of the curable elastomer by baking to improve durability, and by deposition of a layer of 1H, 1H, 2H, 2H-perfluorodecyltrichlorosilane (FDTS) to promote easy separation of the mold and sample. PDMS (Sylgard 184, Dow Corning, Midland, MI) was prepared at a 10:1 ratio by weight of pre-polymer and cross-linking agent and was poured over the negative mold. The PDMS was cured at 100°C for 15 minutes, before the mold and sample are separated by hand.

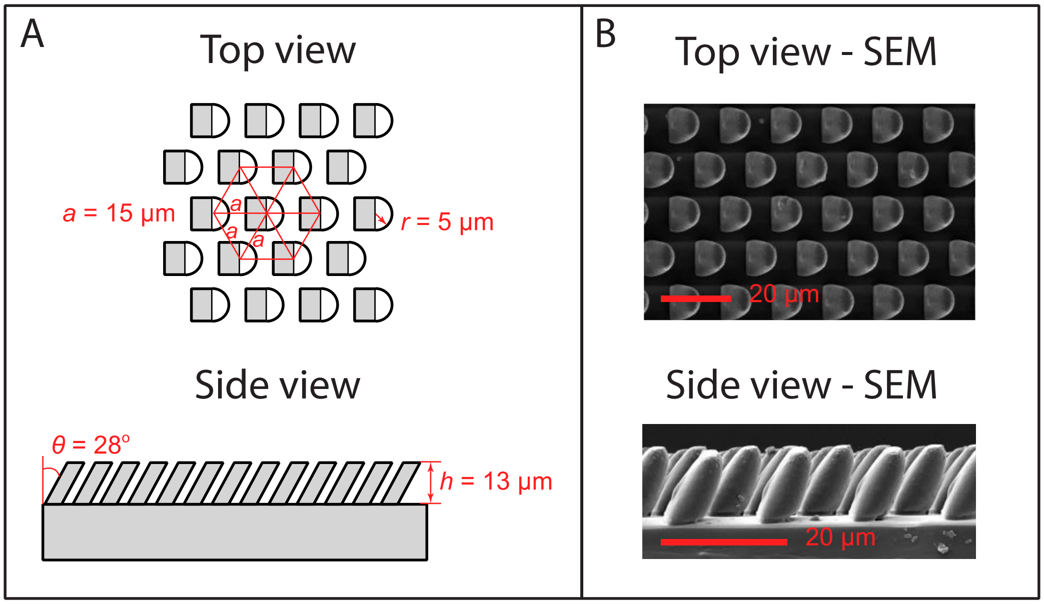

Figure 2.11 Microfiber surface schematic with dimensions (A) and corresponding SEM images (B). The PDMS microfibers are arranged in a regular hexagonal lattice with a spacing of 15 µm. The fibers are angled with respect to the surface normal and have a semicircular section (yielding tilted half-cylinder geometry). The angle from the surface normal is ~28° for the flat face, and ~15° for the curved face. The height from base to tip is ~13 µm.

The resulting microfibers are shown in Figure 2.11. The height from base to tip is ~13 µm. The fiber is tapered because of greater exposure of the top surface of the mold to deep UV. This leads to greater development of the PMGI resist in the region which forms the fiber base. The radius at the fiber base is ~5 µm, and at the fiber tip is ~3 µm. The fiber spacing is 15 µm, as expected. The angle from the surface normal is ~28° for the flat face, and ~15° for the curved face.

2.2.3.2 Adhesion and friction force measurements

Adhesion and friction measurements were simultaneously obtained using a surface forces apparatus (SFA2000, Surforce©)[30] utilizing a friction top mount and strain gauge attachments, shown schematically in Figure 2.12. The lower surface consists of either a flat (non-structured) or microstructured (microfiber array) PDMS glued to a flat glass disk. The non-structured PDMS serves as a control to isolate the effects due to the microfiber array. The upper surface is a half sphere of borosilicate glass with radius of curvature of $R = 1$ cm, which gives rise to a projected contact diameter of approximately 500 µm at the loads tested. Articulation of the upper surface is controlled by motorized micrometers. Two separate experiments were performed. The first involves normal approach and normal retraction of the surfaces (load-unload test). The second involves normal approach, lateral displacement, and normal retraction (load-shear-unload test). Shear was performed both with the fiber tilt, x^+, and against the fiber tilt, x^-. The bottom surface is supported by a double cantilever spring to which strain gauges are attached, permitting measurement of the normal force. On approach we control the preload, L, and during retraction the adhesion force, F_{ad}, is recorded. Separate strain gauges are attached to the top mount friction springs to measure the force in the lateral direction, with the static friction force being $F_{||}$. Experiments were performed with preloads of 2, 8, 16, and 32 mN. The number of fibers and size of the contact will increase with preload, as will the degree to which the fibers are compressed and ultimately buckled. Surfaces approach and retract at a rate of 100 nm/s. In loading-shear-unloading experiments a lateral displacement of 150 µm was applied at a rate of 10 µm/s during the shear phase.

2.2.3.3 Relative humidity measurement and control

All experiments were performed at relative humidity levels of 0 %, 40 %, 60 %, 75 %, > 95 %, as well with the contact fully submerged in water. Humidity measurements were conducted and monitored *in situ* with an HC2-S humidity probe (Rotronic©) attached and inserted into the SFA. Each humidity set point was equilibrated for 48 hours before adhesion and friction measurements were performed. A relative humidity of 0 % was obtained by purging the SFA chamber with N_2 gas. Intermediate humidity levels were controlled by inserting a small vial of saturated salt solution into the sealed SFA chamber (Sodium Iodide 40 %, Sodium Bromide 60 %, Sodium Chloride 75 %)[84]. The > 95 % RH condition was controlled by placing a small vial of Milli-Q® purified water in the SFA chamber. This is referred to as > 95 % because the humidity probe is only accurate up to 95 % RH, and because it is unlikely that the RH at the point of contact between the surfaces is exactly 100 % RH. The slightest temperature difference between the surfaces and humidified air will prevent the contact from fully reaching 100 % RH. The contact is submerged using a cup attachment housing the lower surface filled with Milli-Q® purified water. Given the thermodynamic equivalence of 100 % RH and fully submerged underwater, this set of experiments is subsequently referred to as 100 % RH.

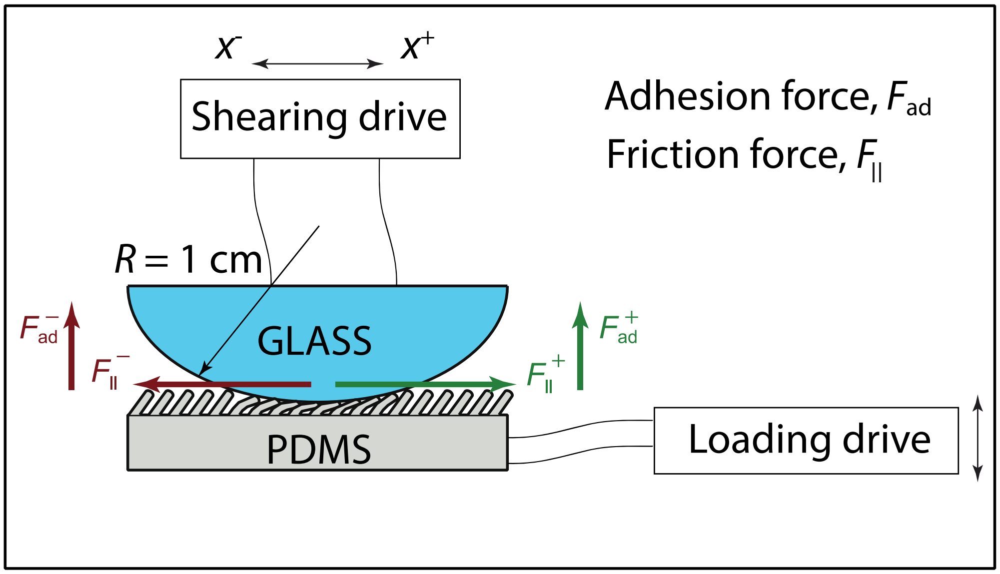

Figure 2.12 Schematic of the Surface Forces Apparatus (SFA) The lower surface consists of either a flat PDMS or microstructured PDMS (shown) glued to a flat glass disk. The upper surface is a half sphere of borosilicate glass with radius of curvature R = 1 cm. The bottom surface is supported by a double cantilever spring to which strain gauges are attached, permitting measurement of the normal force (preload, L, and adhesion force, F_{ad}). Separate strain gauges are attached to the top mount friction springs to measure the force in the lateral direction (friction force, $F_{||}$). Both load-unload and loading-shear-unload experiments were performed. Shear was performed both with the fiber tilt, x^+, and against the fiber tilt, x^-.

2.2.4 Results

2.2.4.1 Load-unload test

Loading-unloading experiments were performed for both the microfiber PDMS surface, and a flat PDMS control. The adhesion force in the absence of shear, F_{ad}, was measured and compared for each. The roughness of the glass disk (10 nm RMS) was such that interpenetration of asperities and microfibers, known to enhance the adhesion force[29,85,86], was not expected. As such, the flat PDMS served as an upper bound on the adhesion force for this system. The adhesion force for the microstructured sample was compared to that obtained with shear, both with and against the fiber tilt, to examine the robustness of the grip-release mechanism in humid environments (Section 2.2.4.2).

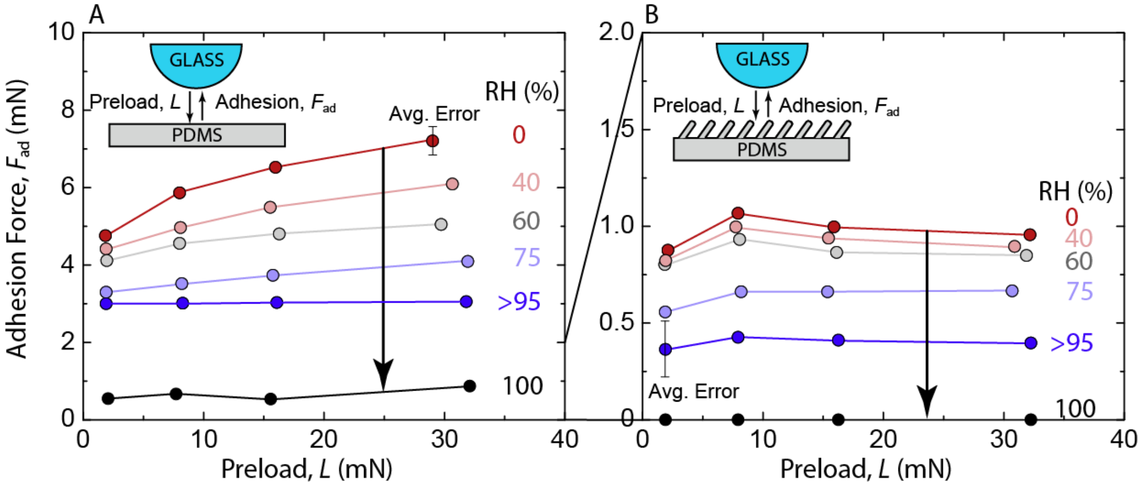

Figure 2.13 Load-unload adhesion force, F_{ad}, as a function of preload, L. Results are presented for both flat PDMS (A) and microstructured PDMS (B). For flat PDMS Adhesion forces at low humidity (red) have a greater dependence on preload than at high humidity. Adhesion forces decrease monotonically with increasing relative humidity, from 0 % (red), 40 % (pink), 60 % (gray), 75 % (lavender), > 95 % (blue), and 100% underwater (black). For microstructured PDMS the adhesion forces at low humidity exhibit an intermediate maximum, in contrast to flat PDMS (A). A similar monotonic reduction in the adhesion force with increasing humidity is observed on microstructured PDMS, with the magnitude of these forces being considerably lower than flat PDMS.

Adhesion force on flat substrate

There are two noticeable trends in the preload dependence of the adhesion force between the flat PDMS sample and glass disk, shown in Figure 2.13A. First, under 0 % RH the adhesion force increases as the preload increases from 2 to 32 mN. This trend is consistent with other investigations of flat PDMS with spherical glass probes[87]. A preload dependent adhesion force is not anticipated for the elastic contact of spherical unpatterned/smooth bodies[88]. To the authors knowledge, no systematic investigation of this preload dependence in unpatterned elastomer samples has been performed. This preload dependence diminishes with increasing humidity, and is no longer discernable at > 95 % and 100 % RH (underwater).

The second trend observed is a reduction in the adhesion force with increasing relative humidity, shown in Figure 2.14. Anticipating that the relative contributions of van der Waals and capillary effects to the total adhesion force will change as the relative humidity is increased, it is useful to examine theoretical predictions for these contributions in several limits to better understand this behavior. The simple geometry of the control experiment is conducive to such an approach.

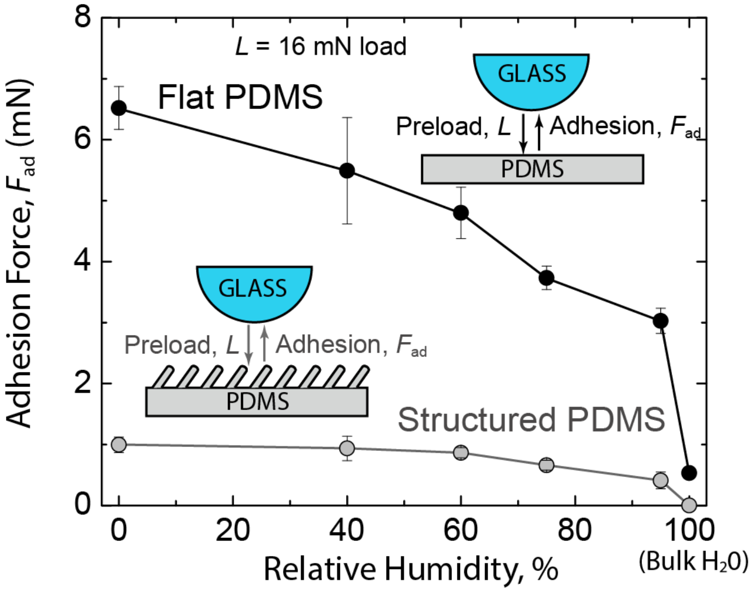

Figure 2.14 Load-unload adhesion force, F_{ad}, as a function of relative humidity for a preload L = 16 mN. Results are presented for both the flat PDMS surface (black) and the angled microstructured PDMS surface (gray). In both cases the adhesion force decreases monotonically with increasing relative humidity.

Theoretical Prediction

Work of adhesion – van der Waals contribution

The van der Waals work of adhesion can be stated in terms of the Hamaker constant, A, as

$$W_{\mathrm{vdW}} = \frac{A}{12\pi {D_0}^2} \qquad \text{(Eqn. 2.4)}$$

where the cutoff separation is typically assumed to be D_0 = 0.165 nm[28].

For two bodies (subscripts 1 and 2) interacting across a third medium (subscript 3) the Hamaker constant, based upon the Lifshitz theory and assuming an identical absorption frequency in all media, is[28]

$$A = \frac{3}{4}kT\left(\frac{\varepsilon_1-\varepsilon_3}{\varepsilon_1+\varepsilon_3}\right)\left(\frac{\varepsilon_2-\varepsilon_3}{\varepsilon_2+\varepsilon_3}\right) + \frac{3h\nu_{\mathrm{e}}}{8\sqrt{2}}\frac{(n_1^2-n_3^2)(n_2^2-n_3^2)}{(n_1^2+n_3^2)^{\frac{1}{2}}(n_2^2+n_3^2)^{\frac{1}{2}}\{(n_1^2+n_3^2)^{\frac{1}{2}}+(n_2^2+n_3^2)^{\frac{1}{2}}\}} \qquad \text{(Eqn. 2.5)}$$

where ε is the dielectric constant, n the refractive index, k the Boltzmann constant, T the temperature in Kelvin, h is Planck's constant, and v_e is the main absorption frequency in the UV (typically around $3\text{x}10^{15}$ s^{-1})

In the situation of 0 % RH, the separating media is dry air. Using properties for borosilicate glass and PDMS across air (Table 2.2), Equation 2.5 yields A_{air} = $7.62\text{x}10^{-20}$ J. This can be contrasted with the case of > 95 % and 100 % RH where the interaction occurs across water, for which we obtain A_{water} = $6.44\text{x}10^{-21}$ J. In combination with Equation 1, these yield van der Waals contributions to the work of adhesion of $W_{\text{vdW}}^{\text{air}} = 74\ \text{mJ/m}^2$ and $W_{\text{vdW}}^{\text{water}} = 6\ \text{mJ/m}^2$.

Table 2.2 Dielectric constant and refractive index used in Equation 2.5 to calculate Hamaker constants.

Material	Dielectric constant, ε	Refractive index, n
Glass	4.6	1.474
Air	1	1.000
Water	80	1.333
PDMS	2.5	1.41

For intermediate relative humidity, from 10-90 %, it is much more difficult to calculate an accurate Hamaker constant. In the central portion of the contact, glass and PDMS interact across a liquid water capillary bridge (Figure 2.15). Outside of this the interaction occurs across a vapor phase, the dielectric properties of which will depend on the relative humidity.

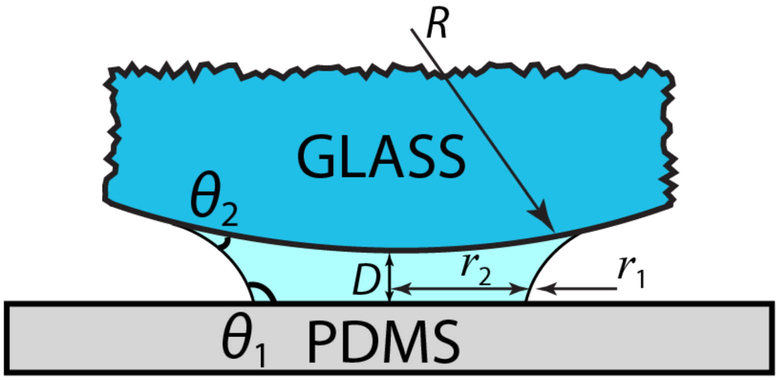

Figure 2.15 Schematic of a capillary bridge between flat PDMS and a glass sphere of radius R. The water contact angles are θ_1 and θ_2 on the PDMS and glass, respectively. The minimum separation of the surfaces is D, and the water capillary bridge has meridional principal radius r_1, and azimuthal principal radius r_2.

Work of adhesion – Capillary contribution

Capillary forces are the result of both the Laplace pressure inside the liquid bridge and normal surface tension around the circumference on the solid-liquid-vapor interface. We consider the case of a capillary formed between a sphere and flat surface, shown schematically in Figure 2.15. If the radius of the spherical body, R, is much greater than the distance between the two surfaces, D, and the azimuthal principal radius, r_2, is much greater than the meridional principal radius, r_1, then the capillary adhesion force can be simplified as[28]

$$F_{\mathrm{cap}} = 2\pi R\gamma_{\mathrm{L}}(\cos\theta_1 + \cos\theta_2) \qquad \text{(Eqn. 2.6)}$$

where γ_{L} is the surface energy of water and θ_1 and θ_2 refer to the water contact angle on glass and on PDMS.

The capillary force between rigid spheres given in Equation 2.6 can be utilized to obtain an effective contribution to the work of adhesion using the Derjaguin approximation[28]

$$\frac{F_{\mathrm{cap}}}{2\pi R} = W_{\mathrm{cap}} \qquad \text{(Eqn. 2.7)}$$

which results in

$$W_{\mathrm{cap}} = \gamma_{\mathrm{L}}(\cos\theta_1 + \cos\theta_2)\,. \qquad \text{(Eqn. 2.8)}$$

Capillary formation is expected for 40 % to > 95 % RH (not including submerged under water, 100 % RH). With water contact angles $\theta_1 = 5° - 10°$ and $\theta_2 = 110° - 115°$ on glass and PDMS respectively and surface energy $\gamma_{\mathrm{L}} = 72$ mJ/m^2, Equation 2.8 yields $W_{\mathrm{cap}} = 40 - 47$ mJ/m^2.

Adhesion Force

Given the low modulus of the PDMS and the relatively high work of adhesion contributions given in the preceding section, the system considered is within the range of validity of the Johnson-Kendall-Roberts (JKR) theory as dictated by the Tabor parameter[89]. The adhesion force between the elastic bodies is therefore

$$F_{\mathrm{JKR}} = \frac{3}{2}\pi R W_{\mathrm{total}} \qquad \text{(Eqn. 2.9)}$$

where W_{total} is the work of adhesion and, in the case of a sphere-on-flat geometry, R is the radius of the spherical body.

Theoretical values for the adhesion force can be calculated in the limits of 0% RH, > 95% RH and fully submerged using the work of adhesion contributions derived above. The van der Waals and capillary work of adhesion can be combined as

$$W_{\text{total}} = W_{\text{vdW}} + W_{\text{cap}}\,. \qquad \text{(Eqn. 2.10)}$$

At 0 % RH we expect only a van der Waals interaction occurring across dry air. The resulting the work of adhesion, $W_{\text{total}} = W_{\text{vdW}}^{\text{air}} = 74\ \text{mJ/m}^2$. For a sphere of radius R = 1 cm, Equation 2.9 yields an adhesion force, $F_{\text{JKR}}^{0\%\text{RH}} = 3.5\ \text{mN}$. When fully submerged underwater (100% RH), capillary forces are no longer present and the van der Waals interaction occurs across water. In this case, we obtain the work of adhesion, $W_{\text{total}} = W_{\text{vdW}}^{\text{water}} = 6\ \text{mJ/m}^2$, and the adhesion force $F_{\text{JKR}}^{100\%\text{RH}} = 0.3\ \text{mN}$. Lastly, in the case of 95% RH both van der Waals and capillary forces contributions are expected. The latter occurs across water and the work of adhesion is therefore $W_{\text{total}} = W_{\text{vdW}}^{\text{water}} + W_{\text{cap}} = 46 - 53\ \text{mJ/m}^2$. This results in an adhesion force, $F_{\text{JKR}}^{95\%\text{RH}} = 2.2 - 2.5\ \text{mN}$. These theoretical values are on the order of those obtained by experiment at the lowest preloads tested, as shown evidenced in Figure 2.13.

Gibbs' Adsorption Isotherm

The dependence of the adhesion force on relative humidity agrees with the Gibbs' adsorption isotherm

$$\Gamma = -\frac{1}{RT}\frac{\mathrm{d}\gamma}{\mathrm{d}(\ln c)} \qquad \text{(Eqn. 2.11)}$$

where Γ is the surface excess (the amount of species adsorbed per unit area), R is the gas constant, T is temperature, c is the species concentration (RH in the case of water), and γ is the surface energy. This predicts that the adsorption of species at the interface reduces the surface energy, and thus the adhesion force.

Adhesion force on microstructured surface

Comparing the adhesion behavior from the flat PDMS to the structured PDMS without shear (Figure 2.13B), we observe the same trend for the adhesion force as a function of humidity. As the relative humidity increases, the adhesive force decreases. There is no measurable adhesion when the contact is submerged (100 % RH).

The load dependence in the range 0 - 60 % RH is more nuanced than for the flat substrate, with a maximum appearing at L = 8 mN (Figure 2.13B). The initial increase in adhesion force with preload is common when testing microstructured samples on spherical test surfaces[87,90], as a greater number of fibers are brought in to contact. At higher preloads it is possible that elastic strain energy due to fiber bending promotes detachment and lowers the adhesion force.

The magnitude of the adhesion force on the microstructured surface is much lower when compared to the flat PDMS, likely due to lower true contact area. Counting the number of fibers in contact at an 8 mN preload under 0 % RH yields about 1920 fibers, that when multiplied by an estimated contact area of each fiber of 10 μm^2 gives a total contact area of 18,900 μm^2. This contact area can be compared to the apparent area of contact for the flat PDMS under the same preload and 0 % RH of about 402,000 μm^2. The ratio of the true contact area, 18,900 μm^2 /402,000 μm^2 = 0.047, is smaller than the ratio of the adhesion forces, 1.1 mN / 5.9 mN = 0.186. This non-linear scaling with area is predicted for contact splitting[91], however such a crude estimate should not be used to infer details of the mechanics beyond this observation. Furthermore, it is much more difficult to estimate the true area of contact under humid conditions when capillary bridges may be present. While low adhesion forces may seem to indicate poor performance, in the context of grip-release adhesives it is desirable to achieve low adhesive forces in the absence of appropriate engagement of the surfaces. In the gecko, this is referred to as the ‘non-adhesive default state’[92]. The results of Figure 2.13B demonstrate that non-adhesive behavior is in fact enhanced with increasing humidity in this synthetic adhesive.

The decrease in adhesion forces with increased humidity in both systems can be explained by the adsorption of water to the interface and formation of capillary bridges. This is supported by theoretical predictions for van der Waals and capillary force contributions for a sphere on flat geometry, which showed that the capillary adhesion force is lower than the van der Waals force in dry air. It is worth noting that this is not true of all contact angle combinations. In addition, the van der Waals force is expected to decrease with increasing humidity as the separating medium transitions from pure air, to humid air, to water. This effect has been described by Wan, Smith, and Lawn[93].

We shall see shortly for the microstructured sample, that the monotonic reduction in adhesion force with increasing relative humidity does not hold for all loading paths. The relative contributions of capillary and van der Waals forces are sensitive to both the microscale geometry of the fiber (controlling the effective contact area upon shearing) and to differences in the nanoscale roughness across the fiber. This is further discussed in the next section.

2.2.4.2 Load-shear-unload test

It is known that the detachment force in gecko setae is dependent on the direction of the load relative to the contacting surface, leading to a unique relationship between frictional and adhesive forces[6]. Modulating the frictional load by applying lateral displacement, the gecko can achieve states of high and low adhesion. With this comes the ability to achieve robust attachment to- and ease of detachment from- contacting surfaces.

Adhesion force

When we discussed adhesion forces on microstructured surfaces, we observed that the adhesion forces generated by the microfiber sample were low in the absence of shear, successfully mimicking one key feature of the gecko's adhesive system. We now wish to examine the ability to modulate adhesion forces in humid environments with lateral displacement (x^+ along the tilt or x^- against the tilt, as depicted in Figure 2.12). Adhesion forces were compared during shearing along the tilt of the fiber followed by separation, and shearing against the tilt followed by separation. Along the tilt is the intended high adhesion or 'grip' direction, where the adhesion force is denoted as F_{ad}^{+}. Against the tilt is the intended low adhesion or 'release' direction, where the adhesion force is denoted as F_{ad}^{-}.

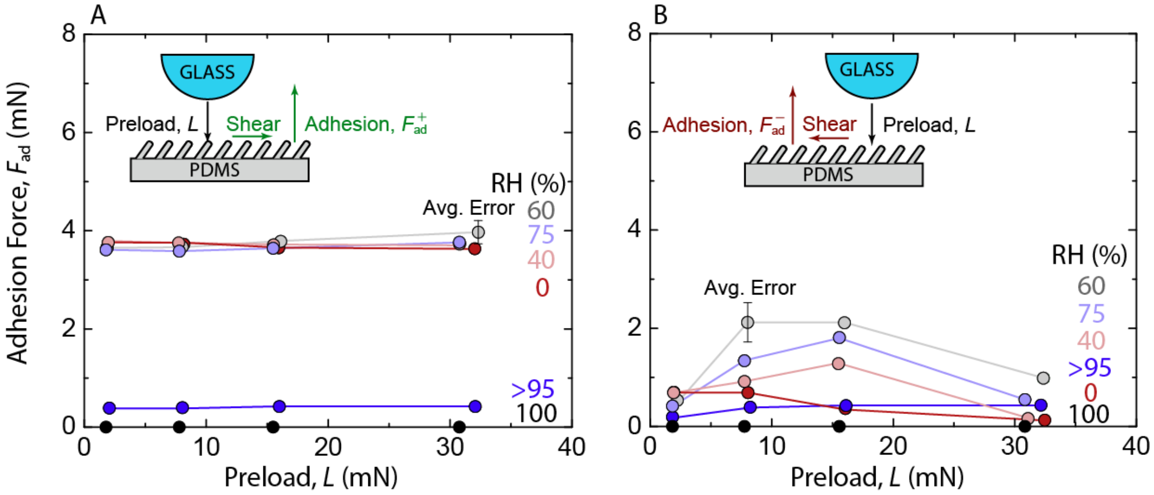

Figure 2.16 Load-shear-unload adhesion forces on microstructured PDMS as a function of preload, L. Results are presented for separation after shearing along the direction of tilt (A), adhesion force F_{ad}^{+}, and for separation after shearing against the direction of tilt (B), adhesion force F_{ad}^{-}. A lateral displacement of 150 μm was applied at a rate of 10 μm/s during the shear phase. The relative humidity is varied, with 0 % (red), 40 % (pink), 60 % (gray), 75 % (lavender), > 95 % (blue), and 100% underwater (black).

Shear with tilt – 'Grip state'

We first consider the adhesion force after shearing along the tilt direction, F_{ad}^{+}, shown in Figure 2.16A. No preload dependence is observed and the magnitude of the adhesion force is essentially constant until we reach > 95 % RH. At this point the adhesion force drops significantly. The lack of a preload dependence suggests that even minimal compression and shear is sufficient to deform the fibers and yield enough contact to engage adhesion with the flat side of the half cylinder fibers (depicted in Figure 2.11A). The combination of the flat sidewall and fiber tilt, as well as high fiber density, mean that upon shearing the effective contact area approaches that of flat PDMS. It is likely that this surface contact geometry does not change significantly during shearing as the preload is increased. Any additional strain energy due to fiber bending (seen to reduce the adhesion force at high preload in cases without shear and shear against tilt) appears to be compensated for by the increase in contact area. Interestingly the effect of humidity is negligible to 95 %, since without shear the flat surface exhibited a noticeable decrease in adhesion as the humidity was increased (Figure 2.14). Although the contact areas may be approximately equivalent, the microstructured surface results in a multi-asperity contact with effective roughness on the microscale. This will change the onset of capillary formation when compared to the flat surface. When tested underwater (100 % RH) there was no measurable adhesion force.

Shear against tilt – 'Release state'

The adhesion force when shearing against the tilt direction of the fibers and then separating, F_{ad}^{-}, exhibits further interesting phenomena. In the preload range 8 - 16 mN, a maximum exists in the adhesion force at intermediate humidity (40-75 % RH). This may correspond to a similar effect as described for adhesion of the microstructured sample without shear, where the use of a spherical probe dictates that as the preload is increased there is a competition between the number of contacts formed (increasing adhesion force) and the elastic strain energy stored in bending (reducing adhesion force).

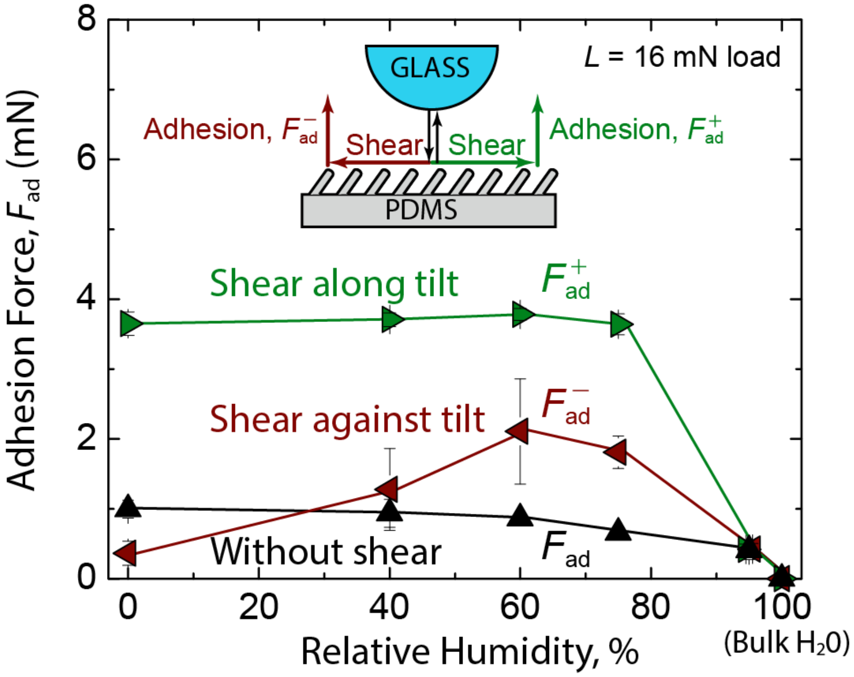

Figure 2.17 Load-shear-unload adhesion force on microstructured PDMS as a function of relative humidity for a preload L = 16 mN. Results are presented for separation after shearing along the fiber tilt, F_{ad}^{+} (green), shearing against the fiber tilt, F_{ad}^{-} (red), and without shear, F_{ad} (black). A lateral displacement of 150 µm was applied at a rate of 10 µm/s during the shear phase.

As the relative humidity increases, there is an intermediate maximum in the adhesion force after shearing against the tilt, F_{ad}^{-}, as seen in Figure 2.17. This is in stark contrast to the monotonic reduction observed without shear, and the humidity independent adhesion observed up to 75 % RH when shearing with the tilt.

The load path is known to control the region of the fiber which contacts the surface, and the effective area of this contact. There is a secondary effect which plays a key role in the trends observed, that being a different nanoscale roughness between the two regions. The SEM micrograph of Figure 2.18 shows a significant difference in the nanoscale roughness of the top of the fiber (smooth), compared to the curved side and flat side (rough).

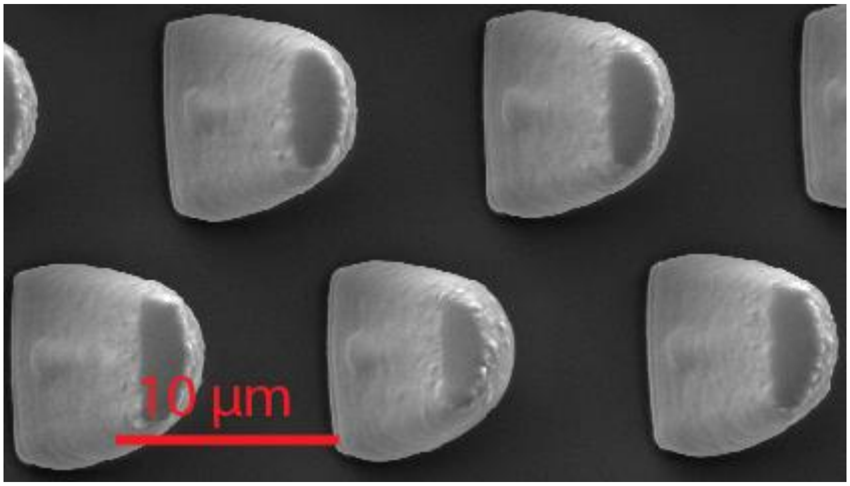

Figure 2.18 Top view SEM image depicting nanoscale roughness of tilted fibers on flat and curved faces (left side of tip vs right), compared to a much smoother tip.

The observation of a maximum adhesion at finite RH involving nanoscale rough or textured surfaces is well known (Section 17.11 of Intermolecular and Surface Forces, Israelachvili 2011)[28]. The maxima phenomenon has been measured in biological systems with nanoscale features on their foot pads such as the gecko[71], beetle[73], and spider[72], as well as for hard surfaces such as roughened silica substrates[68] and particle coated silicon[62]. Such nano-rough surfaces lead to small asperity junctions. At low humidity both the van der Waals and capillary force contributions are small. As the relative humidity increases, so too does the Kelvin radius, $r_\mathrm{K} \propto 1/\ln(\mathrm{RH})$. Capillary forces will increase the adhesion by bridging larger asperities. As the relative humidity approaches 100 % the contact becomes submerged and the capillary force is no longer present. The adhesion is once again low, due only to the van der Waals forces across water at small asperities. The magnitude of the capillary forces will depend on the exact scale of the surface roughness, as well as the water contact angle on each surface (Figure 2.15).

For shear against the tilt and without shear, the effective contact area at each fiber is small as reflected in the adhesion force at 0 % RH. The contact has more pronounced nanoscale roughness and the smallest true contact area when shearing against the tilt, leading to the lowest adhesion force in this case. When shearing against the tilt at intermediate humidity, the formation of capillaries at nanoscale asperities leads to a significant enhancement of the adhesion, while for the smooth contact (without shear) this increase is absent. The presence of nanoscale roughness on the flat side of the fiber appears to have a lesser role when the effective contact area at each fiber is large (i.e. when shearing along the tilt compared to against the tilt).

Friction force

In addition to examining the ability to modulate adhesion forces through shear, it is also important to examine the friction forces[8]. The friction forces give in-plane load bearing capability required for applications involving wall hanging, perching, or climbing. The static friction force is here defined as the parallel force required to initiate motion between two surfaces at rest. For the flat PDMS surface the static friction force is defined as $F_{||}$. For the microstructured surface the static friction force is defined as $F_{||}^{+}$ when shearing along the tilt of the fibers and $F_{||}^{-}$ when shearing against the tilt of the fibers.

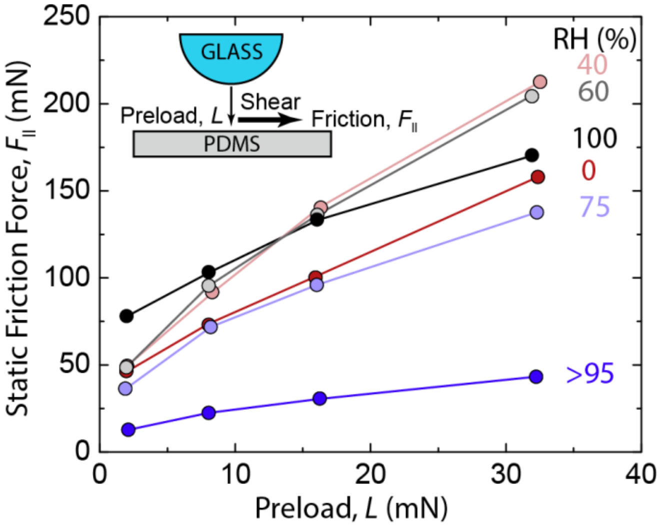

Figure 2.18 Static friction force, $F_{||}$ as a function of preload, L, on flat PDMS. Results are presented for the full range of relative humidity, 0 % (red), 40 % (pink), 60 % (gray), 75 % (lavender), > 95 % (blue), and 100% underwater (black). The friction force increases with increasing preload in a non-linear fashion.

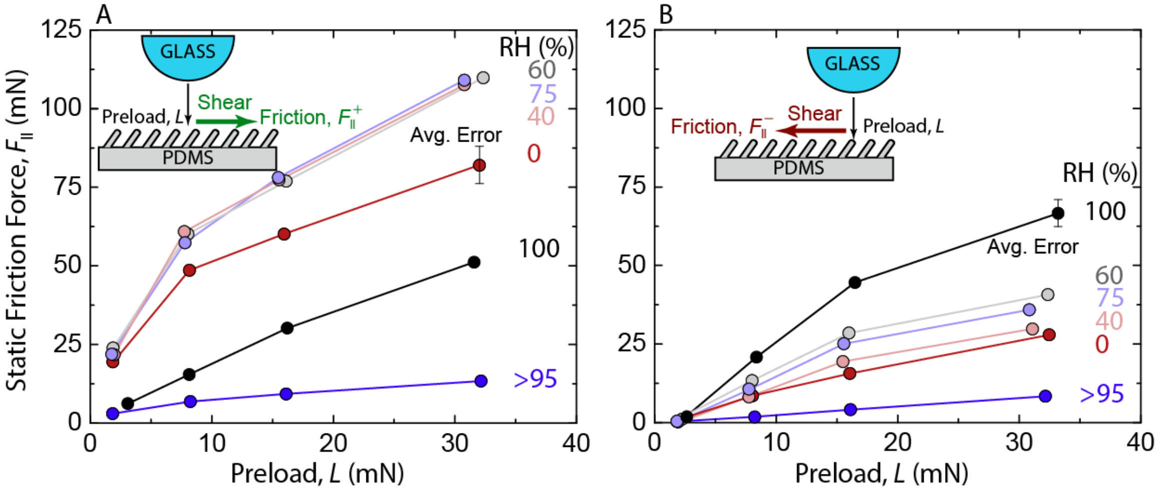

Figure 2.19 Static friction force, $F_{||}$, as a function of preload, L, on micro-structured PDMS for both shear with the tilt (A) and against the tilt (B). Results are presented for the full range of relative humidity, 0 % (red), 40 % (pink), 60 % (gray), 75 % (lavender), > 95 % (blue), and 100% underwater (black). In both cases the friction forces increase with increasing preload.

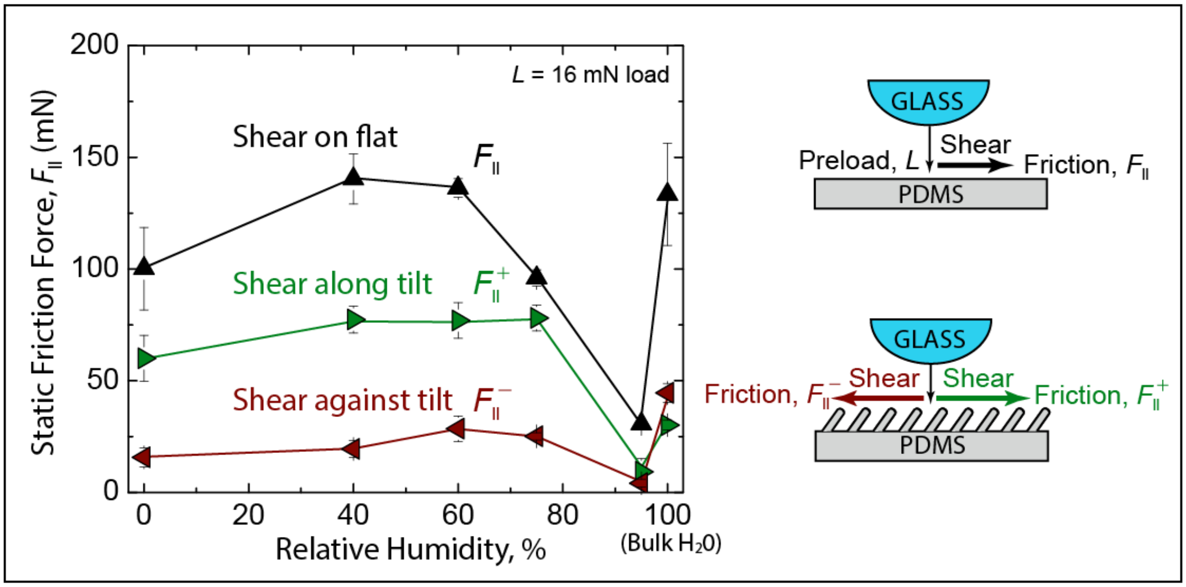

Figure 2.20 Load-shear static friction force as a function of relative humidity for a preload L = 16 mN. Results are presented for flat PDMS, $F_{||}$ (black), and for microstructured PDMS, shear along the tilt $F_{||}^{+}$ (green), and shear against the tilt $F_{||}^{-}$ (red).

At all humidity levels and for all surfaces tested, the static friction force increases with increasing preload, as seen in Figures 2.18 and 2.19. This trend is typical of the friction between solid surfaces. More interestingly, all surfaces exhibit an intermediate maximum in the friction force with increasing relative humidity as seen in Figure 2.20. A sharp increase is observed for the submerged contact. The static friction force was highest on the flat surface and lowest when shearing against the tilt of the fibers on the microstructured surface, following the same trend as the adhesion forces on each of these surfaces.

Similar to the initial increase in adhesion force with increasing humidity observed when shearing against the microfibers, the increase in static friction forces may be the result of a true contact area change. The presence of capillaries may increase the contact area, providing increased resistance to shear. However, there is a critical humidity level where the adsorbed water layer becomes thick enough to act as a lubricant, resulting in a reduction in the friction forces. When the experiment is performed underwater (100 % RH), the friction force increases greatly. This may be due to a large air bubble which formed between the two surfaces (seen visually). It was difficult to remove the air bubble, even with degassed water, due to the hydrophobicity of the PDMS sample. This hydrophobicity is enhanced in the case of the microstructured surface.

2.2.5 Discussion

The results obtained are of great interest when predicting the performance of elastomeric fibrillar adhesives in humid environments, particularly in relation to the ability to modulate adhesive forces by controlling the loading path. It is promising that the adhesion forces generated when shearing along the tilt (grip state) are not diminished until after 75 % RH is exceeded. In addition, the adhesion and friction forces are higher when shearing along the tilt compared to without shear or shearing against the tilt at these humidity levels.

Table 1 presents the ratio of adhesion forces for shearing along the tilt vs. shear against the tilt, $F_{\mathrm{ad}}^{+}/F_{\mathrm{ad}}^{-}$, and for shear along tilt vs. without shear, $F_{\mathrm{ad}}^{+}/F_{\mathrm{ad}}$. Interestingly, at intermediate humidity (40 - 75 % RH) the ratio is much higher for $F_{\mathrm{ad}}^{+}/F_{\mathrm{ad}}$ than $F_{\mathrm{ad}}^{+}/F_{\mathrm{ad}}^{-}$, meaning that it may be beneficial to tailor the loading path during detachment, only shearing to the point that fibers return the state they were in at first contact. For each humidity level from 0 % to 75%, one of the two loading paths for detachment (shear against the tilt or no shear) will always give a grip-release ratio of at least 4.0. When the humidity level reaches > 95 % the ratio drops to unity and the grip-release mechanism is compromised. In practice, it is likely that angled trajectories for attachment, grip, and release will be employed in every day operation. Adhesive performance when subject to these loading paths has been examined in dry environments[82], and extension to humid conditions is an interesting avenue for future work.

Table 2.3 Comparison of the ratio of adhesion forces for shearing along the tilt vs. shear against the tilt, $F_{\mathrm{ad}}^{+}/F_{\mathrm{ad}}^{-}$, and for shear along tilt vs. without shear, $F_{\mathrm{ad}}^{+}/F_{\mathrm{ad}}$, as well as friction along the tilt vs. friction against the tilt, $F_{||}^{+}/F_{||}^{-}$. Results are presented as a function of relative humidity (RH). The preload L = 16 mN.

RH (%)	**0**	**40**	**60**	**75**	**> 95**	**100**
$\boldsymbol{F_{ad}^{+}/F_{ad}^{-}}$	10.1 ± 5.2	2.9 ± 1.4	1.8 ± 0.7	2.0 ± 0.3	1.0 ± 0.4	0/0
$\boldsymbol{F_{ad}^{+}/F_{ad}}$	3.7 ± 0.6	4.0 ± 0.9	4.4 ± 0.5	5.5 ± 0.9	1.0 ± 0.5	0/0
$\boldsymbol{F_{||}^{+}/F_{||}^{-}}$	3.8 ± 1.7	4.0 ± 1.1	2.7 ± 0.8	3.1 ± 0.4	2.2 ± 2.0	0.7 ± 0.1

At 95 % humidity, the adhesion forces are equal to the case without shear, as seen in Figure 2.17. This would seem to indicate that the microfibers in contact relax to their initial state. This is facilitated by a thick water layer that behaves as a lubricant instead of an adhesive capillary bridge. This is further evidenced by the much-diminished friction forces seen in Figure 2.20. The ratio of friction forces, $F_{||}^{+}/F_{||}^{-}$, is greater than 1 except for when submerged underwater (100 % RH), in which case the resistance to shear was greatest against the tilt direction.

In all cases examined the adhesion force on the microstructured sample was lower than on the flat sample. However, the tilted half-cylinder microfibers demonstrated the ability to modulate adhesion force through tailoring of the loading path. The resulting adhesion forces for shear with the tilt approached those obtained on the flat surface. This is in addition to other benefits of fibrillar adhesives. Separation must be reinitiated at each fiber, increasing robustness to the propagation of detachment when compared to a single macroscopic contact. Furthermore, the ability of fibers to interpenetrate surface roughness can yield higher adhesion than on a flat sample when there is commensurability of the fiber size and contacting asperity size. The inability to generate higher adhesion forces than on a flat control is unlikely to hold for all contacting surfaces, particularly as additional levels of structural hierarchy (length-scales of fiber) are included in the microstructure of the adhesive.

2.2.6 Conclusion

In summary, there are many subtleties in the adhesion and friction forces generated by the anisotropic (tilted half cylinder) microfibrillar PDMS surface examined. These result from the combined effects of preload, sliding direction, nanoscale and microscale geometry, and relative humidity. The friction forces and the release state adhesion force, for example, exhibit maxima at intermediate relative humidity, between 40 % and 75 %. The adhesion force is approximately preload independent when shearing along the tilt at all humidity levels examined. Overall it has been demonstrated that the microstructured surface shows great promise for application in humid environments. Increasing the relative humidity results in differences in the relative contributions of van der Waals and capillary forces, leading to a monotonic reduction in the adhesion force on a flat PDMS control. The microstructured surface exhibits similar behavior in the absence of shear. However, by shearing along the tilt of the fiber the adhesion force approaches that obtained on the flat surface and is approximately constant to 75 % RH. Furthermore, in the absence of shear or with shear against the tilt the adhesion force is much reduced. Grip and release can therefore be achieved by tailoring the loading path. Only at very high relative humidity, > 95 % and for a submerged contact, is there no longer a distinct high adhesion and low adhesion state.

References

(1) Autumn, K.; Liang, Y. A.; Hsieh, S. T.; Zesch, W.; Chan, W. P.; Kenny, T. W.; Fearing, R.; Full, R. J. Adhesive Force of a Single Gecko Foot-Hair. *Nature* **2000**, *405* (6787), 681–685.

(2) Autumn, K.; Peattie, A. M. Mechanisms of Adhesion in Geckos. *Integr. Comp. Biol.* **2002**, *42* (6), 1081–1090.

(3) Autumn, K.; Sitti, M.; Liang, Y. A.; Peattie, A. M.; Hansen, W. R.; Sponberg, S.; Kenny, T. W.; Fearing, R.; Israelachvili, J. N.; Full, R. J. Evidence for van Der Waals Adhesion in Gecko Setae. *Proc. Natl. Acad. Sci. U. S. A.* **2002**, *99* (19), 12252–12256.

(4) Das, S.; Chary, S.; Yu, J.; Tamelier, J.; Turner, K. L.; Israelachvili, J. N. JKR Theory for the Stick-Slip Peeling and Adhesion Hysteresis of Gecko Mimetic Patterned Surfaces with a Smooth Glass Surface. *Langmuir* **2013**, *29* (48), 15006–15012.

(5) Gillies, A. G.; Fearing, R. S. Simulation of Synthetic Gecko Arrays Shearing on Rough Surfaces. *J. R. Soc. Interface* **2014**, *11* (95).

(6) Autumn, K.; Dittmore, A.; Santos, D.; Spenko, M.; Cutkosky, M. Frictional Adhesion: A New Angle on Gecko Attachment. *J. Exp. Biol.* **2006**, *209* (Pt 18), 3569–3579.

(7) Puthoff, J. B.; Holbrook, M.; Wilkinson, M. J.; Jin, K.; Pesika, N. S.; Autumn, K. Dynamic Friction in Natural and Synthetic Gecko Setal Arrays. *Soft Matter* **2013**, *9* (19), 4855.

(8) Zhao, B.; Pesika, N.; Rosenberg, K.; Tian, Y.; Zeng, H.; McGuiggan, P.; Autumn, K.; Israelachvili, J. Adhesion and Friction Force Coupling of Gecko Setal Arrays:

Implications for Structured Adhesive Surfaces. *Langmuir* **2008**, *24* (4), 1517–1524.

(9) Aránzazu del Campo, *; Christian Greiner, A.; Arzt, E. Contact Shape Controls Adhesion of Bioinspired Fibrillar Surfaces. **2007**.

(10) Gao, H.; Wang, X.; Yao, H.; Gorb, S.; Arzt, E. Mechanics of Hierarchical Adhesion Structures of Geckos. *Mech. Mater.* **2005**, *37* (2–3), 275–285.

(11) Peng, Z.; Chen, S.; Kligerman, Y.; Gorb, S. N.; Arzt, E.; McGuiggan, P.; Autumn, K.; Israelachvili, J. N.; Israelachvili, J. N.; Full, R. J. The Effect of Geometry on the Adhesive Behavior of Bio-Inspired Fibrils. *Soft Matter* **2012**, *8* (38), 9864.

(12) Gravish, N.; Wilkinson, M.; Sponberg, S.; Parness, A.; Esparza, N.; Soto, D.; Yamaguchi, T.; Broide, M.; Cutkosky, M.; Creton, C.; Autumn, K. Rate-Dependent Frictional Adhesion in Natural and Synthetic Gecko Setae. *J. R. Soc. Interface* **2010**, *7* (43), 259–269.

(13) Cañas, N.; Kamperman, M.; Völker, B.; Kroner, E.; McMeeking, R. M.; Arzt, E. Effect of Nano- and Micro-Roughness on Adhesion of Bioinspired Micropatterned Surfaces. *Acta Biomater.* **2012**, *8* (1), 282–288.

(14) Geim, A. K.; Dubonos, S. V.; Grigorieva, I. V.; Novoselov, K. S.; Zhukov, A. A.; Shapoval, S. Y. Microfabricated Adhesive Mimicking Gecko Foot-Hair. *Nat. Mater.* **2003**, *2* (7), 461–463.

(15) Murphy, M. P.; Kim, S.; Sitti, M. Enhanced Adhesion by Gecko-Inspired Hierarchical Fibrillar Adhesives. *ACS Appl. Mater. Interfaces* **2009**, *1* (4), 849–855.

(16) Yu, J.; Chary, S.; Das, S.; Tamelier, J.; Pesika, N. S.; Turner, K. L.; Israelachvili, J. N. Gecko-Inspired Dry Adhesive for Robotic Applications. *Adv. Funct. Mater.* **2011**, *21* (16), 3010–3018.

(17) Zhou, M.; Pesika, N.; Zeng, H.; Wan, J.; Zhang, X.; Meng, Y.; Wen, S.; Tian, Y. Design of Gecko-Inspired Fibrillar Surfaces with Strong Attachment and Easy-Removal Properties: A Numerical Analysis of Peel-Zone. *J. R. Soc. Interface* **2012**, *9* (75).

(18) Xue, L.; Kovalev, A.; Thöle, F.; Rengarajan, G. T.; Steinhart, M.; Gorb, S. N. Tailoring Normal Adhesion of Arrays of Thermoplastic, Spring-like Polymer Nanorods by Shaping Nanorod Tips. *Langmuir* **2012**, *28* (29), 10781–10788.

(19) Heepe, L.; Gorb, S. N. Biologically Inspired Mushroom-Shaped Adhesive Microstructures. *Annu. Rev. Mater. Res.* **2014**, *44* (1), 173–203.

(20) Kim, Y.; Claus, R. K.; Limanto, F.; Fearing, R. S.; Maboudian, R. Friction Characteristics of Polymeric Nanofiber Arrays against Substrates with Tailored Geometry. *Langmuir* **2013**, *29* (26), 8395–8401.

(21) Rodriguez, I.; Lim, C. T.; Natarajan, S.; Ho, A. Y. Y.; Van, E. L.; Elmouelhi, N.; Low, H. Y.; Vyakarnam, M.; Cooper, K. Shear Adhesion Strength of Gecko-Inspired Tapes on Surfaces with Variable Roughness. *J. Adhes.* **2013**, *89* (12), 921–936.

(22) Asbeck, A.; Dastoor, S.; Parness, A.; Fullerton, L.; Esparza, N.; Soto, D.; Heyneman, B.; Cutkosky, M. Climbing Rough Vertical Surfaces with Hierarchical Directional Adhesion. In *2009 IEEE International Conference on Robotics and Automation*; IEEE, 2009; pp 2675–2680.

(23) Chen, S.; Gao, H. Bio-Inspired Mechanics of Reversible Adhesion: Orientation-Dependent Adhesion Strength for Non-Slipping Adhesive Contact with Transversely Isotropic Elastic Materials. *J. Mech. Phys. Solids* **2007**, *55* (5), 1001–1015.

(24) Yao, H.; Rocca, G. Della; Guduru, P. .; Gao, H. Adhesion and Sliding Response of a

Biologically Inspired Fibrillar Surface: Experimental Observations. *J. R. Soc. Interface* **2008**, *5* (24).

(25) Tambe, N. S.; Bhushan, B. Friction Model for the Velocity Dependence of Nanoscale Friction. *Nanotechnology* **2005**, *16* (10), 2309–2324.

(26) Yoshizawa, H.; Israelachvili, J. Fundamental Mechanisms of Interfacial Friction. 2. Stick-Slip Friction of Spherical and Chain Molecules. *J. Phys. Chem.* **1993**, *97* (43), 11300–11313.

(27) Israelachvili, J.; Berman, A. Irreversibility, Energy Dissipation, and Time Effects in Intermolecular and Surface Interactions. *Isr. J. Chem.* **1995**, *35* (1), 85–91.

(28) Israelachvili, J. N. *Intermolecular and Surface Forces: Revised Third Edition*; Academic Press, 2011.

(29) Yu, J.; Chary, S.; Das, S.; Tamelier, J.; Turner, K. L.; Israelachvili, J. N. Friction and Adhesion of Gecko-Inspired PDMS Flaps on Rough Surfaces. *Langmuir* **2012**, *28* (31), 11527–11534.

(30) Israelachvili, J. . Recent Advances in the Surface Forces Apparatus (SFA) Technique. *Reports Prog. Phys.* **2010**, *73* (3).

(31) Berman, A. D.; Ducker, W. A.; Israelachvili, J. N. Origin and Characterization of Different Stick−Slip Friction Mechanisms †. *Langmuir* **1996**, *12* (19), 4559–4563.

(32) Yoshizawa, H.; McGuiggan, P.; Israelachvili, J. Identification of a Second Dynamic State during Stick-Slip Motion. *Science* **1993**, *259* (5099), 1305–1308.

(33) *Fundamentals of Friction and Wear*; Gnecco, E., Meyer, E., Eds.; NanoScience and Technology; Springer Berlin Heidelberg: Berlin, Heidelberg, 2007.

(34) Scholz, C. H.; Engelder, J. T. The Role of Asperity Indentation and Ploughing in

Rock Friction — I. *Int. J. Rock Mech. Min. Sci. Geomech. Abstr.* **1976**, *13* (5), 149–154.

(35) Byerlee, J. D. Theory of Friction Based on Brittle Fracture. *J. Appl. Phys.* **1967**, *38* (7), 2928–2934.

(36) Carlos Miguez Suarez, J.; Biasotto Mano, E. Brittle–ductile Transition of Gamma-Irradiated Recycled Polyethylenes Blend. *Polym. Test.* **2000**, *19* (6), 607–616.

(37) Scholz, C. H. (Christopher H. . *The Mechanics of Earthquakes and Faulting.*; Cambridge University Press, 2002.

(38) Schallamach, A. A Theory of Dynamic Rubber Friction. *Wear* **1963**, *6* (5), 375–382.

(39) Schallamach, A. How Does Rubber Slide? *Wear* **1971**, *17* (4), 301–312.

(40) Briggs, G. A. D.; Briscoe, B. J. The Dissipation of Energy in the Friction of Rubber. *Wear* **1975**, *35* (2), 357–364.

(41) Golden, J. M. A Molecular Theory of Adhesive Rubber Friction. *J. Phys. A. Math. Gen.* **1975**, *8* (6), 966–979.

(42) Hiller, U. Untersuchungen Zum Feinbau Und Zur Funktion Der Haftborsten von Reptilien. *Zeitschrift fur Morphol. der Tiere* **1968**, *62* (4), 307–362.

(43) Tian, Y.; Pesika, N.; Zeng, H.; Rosenberg, K.; Zhao, B.; McGuiggan, P.; Autumn, K.; Israelachvili, J. Adhesion and Friction in Gecko Toe Attachment and Detachment. *Proc. Natl. Acad. Sci. U. S. A.* **2006**, *103* (51), 19320–19325.

(44) Zhou, M.; Pesika, N.; Zeng, H.; Tian, Y.; Israelachvili, J. Recent Advances in Gecko Adhesion and Friction Mechanisms and Development of Gecko-Inspired Dry Adhesive Surfaces. *Friction* **2013**, *1* (2), 114–129.

(45) Bartlett, M. D.; Crosby, A. J. High Capacity, Easy Release Adhesives From

Renewable Materials. *Adv. Mater.* **2014**, *26* (21), 3405–3409.

(46) Paretkar, D.; Kamperman, M.; Martina, D.; Zhao, J.; Creton, C.; Lindner, A.; Jagota, A.; McMeeking, R.; Arzt, E. Preload-Responsive Adhesion: Effects of Aspect Ratio, Tip Shape and Alignment. *J. R. Soc. Interface* **2013**, *10* (83).

(47) Krahn, J.; Liu, Y.; Sadeghi, A.; Menon, C. A Tailless Timing Belt Climbing Platform Utilizing Dry Adhesives with Mushroom Caps. *Smart Mater. Struct.* **2011**, *20* (11), 115021.

(48) Spenko, M.; Trujillo, S.; Heyneman, B.; Santos, D.; Cutkosky, M. R. Smooth Vertical Surface Climbing With Directional Adhesion. *IEEE Trans. Robot.* **2008**, *24* (1), 65–74.

(49) Cai, S.; Bhushan, B. Effects of Symmetric and Asymmetric Contact Angles and Division of Menisci during Separation. *Philos. Mag.* **2007**, *87* (35), 5505–5522.

(50) Butt, H.-J.; Kappl, M. Normal Capillary Forces. *Adv. Colloid Interface Sci.* **2009**, *146* (1–2), 48–60.

(51) Carter, W. C. The Forces and Behavior of Fluids Constrained by Solids. *Acta Metall.* **1988**, *36* (8), 2283–2292.

(52) De Souza, E. J.; Brinkmann, M.; Mohrdieck, C.; Crosby, A.; Arzt, E. Capillary Forces between Chemically Different Substrates. *Langmuir* **2008**, *24* (18), 10161–10168.

(53) Fisher, L. R.; Israelachvili, J. N. Direct Experimental Verification of the Kelvin Equation for Capillary Condensation. *Nature* **1979**, *277* (5697), 548–549.

(54) Fortes, M. . Axisymmetric Liquid Bridges between Parallel Plates. *J. Colloid Interface Sci.* **1982**, *88* (2), 338–352.

(55) Sedin, D. L.; Rowlen, K. L. Adhesion Forces Measured by Atomic Force Microscopy in Humid Air. *Anal. Chem.* **2000**, *72* (10), 2183–2189.

(56) Willett, C. D.; Adams, M. J.; Johnson, S. A.; Seville, J. P. K. Capillary Bridges between Two Spherical Bodies. *Langmuir* **2000**, *16* (24), 9396–9405.

(57) Xiao, X.; Qian, L. Investigation of Humidity-Dependent Capillary Force. *Langmuir* **2000**, *16* (21), 8153–8158.

(58) Ando, Y. The Effect of Relative Humidity on Friction and Pull-off Forces Measured on Submicron-Size Asperity Arrays. *Wear* **2000**, *238* (1), 12–19.

(59) Ata, A.; Rabinovich, Y. I.; Singh, R. K. Role of Surface Roughness in Capillary Adhesion. *J. Adhes. Sci. Technol.* **2002**, *16* (4), 337–346.

(60) de Boer, M. P.; de Boer, P. C. T. Thermodynamics of Capillary Adhesion between Rough Surfaces. *J. Colloid Interface Sci.* **2007**, *311* (1), 171–185.

(61) de Lazzer, A.; Dreyer, M.; Rath, H. J. Particle−Surface Capillary Forces. *Langmuir* **1999**, *15* (13), 4551–4559.

(62) Farshchi-Tabrizi, M.; Kappl, M.; Cheng, Y.; Gutmann, J.; Butt, H.-J. On the Adhesion between Fine Particles and Nanocontacts: An Atomic Force Microscope Study. *Langmuir* **2006**, *22* (5), 2171–2184.

(63) Feiler, A. A.; Jenkins, P.; Rutland, M. W. Effect of Relative Humidity on Adhesion and Frictional Properties of Micro- and Nano-Scopic Contacts. *J. Adhes. Sci. Technol.* **2005**, *19* (3–5), 165–179.

(64) Huang, C.-C.; Chen, L.; Gu, X.; Zhao, M.; Nguyen, T.; Lee, S. The Effects of Humidity and Surface Free Energy on Adhesion Force between Atomic Force Microscopy Tip and a Silane Self-Assembled Monolayer Film. *J. Mater. Res.* **2011**,

25 (3), 556–562.

(65) Köber, M.; Sahagún, E.; García-Mochales, P.; Briones, F.; Luna, M.; Sáenz, J. J. Nanogeometry Matters: Unexpected Decrease of Capillary Adhesion Forces with Increasing Relative Humidity. *Small* **2010**, *6* (23), 2725–2730.

(66) Marmur, A. Tip-Surface Capillary Interactions. *Langmuir* **1993**, *9* (7), 1922–1926.

(67) Persson, B. N. J. Capillary Adhesion between Elastic Solids with Randomly Rough Surfaces. *J. Phys. Condens. Matter* **2008**, *20* (31), 315007.

(68) Rabinovich, Y.; Adler, J.; Esayunar, M.; Ata, A.; Singh, R.; Moudgil, B. Capillary Forces between Surfaces with Nanoscale Roughness. *Adv. Colloid Interface Sci.* **2002**, *96* (1–3), 213–230.

(69) Kim, T. W.; Bhushan, B. The Adhesion Model Considering Capillarity for Gecko Attachment System. *J. R. Soc. Interface* **2008**, *5* (20), 319–327.

(70) Huber, G.; Mantz, H.; Spolenak, R.; Mecke, K.; Jacobs, K.; Gorb, S. N.; Arzt, E. Evidence for Capillarity Contributions to Gecko Adhesion from Single Spatula Nanomechanical Measurements. *Proc. Natl. Acad. Sci. U. S. A.* **2005**, *102* (45), 16293–16296.

(71) Niewiarowski, P. H.; Lopez, S.; Ge, L.; Hagan, E.; Dhinojwala, A. Sticky Gecko Feet: The Role of Temperature and Humidity. *PLoS One* **2008**, *3* (5), e2192.

(72) Wolff, J. O.; Gorb, S. N. The Influence of Humidity on the Attachment Ability of the Spider Philodromus Dispar (Araneae, Philodromidae). *Proceedings. Biol. Sci.* **2012**, *279* (1726), 139–143.

(73) Heepe, L.; Wolff, J. O.; Gorb, S. N. Influence of Ambient Humidity on the Attachment Ability of Ladybird Beetles (Coccinella Septempunctata). *Beilstein J.*

Nanotechnol. **2016**, *7*, 1322–1329.

(74) Pesika, N. S.; Zeng, H.; Kristiansen, K.; Zhao, B.; Tian, Y.; Autumn, K.; Israelachvili, J. Gecko Adhesion Pad: A Smart Surface? *J. Phys. Condens. Matter* **2009**, *21* (46), 464132.

(75) Puthoff, J. B.; Prowse, M. S.; Wilkinson, M.; Autumn, K. Changes in Materials Properties Explain the Effects of Humidity on Gecko Adhesion. *J. Exp. Biol.* **2010**, *213* (Pt 21), 3699–3704.

(76) Buhl, S.; Greiner, C.; Campo, A. del; Arzt, E. Humidity Influence on the Adhesion of Biomimetic Fibrillar Surfaces. *Int. J. Mater. Res.* **2009**, *100* (8), 1119–1126.

(77) Greiner, C.; Spolenak, R.; Arzt, E. Adhesion Design Maps for Fibrillar Adhesives: The Effect of Shape. *Acta Biomater.* **2009**, *5* (2), 597–606.

(78) Stark, A. Y.; Klittich, M. R.; Sitti, M.; Niewiarowski, P. H.; Dhinojwala, A.; Suh, K. Y. The Effect of Temperature and Humidity on Adhesion of a Gecko-Inspired Adhesive: Implications for the Natural System. *Sci. Rep.* **2016**, *6* (1), 30936.

(79) Xue, L.; Kovalev, A.; Dening, K.; Eichler-Volf, A.; Eickmeier, H.; Haase, M.; Enke, D.; Steinhart, M.; Gorb, S. N. Reversible Adhesion Switching of Porous Fibrillar Adhesive Pads by Humidity. *Nano Lett.* **2013**, *13* (11), 5541–5548.

(80) Xue, L.; Kovalev, A.; Eichler-Volf, A.; Steinhart, M.; Gorb, S. N. Humidity-Enhanced Wet Adhesion on Insect-Inspired Fibrillar Adhesive Pads. *Nat. Commun.* **2015**, *6*, 6621.

(81) Tamelier, J.; Chary, S.; Turner, K. L. Vertical Anisotropic Microfibers for a Gecko-Inspired Adhesive. *Langmuir* **2012**, *28* (23), 8746–8752.

(82) Tamelier, J.; Chary, S.; Turner, K. L. Importance of Loading and Unloading

Procedures for Gecko-Inspired Controllable Adhesives. *Langmuir* **2013**, *29* (34), 10881–10890.

(83) Chary, S.; Tamelier, J.; Turner, K. A Microfabricated Gecko-Inspired Controllable and Reusable Dry Adhesive. *Smart Mater. Struct.* **2013**, *22* (2), 25013.

(84) Greenspan, L. Humidity Fixed Points of Binary Saturated Aqueous Solutions. *J. Res. Natl. Bur. Stand. A, Phys. Chem. 81a* (1), 89–96.

(85) Das, S.; Cadirov, N.; Chary, S.; Kaufman, Y.; Hogan, J.; Turner, K. L.; Israelachvili, J. N. Stick-Slip Friction of Gecko-Mimetic Flaps on Smooth and Rough Surfaces. *J. R. Soc. Interface* **2015**, *12* (104), 20141346-.

(86) Barreau, V.; Hensel, R.; Guimard, N. K.; Ghatak, A.; McMeeking, R. M.; Arzt, E. Fibrillar Elastomeric Micropatterns Create Tunable Adhesion Even to Rough Surfaces. *Adv. Funct. Mater.* **2016**, *26* (26), 4687–4694.

(87) Kroner, E.; Maboudian, R.; Arzt, E. Adhesion Characteristics of PDMS Surfaces During Repeated Pull-Off Force Measurements. *Adv. Eng. Mater.* **2010**, *12* (5), 398–404.

(88) Johnson, K. L.; Kendall, K.; Roberts, A. D. Surface Energy and the Contact of Elastic Solids. *Proc. R. Soc. A Math. Phys. Eng. Sci.* **1971**, *324* (1558), 301–313.

(89) Tabor, D. Surface Forces and Surface Interactions. *J. Colloid Interface Sci.* **1977**, *58* (1), 2–13.

(90) Greiner, C.; del Campo, A.; Arzt, E. Adhesion of Bioinspired Micropatterned Surfaces: Effects of Pillar Radius, Aspect Ratio, and Preload. *Langmuir* **2007**, *23* (7), 3495–3502.

(91) Kamperman, M.; Kroner, E.; del Campo, A.; McMeeking, R. M.; Arzt, E. Functional

Adhesive Surfaces with “Gecko” Effect: The Concept of Contact Splitting. *Adv. Eng. Mater.* **2010**, *12* (5), 335–348.

(92) Autumn, K.; Hansen, W. Ultrahydrophobicity Indicates a Non-Adhesive Default State in Gecko Setae. *J. Comp. Physiol. A. Neuroethol. Sens. Neural. Behav. Physiol.* **2006**, *192* (11), 1205–1212.

(93) Wan, K.-T.; Smith, D. T.; Lawn, B. R. Fracture and Contact Adhesion Energies of Mica-Mica, Silica-Silica, and Mica-Silica Interfaces in Dry and Moist Atmospheres. *J. Am. Ceram. Soc.* **1992**, *75* (3), 667–676.

Chapter 3: Characterizing dynamic, high-frequency friction in lubricating complex-fluid thin films between viscoelastic surfaces

3.1 Abstract

Friction coefficients alone provide a highly oversimplified characterization of sliding surfaces as they are rarely truly *constant* but vary with load, velocity, previous history, and sliding time. Perhaps most importantly, they do not represent the *dynamics* captured in a friction trace, such as stiction and stick-slip sliding, which are responsible for phenomena such as damage, wear, sound, and sensory perception (e.g., feel, food texture). Using a new 'Rotating Disk' attachment for the Surface Forces Apparatus (RD-SFA), we have studied the friction frequency response from 0-2,500 Hz under high sliding velocities/shear rates. The RD-SFA is capable of rotating and shearing two surfaces at velocities from mm/s to m/s in controlled temperature, humidity, and vapor composition environments. Friction experiments on thin complex fluid films were performed at varying loads (20 to 320 mN) and velocities (1 to 40 mm/s) with a 20-microsecond sampling time. At such (and especially higher) velocities, analytical methodologies such as 'wavelet decompositions' can be used to explore the time evolution of the friction dynamics captured in a friction trace. Such techniques are general and enable the unambiguous characterization of any system fluctuations or resonant vibrations associated with stick-slip sliding and other 'intermittent friction' behaviors. We present results for a soft viscoelastic polymer interface of PDMS-on-PDMS lubricated with a variety of 'everyday' fluids (oils, creams, moisturizers, etc.), to illustrate the complex and varied

dynamic behavior that can arise under different experimental or environmental conditions and that have implications for damage, wear, and sensory perception.

3.2 Introduction

Everyday fluids are heterogeneous and complex, and as lubricants will give rise to time-dependent, intermittent, and non-Amontonian friction behavior. Such fluids range from skin care products (creams, moisturizers, etc.), soaps, and detergents, to device lubricants (motor oil, coolants, etc.), which contain several constituents at the molecular and colloidal scale. Insights into the frictional behavior of everyday fluids are important to extract essential information about sensory perception, feel, and wear and friction control[1–4]. However, the complexity in the friction forces, such as fluctuations, has made a standardized analysis scheme difficult to propose, and simpler coarse models are still in use.

Although fluctuations in friction forces with time are commonly observed, the average friction force is generally used to describe friction behavior. The most common way to quantify friction is through a friction coefficient, $\mu = F/L$, or simply the friction force (the resistive parallel force between sliding surfaces, F) divided by the load (the perpendicular or normal force, L). This metric can give insight into energy loss due to frictional processes but tends not to be constant with varying sliding conditions, including loads and velocities, especially in the presence of adhesion forces, and for lubricated (viscous, rheological) systems[5–7].

Common systems used to study friction and lubrication in engineering and manufacturing settings include four ball[8], twin disk[9], ball-on-disk and pin-on-disk tribometers[9]. These systems can achieve a large range of speeds (mm/s to m/s) and loads (mN to 10s of N), but dynamic friction is rarely considered during analysis[10,11]. Atomic Force

Microscopy (AFM) is used to measure friction on the molecular level, but, due to the geometry of the cantilever, has difficulties decoupling parallel (F) and normal (L) forces[12]. Also, friction experiments with a highly pointed AFM tip do not easily translate to the more applicable scenario of two extended (macroscopic) surfaces shearing. Most friction studies are performed to create a Stribeck curve[12], which evaluates the friction coefficient, μ, over a wide range of sliding velocities. However, many of these studies only analyze friction behavior at a single, constant load. Also, these relationships only consider the average friction force – ignoring the subtle but important low and high frequency components that can vary from 10^{-3} – 10^{4} Hz.

Since friction behavior can be quite complex (due to system parameters such as: (1) surface chemical and physical features, (2) fluid and molecular heterogeneities, and (3) temperature fluctuations), there is no simple relationship that predicts *dynamic* friction behavior (changes in friction with time), which is often over-simplified or ignored. Historically, the fluctuations in friction were assumed to be noise (random fluctuations) in the measurement. Yet frictional systems exhibit everything from smooth sliding, to resonant vibrations (sinusoidal), intermittent fluctuations (chaotic), and stick-slip friction (periodic, non-sinusoidal)[13]. Dynamic friction has been shown to be prevalent in many phenomena including sensory perception[14–16] (mouth feel, sound, touch), as well as the explanation for shudder[17] or noise in car engines, and as a damage predictor in systems such as hard drives[18] and articular cartilage[19]. These effects can be much better understood by studying dynamic friction compared to the average values in a friction experiment or measurement.

To more fully characterize friction behavior and perform high-speed, high-sensitivity friction measurements (to determine dynamic or transient effects), we have developed a new rotating disk attachment for the surface forces apparatus (RD-SFA), shown in Figure 3.1 and described below. The newly developed rotating disk attachment utilizes interchangeable motors that can go from speeds of mm/s to m/s with a high torque threshold and measures high resolution friction forces and loads. The motion of the disk can be arbitrarily controlled, including continuous sliding, oscillatory, and back-and-forth motion. We also introduce a complementary approach for analyzing high speed friction data using 'wavelet transforms'[20–22] to determine the variation of frequency components with time, as well as their relative magnitudes. This method allows for unambiguous differentiation between oscillatory responses from natural, e.g., mechanical resonance, frequencies in the whole system and stick-slip friction that arises from surface interactions. We have performed friction experiments on several complex fluid mixtures, and characterized them with these methods, quantifying their differing complex dynamic responses at various velocities and loads.

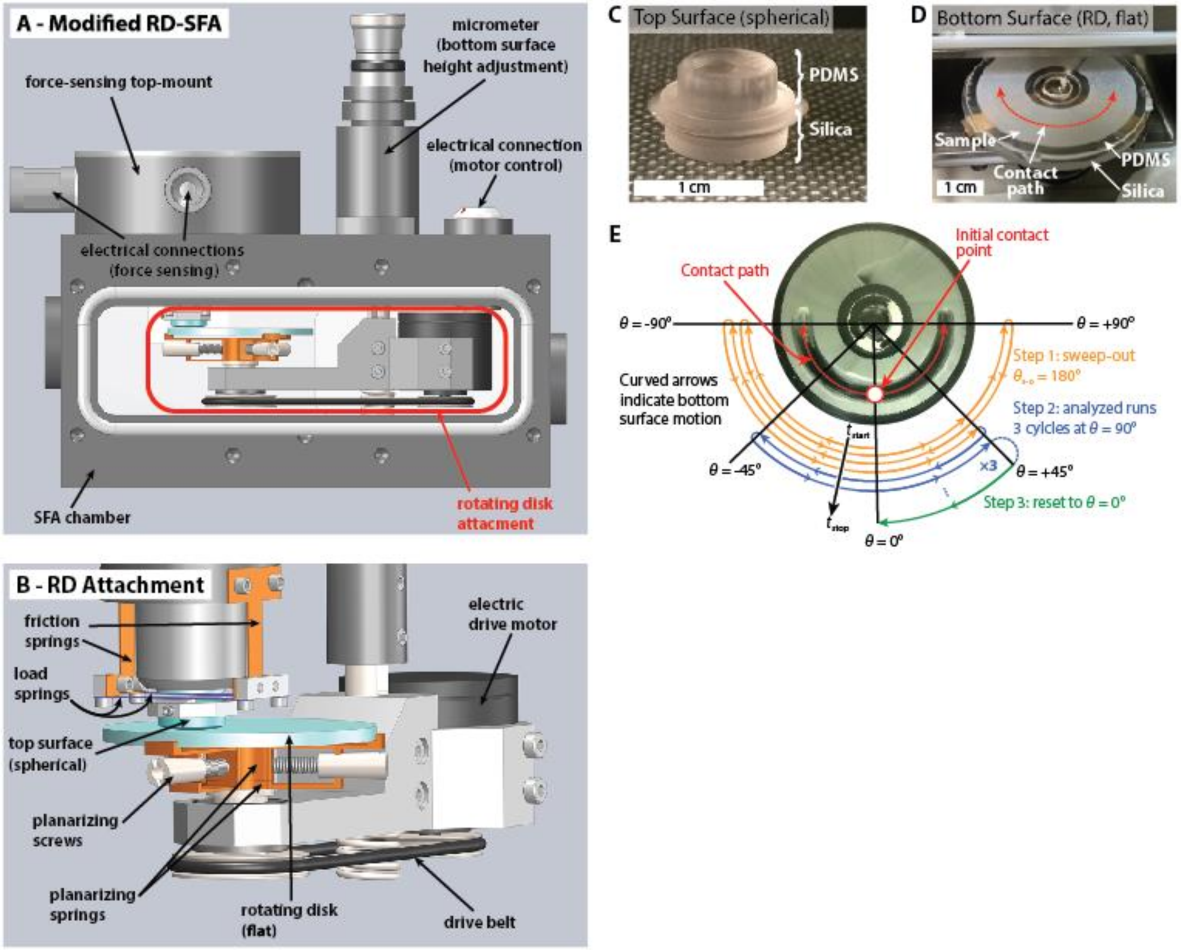

Figure 3.1 The Rotating Disk Surface Forces Apparatus (RD-SFA) and surfaces used. **A**. Schematic of the RD-SFA. The rotating disk attachment fits into the chamber of an SFA2000 (Surforce LLC). The height of the bottom (flat) rotating surface can be adjusted with a micrometer to load and separate the surfaces. **B**. Detailed view of the RD attachment. A rotating stage, driven by an electric servo-motor and pully system, holds the bottom surface (a 40-mm diameter sapphire disk). The stage can be planarized by splaying three pairs of springs with adjustable conical screws. The upper (spherical) surface is mounted on a stage with both friction (orange) and load (blue) sensing springs, each equipped with metal foil strain gauges. **C**. The top surface used in these experiments is a spherical PDMS cap attached to a typical silica disk used in SFA experiments. **D**. The bottom surface is a flat PDMS (with a 50-micron trough to hold the sample fluid) on a 40 mm diameter silica sapphire disk. **E**. Sweeping path used in the experimental procedure: an initial 180° "sweep-out" is performed followed by three cycles at 90° in which the analyzed forces were obtained.

3.3 Materials and Methods

The new rotating disk surface forces apparatus (RD-SFA, Figure 3.1) builds upon an earlier design[23]. Previously, the rotating disk bottom surface was directly attached to the motor, requiring the use of small motors, making it difficult to achieve a large range of velocities and loads. This choice of motor placement also limited the amount of torque the drive motor could supply and increased the mass of the rotating elements, therefore decreasing the resonant frequency of the system, which ultimately limits the frequencies that can be measured. The motor in the new design is coupled to the bottom surface using a pulley/belt system, the diameters of which can be tuned to achieve a range of desired speeds. The motor in the previous design was an integrated part of the bottom surface and friction- and load sensing springs that made the system unnecessarily heavy with low system resonance frequency. The new motor is also driven by a digital motion controller which can independently specify velocity, acceleration, and displacement, as opposed to the limited-ranged and unidirectional velocity control with low torque motors in the previous design. The bottom disk is more modular in the redesigned system as well, allowing the bottom surface to be easily interchanged between experiments. The method to ensure planarity of the bottom surface has also been simplified and improved using three arms, each of which contains two opposing springs which, with the aid of a conical screw, push on each other and tilt the bottom surface in any direction (Figure 3.1B).

By utilizing this new design, the top disk mount was also altered to contain both the (vertical, normal) load- and the (lateral) friction-sensing springs because the lower rotating-disk mount no longer senses the load (Figure 1B) as in conventional SFAs. The foil-gauged friction and load springs have a force resolution of 0.1 mN and a range of 30 N. Greater sensitivity can be achieved with semiconductor strain gauges.

3.3.1 Surface Preparation

Cross-linked, molded PDMS films were adhered to silica disks in these experiments to mimic ‘soft’ (viscoelastic) biomaterial interfaces. A 1:10 ratio of cross-linker to PDMS was used (Sylgard 184 Dow Corning), and the surfaces were cured overnight in an oven at 85^{o}C. The top surface is a spherical cap with a 1 cm radius of curvature that was adhered to a 1 cm diameter flat silica disk (Figure 3.1C). The bottom (rotating) PDMS surface, which is cured onto a 40-mm sapphire disk, is 1 mm thick and 40 mm in diameter and has a 50-μm deep annular trough used to cast a thin film of each sample (Figure 3.1D).

3.3.2 Samples

Model skin creams and moisturizers were used to determine their friction (or lubrication) behavior. Three non-Newtonian shear thinning fluids (based on rheological behavior) were chosen for study. Each fluid is an emulsion with a polymeric thickener and crystallized fatty alcohols. Table 3.1 displays some qualitative properties among the fluids. Sample 1 contains both wax and fatty alcohols. Sample 2 is a polymer dispersion with no fatty alcohols. Sample 3 has a higher level of waxes and fatty-alcohols compared to the other fluids.

Table 3.1 Fluid Characterization

Fluid	**Velocity dependence during friction exp.**	**Characteristic features**
Sample 1	Typical viscous fluid	Wax and fatty-alcohol
Sample 2	Stick-slip exhibiting fluid	Wax but no fatty-alcohol
Sample 3	Mixed effect fluid	Higher concentration of wax and fatty-alcohols

3.3.3 Friction Measurements

The rotating disk was used to perform oscillating shear experiments with a peak-to-peak angle, $\theta = 90^{o}$. Prior to each measurement, the as-cast films of each sample were conditioned by performing three 'sweep-out' oscillations with a sweep-out angle of $\theta_{s\text{-}o} = 180°$ to remove excess material from the contact area and prevent buildup. The overall motion path is illustrated in Figure 3.1E. The sweep-out regime is labeled in each sample's friction trace in Figure 3.2. For each film, the applied load started at 20 mN and stepwise increased to 320 mN (corresponding to pressures of 2 to 60 kPa), and the velocity was stepwise increased from 1 to 40 mm/s at each applied load. These ranges of loads and velocities are relevant for applications such as determining sensory perception or 'feel' on human skin. The top panel of Figure 3.2 also illustrates how the 'average kinetic friction', F_{avg}, plotted in Figure 3.5 was calculated. Data was collected at 20 μs intervals to ensure that high maximum frequencies were measurable (as high as 12.5 kHz); however, no resonance or stick-slip features were observed above ~1 kHz. Therefore, the number of data points were decreased by a factor of ten to reduce wavelet transform computational time.

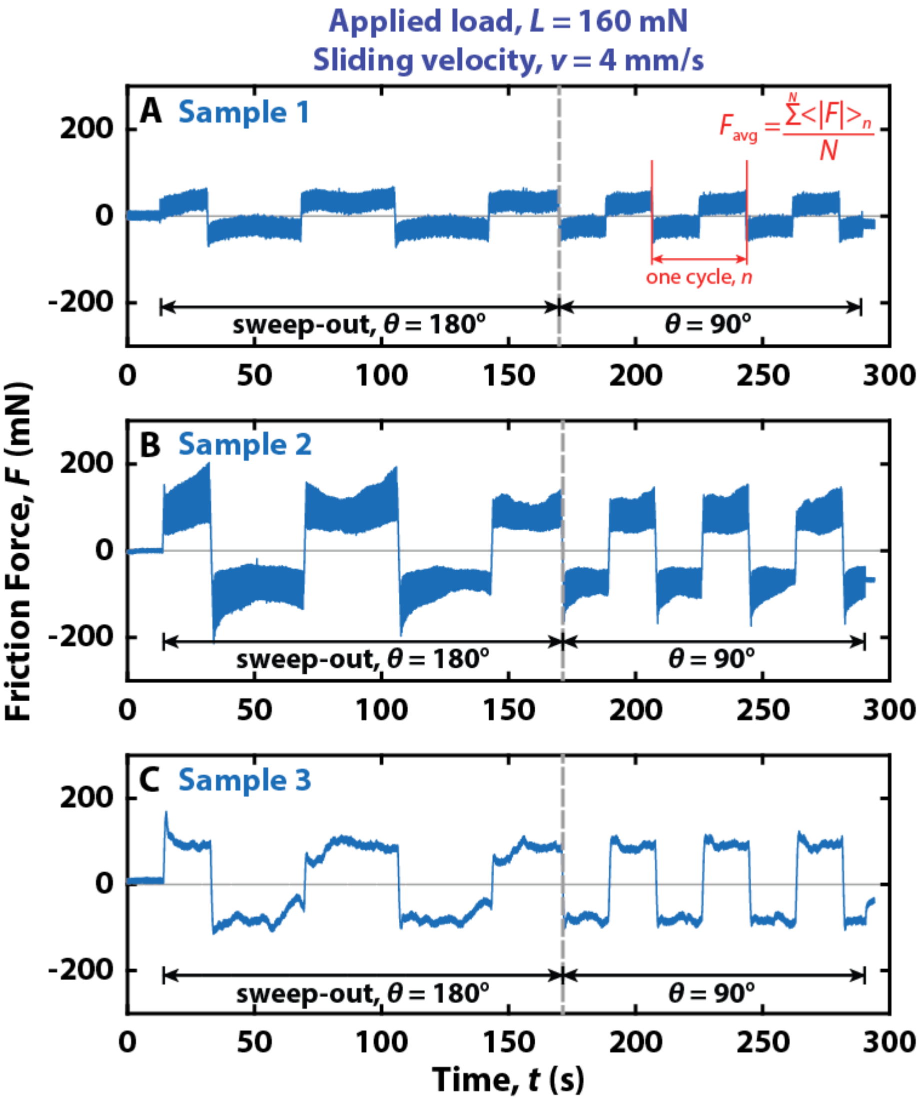

Figure 3.2 Representative friction traces for all three samples at L = 160 mN and v = 4 mm/s. Large angle sweeps (180°, 2 full oscillations) of deposited films were conducted to normalize the sample thicknesses and previous histories and are indicated to the left of the vertical gray dashed lines. The analyzed portions of the friction traces occur to the right of the vertical gray dashed lines (smaller oscillations of 90°) and when averaged over multiple runs give rise to the points in Figure 3.5 (see Results and Discussion). The corresponding sweeping path is illustrated in depth in Figure 3.1E.

3.3.4 Wavelet Analysis

To expand friction analysis beyond typical friction coefficient measurements, a continuous Morse wavelet transform[24,25] was applied to each friction trace to unambiguously extract the time-dependent frequency components of the friction traces, allowing for detailed interpretation of dynamic, intermittent, or transient effects, even in ‘noisy’ data.

Briefly, a continuous wavelet transform is a convolution of an input signal (in this case a time series) with a set of scaled wavelet functions generated by a ‘mother wavelet’, typically using a fast Fourier transform algorithm. The mother wavelet is a packet of wave-like oscillations whose amplitude is maximal in the center of the wavelet and quickly approaches zero as $t \rightarrow \pm\infty$ (a Morse wavelet is shown in Figure 3.3). The mother wavelet can then be stretched or compressed (scaled) in time with respect to a complete orthonormal set of basis functions, creating a wavelet series whose individual functions have varying duration but consistent shape (and therefore varying frequency). An input signal is then piece-wise convoluted with each of the series’ functions to determine the similarity, or ‘coherence’, of the signal with the given wavelet, thus extracting which frequencies are most coherent with the input signal at a given time. In contrast to the short-time Fourier transform algorithm, which obeys the time-frequency uncertainty principle, $\Delta t\Delta\omega \geq \frac{1}{2}$, the scaling feature of the wavelet algorithm allows for both excellent time and frequency localization when determining the time-varying frequency components of an input signal. To calculate the wavelet transforms of friction traces in this work, the MATLAB (MathWorks, version 9.3 2017b) continuous wavelet transform function ‘cwt’ was used.

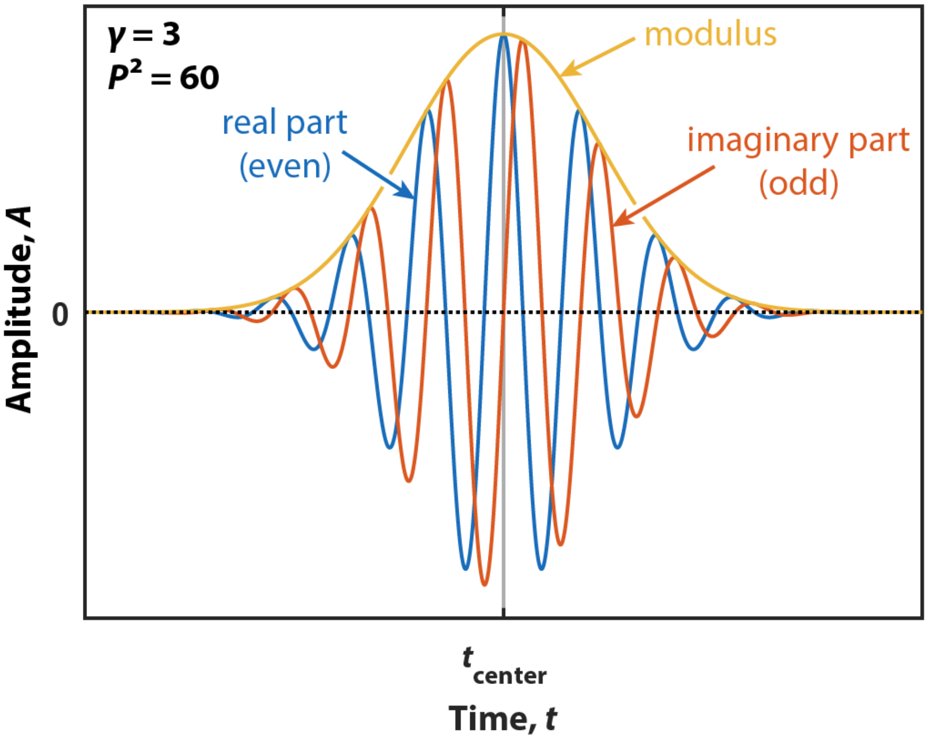

Figure 3.3 The Morse wavelet contains two parameters: γ to characterize the symmetry, and P^2 which is proportional to the wavelet duration in time. Higher γ and P^2 lead to desired symmetry in the frequency-domain. Analytic wavelets like the Morse wavelet are complex-valued and thus contain real and imaginary components.

To illustrate the information revealed from performing a wavelet transform on time-series data, several differently-shaped model waveforms with two constituent frequencies (f_1 = 1 Hz, f_2 = 5 Hz), and their corresponding wavelet transforms are shown in Figure 3.4. The amplitude of a given frequency contained in the time-series at a given time is plotted to provide a rich, detailed representation of the frequencies present.

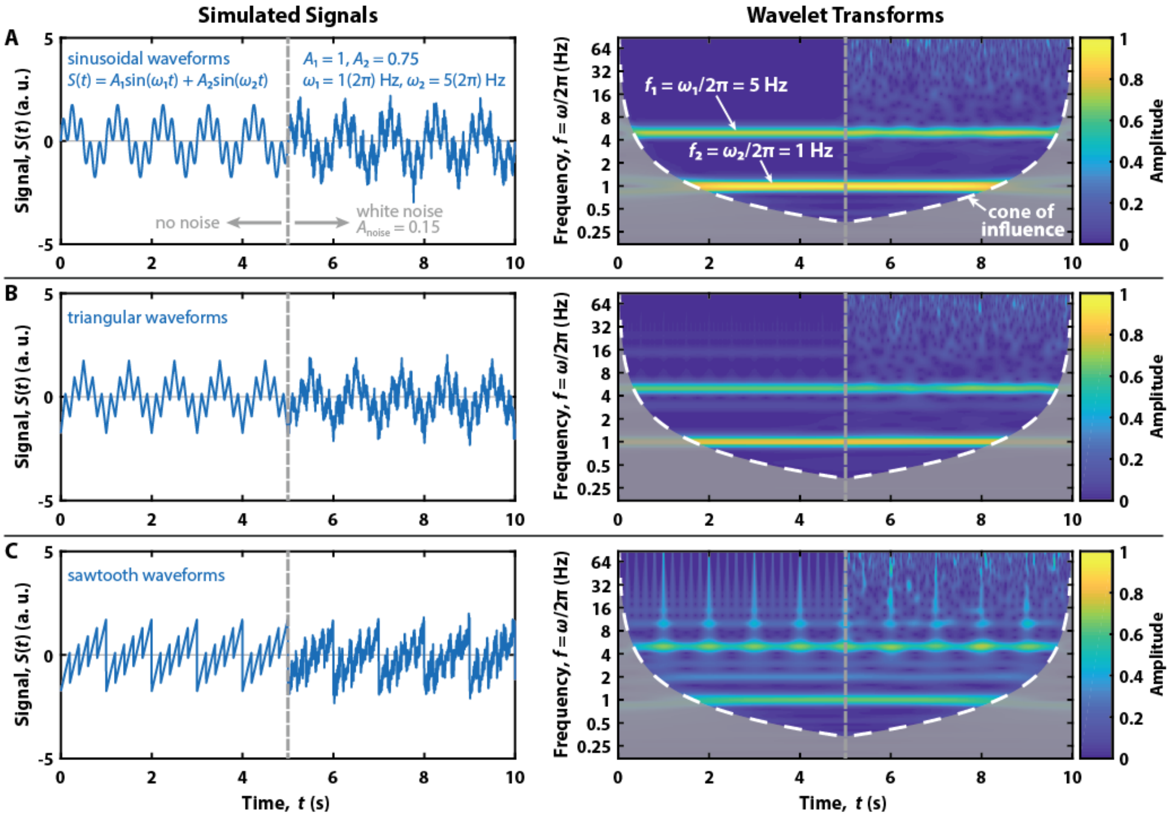

Figure 3.4 Wavelet analysis of three different model signals. Simulated composite signals of frequencies f_1 = 1 Hz and f_2 = 5 Hz and amplitudes A_1 = 1 and A_2 = 0.75 have been generated for **A**. sine, **B**. triangle, and **C**. saw-tooth waveforms (left panels). At time t = 5 s, white noise with amplitude A_{noise} = 0.15 is introduced. The right panels illustrate the wavelet transforms of the time series on the left. **A**. The sine wave results in a large amplitude band at 1 Hz and 5 Hz in the wavelet transform. **B**. The triangle wave results in weaker amplitude bands compared to the pure sine wave with the emergence of vertical spikes and overtones due to the sharp discontinuities in the time series. **C**. The saw-tooth wave (resembling stick-slip) results in still lower intensity bands and demonstrates more intense vertical spikes and overtones. For all model signals, introduction of white noise does not fully degrade the features in the wavelet transforms.

Different waveform shapes have specific characteristic features in the wavelet transform, which are robust against noise. Most notably, as the characteristic waveform becomes more asymmetrical and ‘sawtooth-like’ (like stick-slip friction), more overtones and vertical frequency ‘spikes’ are observed in the wavelet transform. Therefore, wavelet transforms of friction traces should not only be able to quickly characterize the frequencies of dynamic friction features, but also qualitatively determine if such frequencies are resonant frequencies of the system (sinusoidal, device specific) or stick-slip oscillations due to surface interactions (saw-tooth, surface and lubricant specific).

3.4 Results and Discussion

3.4.1 Friction vs. velocity at varying loads

Lubricating systems typically have velocity dependent friction forces. Over many orders of magnitude in velocity, it is not uncommon for the system to exhibit multiple increases and decreases (highs and lows) in the friction force traces (see Figure 3.5A for a schematic example). These increases and decreases in friction forces can usually be attributed to certain time- and length-scales characteristic to the molecular structure of the lubricant, surface features, and lubricant-surface interactions which can be interpreted by the Deborah number[26]. The Deborah Number, which is the relationship between the system's relaxation time(s) and the time over which an interaction occurs (is measured), can similarly be represented as the relationship between the velocity of a system and the characteristic velocity or velocities, defined as the characteristic distance(s) divided by their relaxation time(s)[27]. In complex systems, there can be multiple relaxation times and length scales, giving rise to multiple peaks and valleys in the friction force over many orders of magnitude of velocity. Experimental studies on three samples that span different aspects of these phenomena are further discussed, as well as their relation to dynamic friction effects such as stick-slip and oscillatory responses.

Sample 1: Typical viscous fluid

The first lubricant studied behaves as a typical viscous fluid in the velocity regime from 1 mm/s to 40 mm/s. As seen in Figure 3.5B, this fluid exhibits a gradual increase in the friction force with increasing shear velocity, indicating that in this load and velocity regime, the viscosity of the fluid dominates the friction behavior as in hydrodynamic lubrication[28] and is typically seen in shear experiments at higher velocities (refer to high velocity regime in Figure 3.5A schematic). With increasing velocity, there is more resistance to shear due to the viscosity of the fluid, and thus the friction (strictly, lubrication) force increases. This type of lubrication force can be described by Couette flow, $F_{\|} = \eta A V_{\|}/D$, for two parallel plates of area A at separation D moving at relative velocity $V_{\|}$, where η is the bulk viscosity of the lubricating fluid. The friction vs. load curves, shown in Figure 3.6A, are linear and extrapolate through the origin (0,0), indicating there is no adhesion contribution to the friction force which is therefore strictly load and velocity dependent.

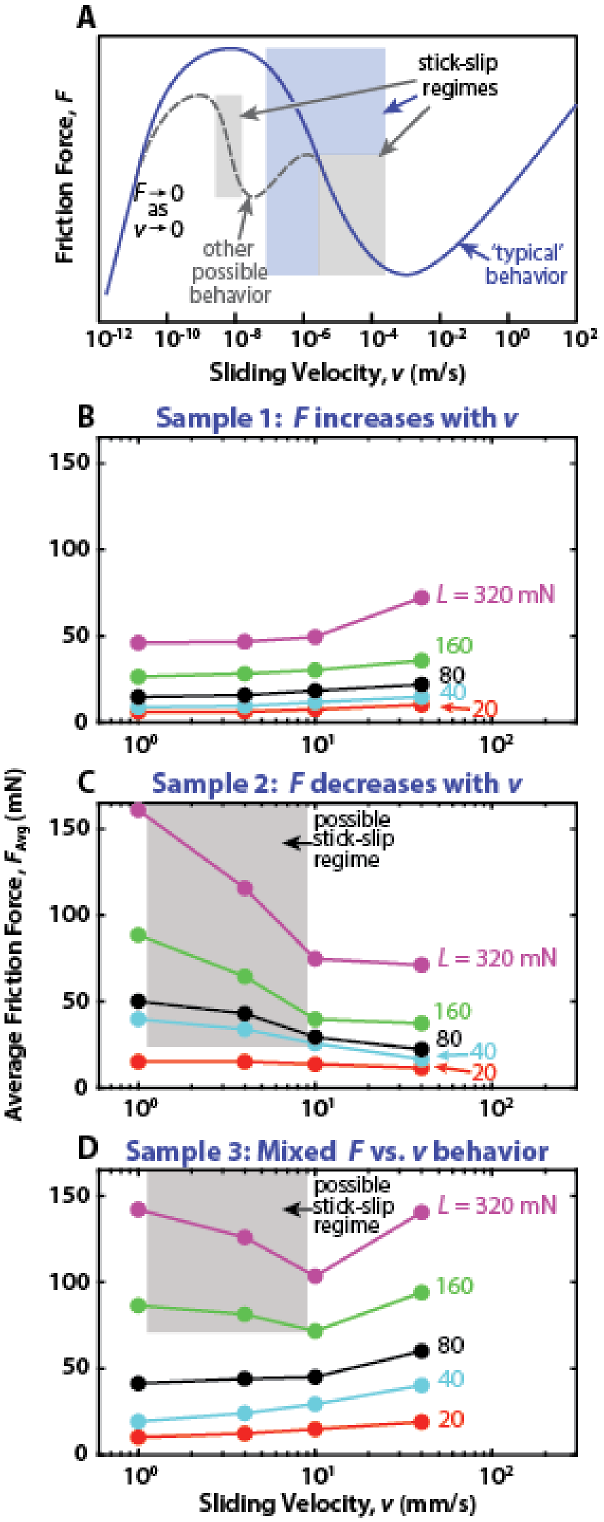

Figure 3.5 Average friction force vs. sliding velocity (F_{avg} vs. v) at various loads, L, for three different samples. **A**. Sample 1 exhibits increasing F_{avg} with v for all L. **B**. Sample 2 exhibits decreasing F_{avg} with v for all L. **C**. Sample 3 exhibits a mix of increasing and decreasing F_{avg} with v for different L. The extent of stick-slip depends on the stiffness of the sensing mechanism.

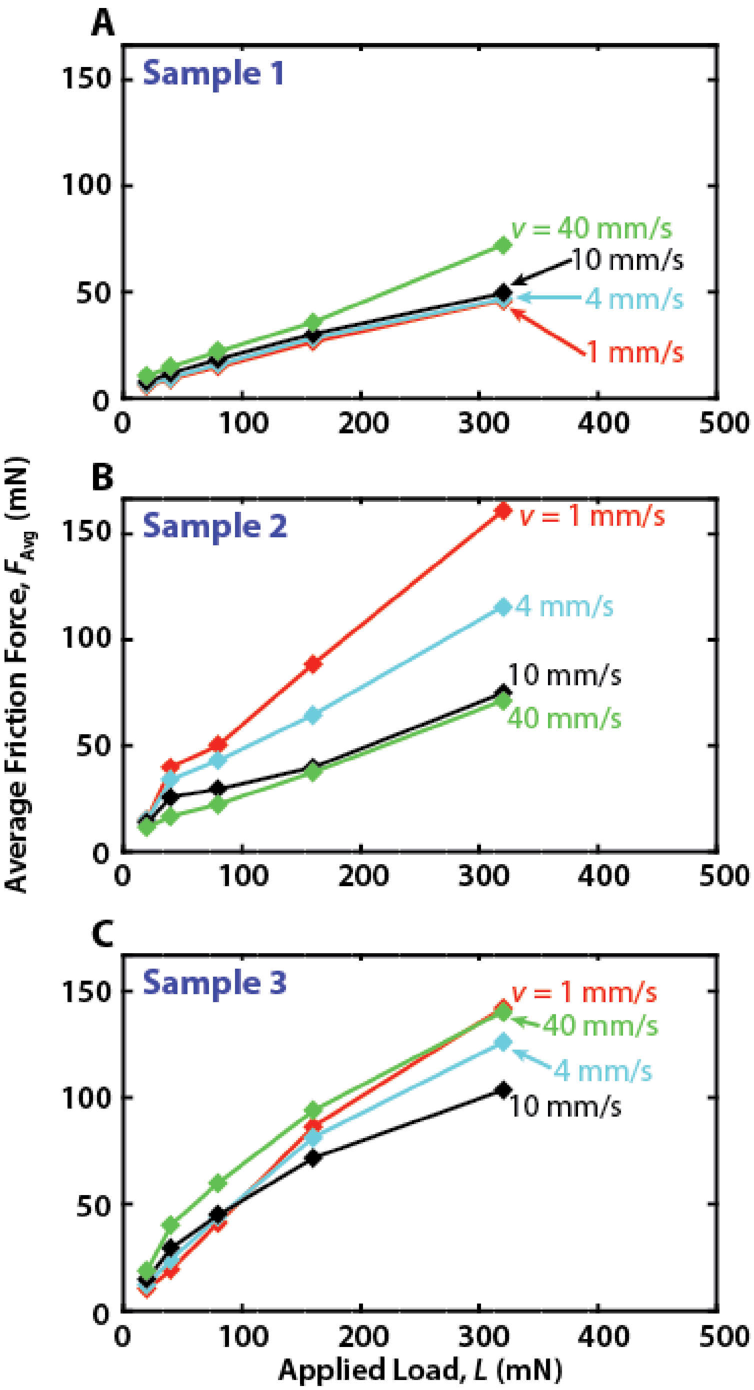

Figure 3.6 Average friction force vs. applied load (F_{avg} vs. L) at various velocities. The same data is represented as in Figure 3.5 but has a function of applied load to give a sense of the friction coefficient for various loads and velocities tested. Sample 1 (**A**), has a linear response with load and deviates slightly with velocity. Samples 2 and 3 (**B** and **C**) are both non-linear, and appear as if they would extrapolate to having a finite friction force at 0 load, indicating an adhesive contribution to the friction force.

Sample 2: Stick-slip exhibiting fluid

Sample 2 (Figure 3.5C, 3.6B) exhibits the opposite velocity trend of Sample 1. The friction force decreases with increasing velocity in the same velocity and load regime as Sample 1, with a sharp decrease at higher loads (160-320 mN, Figure 3.5C). However, between 10 and 40 mm/s the friction force remains relatively constant. The steep decrease in friction force with sliding velocity may indicate a region where stick-slip friction is expected[29–31] and is analyzed further with wavelet transforms. Figure 3.7 shows plots of the friction traces for Sample 2 as a function of load and velocity where the breadth in F of a given uni-directional sliding event indicates larger oscillations in the friction force. The friction vs. load curves are not completely linear, as displayed in Figure 3.6B. If a line were extrapolated through the vertical axis, there would be positive friction at zero applied load, indicating an adhesive contribution to the friction force, which may explain why the friction force is higher at lower velocities. The surfaces may be moving slower than the characteristic time and length scale of the adhesive bonds between the fluid and surfaces, giving rise to higher friction forces at lower velocities. As the load is decreased, the steepness of the velocity behavior goes away. When considering the typical behavior curve (Figure 3.5A) and a Deborah number interpretation, the hump in the friction curve is expected to shift down and left as the load is decreased, just as it is observed.

Sample 3: Mixed behavior fluid

Sample 3 exhibits two different regimes of friction behavior at different loads (Figure 3.5D, 4C). At low loads, the friction force increases with increasing velocity (similar to Sample 1), yet at higher loads (160-320 mN) there is an initial decrease in friction force from 1-10 mm/s and then an increase. Structural changes of the fluid components upon higher compression may lead to the differing velocity and load dependence, thus affecting the force required to shear and time allowed for molecular rearrangements and alignment[32]. Other time-associated effects due to repeated shear at the same contact could also explain the variable trends with load[33]. This fluid shows an example of how testing multiple loads can exhibit drastically different friction forces compared to many studies that produce a Stribeck curve for only one load. Also, a simple friction coefficient would not be effective to describe the friction behavior in this fluid since the relation between friction and load (Figure 3.6C) is non-linear. As was interpreted for Sample 2, it appears the typical velocity behavior curve is shifted down and to the left as the load is decreased during shearing, and thus exhibits the hydrodynamic type (or more liquid-like) behavior at lower velocities, compared to shearing at higher loads.

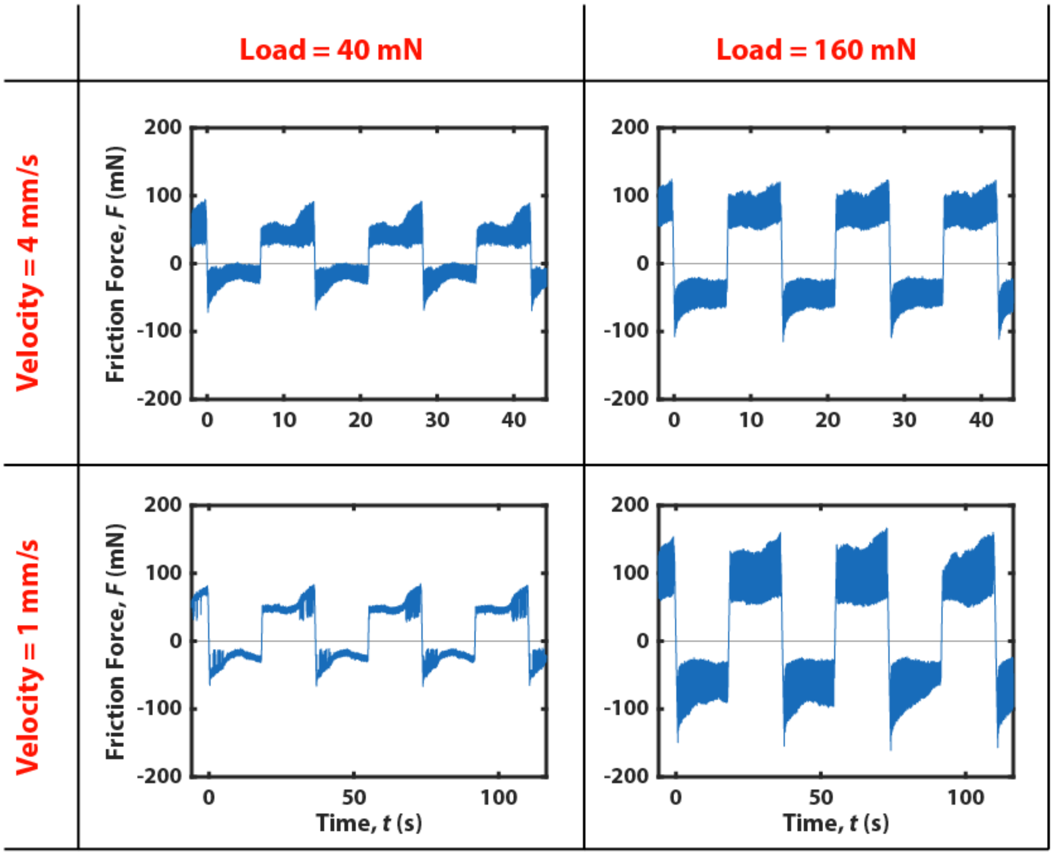

Figure 3.7 Friction traces as a function of load and velocity for Sample 2. The breadth of the friction signal at higher loads and velocities is indicative of resonant or stick-slip response.

3.4.2 Wavelet interpretation and implications

The friction traces for Sample 2 and their wavelet transforms are presented in Figure 3.8. Sample 2 was selected for wavelet analysis due to the richness of stick-slip, oscillatory, and smooth sliding behavior exhibited at different loads and velocities. The steep negative trends in the F_{avg} vs. v (for all L) which, along with the stiffness of the system, is a likely indicator of stick-slip sliding. Figure 3.8A shows that at low load and velocity (L = 20 mN, v = 4 mm/s), the only frequency component present in the friction trace is a pure sinusoidal oscillation at 120 Hz, indicative of mechanical resonance in the system. The horizontal band in the wavelet transform is steady and displays no significant overtones. Considering the F_{avg} vs. v plot of Sample 2 in Figure 3.5C, the lack of stick-slip friction at this load and velocity is not surprising because the friction is nearly constant with increasing velocity at this load. Increasing the load to L = 80 mN at v = 4 mm/s, a combination of load and velocity which lies within a negative slope in Figure 3.5C causes the system to exhibit both mechanical resonance (160 Hz) and stick-slip sliding (26 Hz) responses (Figure 3.8B). The strong horizontal band in the wavelet transform is the fundamental stick-slip frequency which causes overtones at each slip event. The overtones cannot be sustained above the 160 Hz mechanical frequency. Finally, increasing the load to L = 160 mN at v = 1 mm/s damps out most of the mechanical resonance in the system and results in a high amplitude stick-slip friction response with a fundamental frequency of approximately 5 Hz (Figure 3.8C). Overtones are clearly visible in the wavelet transform as weaker horizontal bands at higher frequencies, and the vertical spikes associated with slip events are not quenched by a resonant frequency in the system.

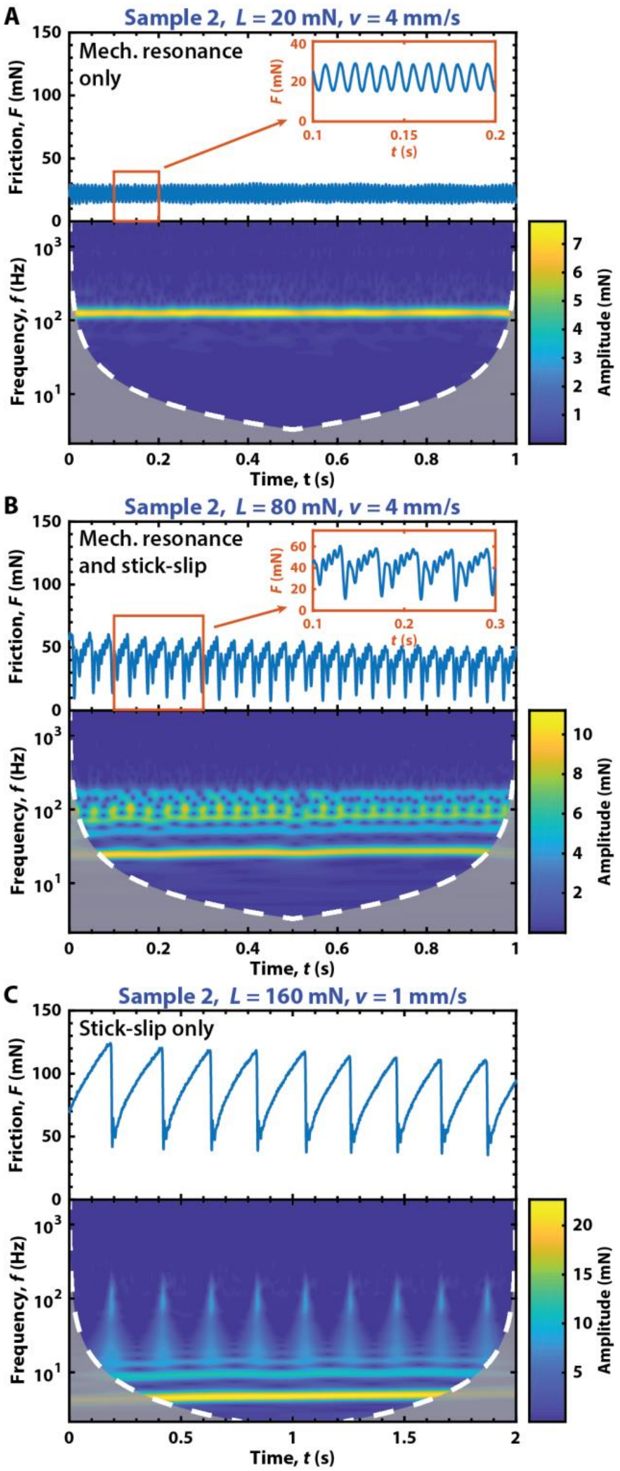

Figure 3.8 Representative friction traces for Sample 2 and the corresponding wavelet transforms displaying different frequency components at varied loads and velocities. **A**. (L = 20 mN, v = 4 mm/s) Pure mechanical resonance is observed at 125 Hz with no observable stick-slip. **B**. (L = 80 mN, v = 4 mm/s) Mechanical resonance of approximately 160 Hz is imposed on a saw-tooth (stick-slip) signal at 26 Hz. **C**. (L = 160 mN, v = 1 mm/s) A stick slip signal at approximately 5 Hz is clearly characterized by a horizontal band and prominent vertical spikes and overtones.

A summary of the stick-slip response at different loads and velocities for Sample 2 is presented in Figure 3.9, showing both the fundamental stick-slip frequencies (Figure 3.9A), and the stick-slip amplitudes (Figure 3.9B). This summarizing stick-slip ‘phase diagram’ can be easily generated for any materials system by algorithmically interpreting the wavelet transforms of friction traces at various loads and velocities. Because stick-slip friction can cause damage and wear in lubricated and non-lubricated systems, this type of rapid analysis may prove to be important for quickly evaluating the efficacy of lubricants at varying sliding parameters.

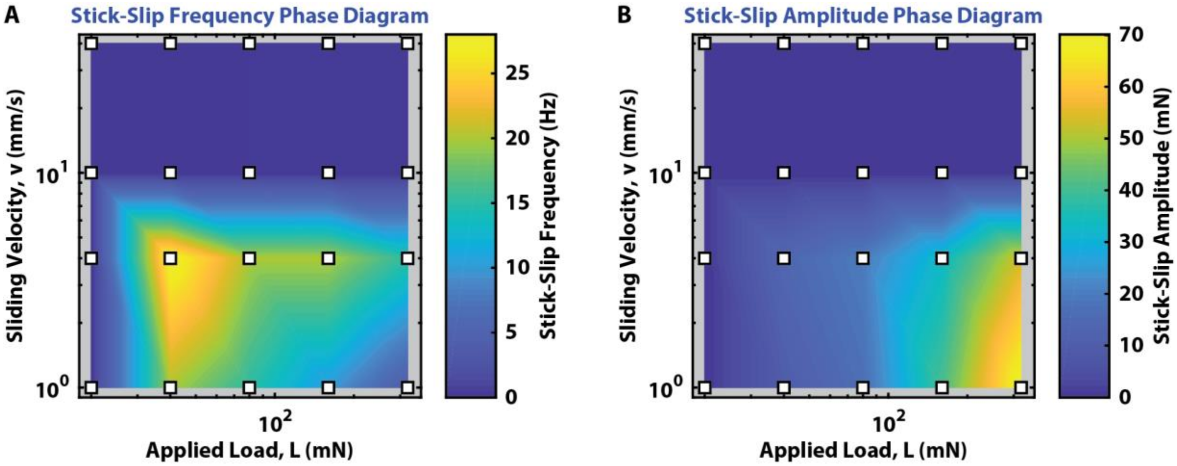

Figure 3.9 Applied load vs. sliding velocity (*L* vs. *v*) phase diagrams for **A**. stick-slip frequency response and **B**. stick-slip amplitude for experiments on Sample 2. White squares indicate the combinations of applied load and velocity measured to generate each phase diagram. Colored shading is generated by linearly interpolating between measured values.

3.5 Conclusions

Friction can exhibit complex behavior when examining different parameters such as load and velocity, especially when considering transient or dynamic effects. We have designed and created a rotating disk (ball on disk tribometer) attachment for the SFA that allows for friction to be measured at velocities ranging from mm/s to m/s with applied loads from 0.1 mN to tens of newtons (corresponding to contact pressures of kilopascals to megapascals).

Friction forces from 0.1 mN to tens of newtons can be measured with 0.1 mN sensitivity. Wavelet transforms were used to extract the rich, dynamic frequency response contained within the friction traces. The wavelet transform method for analyzing friction data allows for mechanical resonances to be rapidly and unambiguously differentiated from stick-slip sliding and can also measure other high-frequency transient effects. The rotating disk combined with wavelet analysis can be used for other applications involving high speed friction, including damage and wear evaluation and sensory perception studies.

References

(1) Luengo, G.; Tsuchiya, M.; Heuberger, M.; Israelachvili, J. Thin Film Rheology and Tribology of Chocolate. *J. Food Sci.* **1997**, *62* (4), 767–812.

(2) Kragelʹskiĭ, I. V.; Dobychin, M. N.; Kombalov, V. S. *Friction and Wear: Calculation Methods*; Pergamon Press, 1982.

(3) Sivamani, R. K.; Goodman, J.; Gitis, N. V.; Maibach, H. I. Friction Coefficient of Skin in Real-Time. *Ski. Res. Technol.* **2003**, *9* (3), 235–239.

(4) Nacht, S.; Close, J.-A.; Yeung, D.; Gans, E. Skin Friction Coefficient: Changes Induced by Skin Hydration and Emollient Application and Correlation with Perceived Skin Feel. *J. Soc. Cosmet. Chem.* **1981**, *32* (2), 55–65.

(5) Braun, O.; Peyrard, M. Dependence of Kinetic Friction on Velocity: Master Equation Approach. *Phys. Rev. E* **2011**, *83*.

(6) Ben-David, O.; Fineberg, J. Static Friction Coefficient Is Not a Material Constant. *Phys. Rev. Lett.* **2011**, *106* (25), 254301.

(7) Blau, P. The Significance and Use of the Friction Coefficient. *Tribol. Int.* **2001**, *34* (9), 585–591.

(8) Masjuki, H.; Maleque, M. Investigation of the Anti-Wear Characteristics of Palm Oil Methyl Ester Using a Four-Ball Tribometer Test. *Wear* **1997**, *206* (1–2), 179–186.

(9) Gallardo-Hernandez, E.; Lewis, R. Twin Disc Assessment of Wheel/rail Adhesion. *Wear* **2008**, *265* (9–10), 1309–1316.

(10) Burris, D. L.; Sawyer, W. G. Addressing Practical Challenges of Low Friction Coefficient Measurements. *Tribol. Lett.* **2009**, *35* (1), 17–23.

(11) Godfrey, D. Friction Oscillations with a Pin-on-Disc Tribometer. *Tribol. Int.* **1995**, *28*

(2), 119–126.

(12) Ogletree, D. F.; Carpick, R. W.; Salmeron, M. Calibration of Frictional Forces in Atomic Force Microscopy. *Rev. Sci. Instrum.* **1996**, *67*, 3298.

(13) Feeny, B.; Guran, A.; Hinrichs, N.; Popp, K. A Historical Review on Dry Friction and Stick-Slip Phenomena. *Appl. Mech. Rev.* **1998**, *51* (5), 321.

(14) Howe, R. D.; Cutkosky, M. R. Sensing Skin Acceleration for Slip and Texture Perception. In *Proceedings, 1989 International Conference on Robotics and Automation*; IEEE Comput. Soc. Press; pp 145–150.

(15) Sanahuja, S.; Upadhyay, R.; Briesen, H.; Chen, J. Spectral Analysis of the Stick-Slip Phenomenon in “oral” Tribological Texture Evaluation. *J. Texture Stud.* **2017**, *48* (4), 318–334.

(16) Giasson, S.; Israelachvili, J.; Yoshizawa, H. Thin Film Morphology and Tribology Study of Mayonnaise. *J. Food Sci.* **1997**, *62* (4), 640–652.

(17) Ibrahim, R. A. Friction-Induced Vibration, Chatter, Squeal, and Chaos—Part II: Dynamics and Modeling. *Appl. Mech. Rev.* **1994**, *47* (7), 227.

(18) Tas, N.; Sonnenberg, T.; Jansen, H.; Legtenberg, R.; Elwenspoek, M. Stiction in Surface Micromachining. *J. Micromech. Microeng* **1996**, *6*, 385–397.

(19) Lee, D. W.; Banquy, X.; Israelachvili, J. N. Stick-Slip Friction and Wear of Articular Joints. *Proc. Natl. Acad. Sci. U. S. A.* **2013**, *110* (7), E567-74.

(20) Daubechies, I. The Wavelet Transform, Time-Frequency Localization and Signal Analysis. *IEEE Trans. Inf. Theory* **1990**, *36* (5), 961–1005.

(21) Grossmann, A.; Kronland-Martinet, R.; Morlet, J. Reading and Understanding Continuous Wavelet Transforms; Springer, Berlin, Heidelberg, 1990; pp 2–20.

(22) Liang, J. W.; Feeny, B. F. Wavelet Analysis of Stick-Slip in an Oscillator with Dry Friction. In *ASME Design Engineering Technical Conferences*; 1995.

(23) Lowrey, D. D.; Tasaka, K.; Kindt, J. H.; Banquy, X.; Belman, N.; Min, Y.; Pesika, N. S.; Mordukhovich, G.; Israelachvili, J. N. High-Speed Friction Measurements Using a Modified Surface Forces Apparatus. *Tribol. Lett.* **2011**, *42* (1), 117–127.

(24) Olhede, S. C.; Walden, A. T. Generalized Morse Wavelets. *IEEE Trans. Signal Process.* **2002**, *50* (11), 2661–2670.

(25) Daubechies, I.; Paul, T. Time-Frequency Localisation Operators-a Geometric Phase Space Approach: II. The Use of Dilations. *Inverse Probl.* **1988**, *4* (3), 661–680.

(26) Reiner, M. The Deborah Number. *Phys. Today* **1964**, *17* (1), 62–62.

(27) Israelachvili, J. N. *Intermolecular and Surface Forces: Revised Third Edition*; Academic Press, 2011.

(28) Bowden, F. P.; Tabor, D. *The Friction and Lubrication of Solids*; Clarendon Press, 2001.

(29) Berman, A. D.; Ducker, W. A.; Israelachvili, J. N. Origin and Characterization of Different Stick−Slip Friction Mechanisms. *Langmuir* **1996**, *12* (19), 4559–4563.

(30) Yoshizawa, H.; Israelachvili, J. Fundamental Mechanisms of Interfacial Friction. 2. Stick-Slip Friction of Spherical and Chain Molecules. *J. Phys. Chem.* **1993**, *97* (43), 11300–11313.

(31) Brockley, C. A.; Ko, P. L. Quasi-Harmonic Friction-Induced Vibration. *J. Lubr. Technol.* **1970**, *92* (4), 550.

(32) Luengo, G.; Israelachvili, J.; Granick, S. Generalized Effects in Confined Fluids: New Friction Map for Boundary Lubrication. *Wear* **1996**, *200* (1–2), 328–335.

(33) Börzsönyi, T.; Szabó, B.; Törös, G.; Wegner, S.; Török, J.; Somfai, E.; Bien, T.; Stannarius, R. Orientational Order and Alignment of Elongated Particles Induced by Shear. *Phys. Rev. Lett.* **2012**, *108* (22), 228302.

Chapter 4: Simultaneous Fluorescence Imaging and Force-Distance Measurement Using the Fluorescence Surface Forces Apparatus

4.1 Real time intermembrane force measurements and imaging of lipid domain morphology during hemifusion

Reprinted with permission from Dong Woog Lee, Kai Kristiansen, Stephen H. Donaldson Jr., Nicholas Cadirov, Xavier Banquy, Jacob N. Israelachvili, *Nature Communications* 2015, 6:7238. Copyright©2015 Nature Publishing Group

4.1.1 Abstract

Membrane fusion is the core process in membrane trafficking, and is essential for cellular transport of proteins and other biomacromolecules. During protein-mediated membrane fusion, membrane proteins are often excluded from the membrane-membrane contact, indicating that local structural transformations in lipid domains play a major role. However, the rearrangements of lipid domains during fusion have not been thoroughly examined. Here, using a newly developed Fluorescence Surface Forces Apparatus (FL-SFA), migration of liquid disordered clusters and depletion of liquid ordered domains at the membrane-membrane contact are imaged in real time during hemifusion of model lipid membranes, together with simultaneous force-distance and lipid membrane thickness measurements. The load and contact time dependent hemifusion results show that the domain rearrangements decrease the energy barrier to fusion, illustrating the significance of dynamic domain transformations in membrane fusion processes. Importantly, the FL-SFA can

unambiguously correlate interaction forces and *in situ* imaging in many dynamic interfacial systems.

4.1.2 Introduction

Lipid domains are clusters or two-dimensional aggregates of lipids whose molecular composition differs from the surrounding membrane[1]. One commonly observed lipid domain, the sphingolipid and cholesterol enriched domain, plays important roles in many biological membrane fusion processes. Lipid domains are associated with protein binding sites during exo- and endo-cytosis[2,3], which are essential for transport of protein and vesicle cargo[4,5]. Also, ion channels for electrical signal transduction are localized in lipid domains[6,7]. In extracellular processes, lipid domains are known to act as viral gateways or pathogen binding sites in diseases such as Alzheimer's, bovine spongiform encephalopathy (BSE, also known as 'mad cow disease'), and human immunodeficiency virus 1 (HIV-1)[8].

Previous studies on combined lipid and protein systems show that lipid domains localize SNARE proteins[2,3,9], and the formation of lipid domain/SNARE complexes is essential for lowering the energy barrier to fusion[10]. Other studies on myogenic cells show that lipid domains dynamically cluster and disperse during different stages of fusion, contributing to cell adhesion and plasma membrane union[11]. Furthermore, during fusion, the membrane proteins are eventually excluded from the membrane-membrane contact zone[12], at which point protein-free intermembrane interactions become significant as also in non-biological, surfactant membrane fusion processes[13]. Such interactions include van der Waals, steric hydration, electrostatic, and hydrophobic interactions that eventually drive the membranes to fuse[13,14]. The structural intermediates formed during the fusion process, known as fusion "stalks," have been reported to depend delicately on lipid membrane composition[15].

Although the involvement of lipid domains during biological fusion processes is now well-established, their dynamic rearrangements during fusion have yet to be elucidated.

Such domains are seen in reconstituted myelin lipid bilayers extracted from the brain, for example, where the domains are observed to be different in healthy vs. pathological (e.g., multiple sclerosis) membranes[16]. In this case, as in many other cellular structures, the membranes are planar and closely stacked *in vivo* and therefore strongly interacting with each other across the water spaces. While these domains have not been observed *in vivo*, many experiments have shown correlations between the *in vitro* structures observed in healthy and diseased membranes[16,17]. Indeed, many studies of domains focus on model or supported membrane systems to draw (perhaps indirect) correlations to the *in vivo* systems. Experiments on model systems, while inherently non-biological, can be used to find correlations and insights of fundamental importance.

Therefore, in this work we aim to determine and correlate the membrane morphology, interactions, domain structures, and the time dependence of rearrangements within the domains during contact, compression, adhesion, and fusion of two model membranes. Using a custom-built Fluorescence Surface Forces Apparatus (FL-SFA, see methods section and Fig. 4.1 for a detailed description of the setup), we measured the interaction forces between supported lipid membranes and simultaneously imaged lipid domains during pressure-induced and protein-free hemi-fusion, allowing for real-time correlations to be made between the interaction forces, membrane thickness, and spatial and temporal domain rearrangements. The results on the model membranes provide mechanistic details of domain rearrangements during membrane fusion, demonstrating that the FL-SFA should find wide utility in correlating fluorescent images with interaction forces during compression and separation of a broad range of materials between confined surfaces.

4.1.3 Methods

4.1.3.1 Materials

Lipids used in this study were purchased from Avanti Polar lipids (Alabaster, AL): 1,2-dipalmitoyl-*sn*-glycero-3-phosphoethanolamine (DPPE, 16:0, Powder), 1,2-dioleoyl-*sn*-glycero-3-phosphocholine (DOPC, 18:1, Chloroform), Brain sphingomyeiln (BSM, predominant 18:0, Porcine, Chloroform), and cholesterol (CHOL, ovine wool, ≥98%). For the fluorescence imaging, Texas Red® 1,2-Dihexadecanoyl-sn-Glycero-3-Phosphoethanolamine, Triethylammonium Salt (TR-DHPE) was purchased from Invitrogen (Carlsbad, CA). DPPE was dissolved in a solvent which is a 3:1 (vol/vol) mixture of chloroform (Sigma Aldrich, CHROMASOLV Plus for HPLC, purity≥99.9%) and methanol (Sigma Aldrich, CHROMASOLV Plus for HPLC, purity≥99.9%) at a final concentration of 1 mg ml^{-1}. DOPC, BSM, and CHOL were mixed in a 1:1:1 (mol/mol) solution at a final concentration of 1 mg ml^{-1} in chloroform. A trace amount (1 wt%) of TR-DHPE was added to the mixture for imaging purposes. All lipids were stored in a deep freezer (–50°C) until use. Buffer salts were purchased from Sigma Aldrich (St. Louis, MO), mixed and dissolved in Milli-Q water (Millipore, Billerica, MA) at final concentrations of 100 mM Sodium nitrate (ReagentPlus, purity≥99.0%), 10 mM Tris(hydroxymethyl)aminomethane (ACS reagent, purity≥99.8%), and 2 mM Calcium nitrate tetrahydrate (purity≥99.0%) at a pH of 7.5.

4.1.3.2 Fluorescence SFA (FL SFA)

A standard SFA2000 system (SurForce LLC, Santa Barbara)[18] was modified in order to enable simultaneous fluorescence imaging with the force-distance profiling. The two most critical modifications were (i) replacing the reflective layer of silver with a hard quarter wave plate coating to allow for wavelength dependent specific reflective and transmission regions (see Fig. 4.1 and 4.2), and (ii) modify the optical paths to allow for the necessary filters and mirrors for fluorescence imaging.

Figure 4.1 shows the surface forces apparatus with fluorescence attachment (FL-SFA) setup where the fluorescence light is illuminated from above and the white light for force-distance profiling is from below. A longpass filter of 575 nm in front of the white light source minimizes its interference with the fluorescence imaging. The remainder of the white light is passed through the mica surfaces with the quarter wave plate coating (see Fig. 4.1 and 4.2A). Emerging multiple beam interfering (MBI) light from the cavity created by the reflective quarter wave plate coating at the backside of the mica surfaces is guided via a 50/50 beam splitter to a spectrometer, where MBI light is diffracted into fringes of equal chromatic order (FECO). The FECO fringes are recorded by a Princeton CoolSNAP CCD camera. The FECO fringes provide information of both absolute separation distances between the two mica surfaces and the profile of the apposing curved surfaces[18]. The lower surface is mounted to a double cantilever spring with a known spring constant *k*, which allows for accurate force measurements.

The fluorescent dye Texas Red used in this study has an absorption peak at 589 nm. A mercury lamp with a short band filter at 589 nm wavelength (10 nm wavelength width) provides the excitation light for the fluorescence imaging. A dichroic mirror at 593 nm wavelength allows for reflective mode imaging as it reflects the excitation light from the Hg-lamp and transmits the emission light from the fluorescent dye. The lipid sample with Texas Red (see preparation below) fluoresces with a peak around 615 nm. The emission light from the fluorescent dye is passed through the dichroic mirror and a short pass filter at 620 nm wavelength (10 nm wavelength width) and then recorded by a Hamamatsu Orca-R2 CCD camera.

The boundary of 580 nm wavelength of light for the quarter wave plate coating is chosen for fluorescence imaging using Texas-Red. This boundary can easily be shifted to allow for other types of fluorophores. The numerical aperture of the objective lens is 0.27 for our setup.

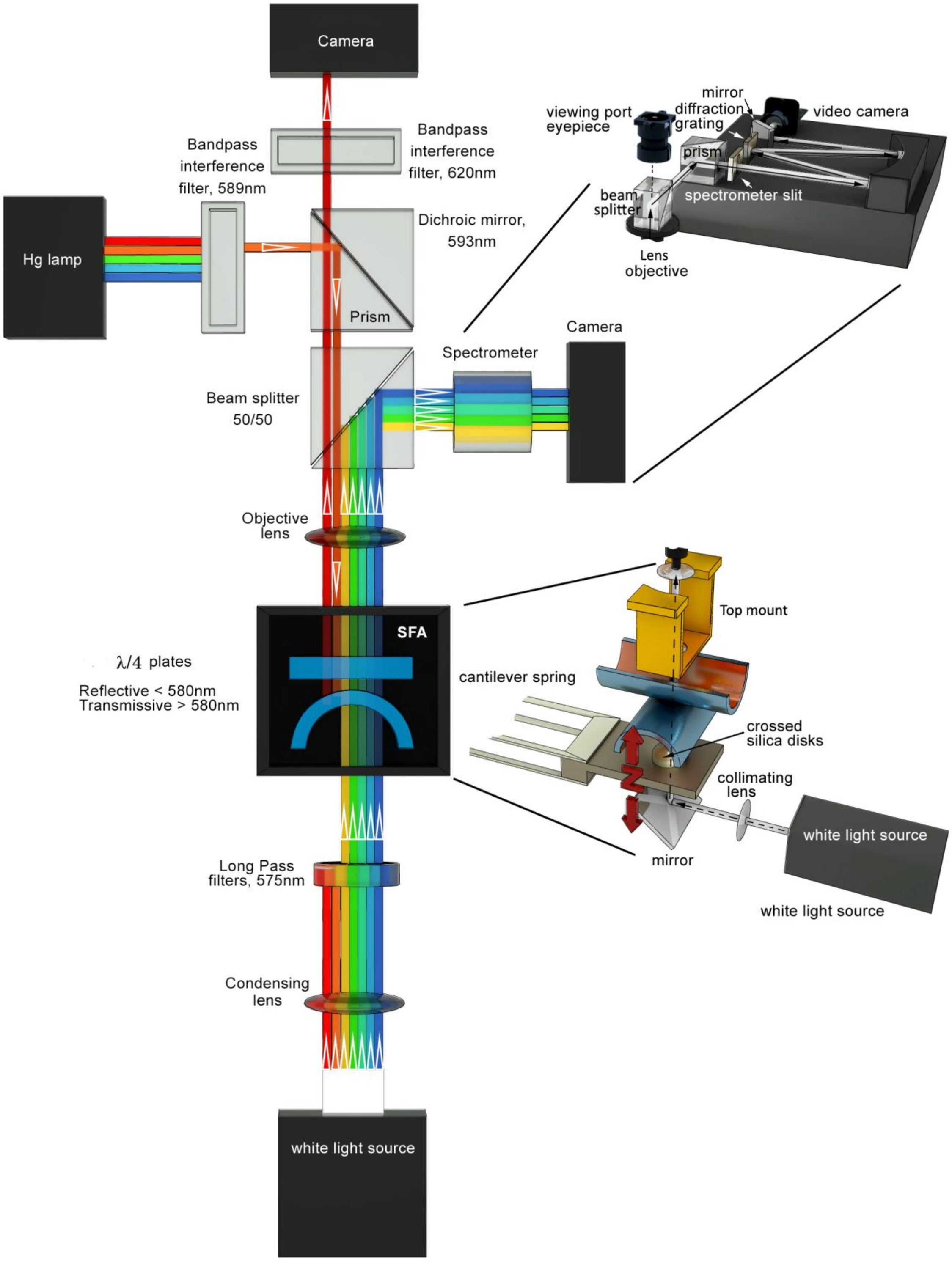

Figure 4.1 Schematic of the surface forces apparatus with fluorescence attachment (FL-SFA). The mica surfaces inside the SFA (center) are back-coated with a quarter wave plate that allows for (i) reflection below 580 nm wavelength of light used for the multiple beam interference in standard SFA measurements, and (ii) transmission above 580 nm wavelength of light used for fluorescence microscopy.

4.1.3.3 Substrate preparation

Atomically smooth mica surfaces of thickness 2-4 μm were freshly cleaved in a laminar flow hood and immediately attached to a larger and freshly cleaved backing sheet of mica for storage, which prevents the mica surfaces from contamination[18]. The back side of the mica surfaces was coated with quarter-wave plate using the Ion Beam Deposition technique. Alternating layers of Ti_2O_5 and SiO_2 with number of layers together with thicknesses as shown in 4.2B provide a wavelength specific reflective hard coating. Figure 4.2C shows the calculated reflectivity of the mica-quarter wave plate system. Incident light of wavelength below 580 nm is reflected, while above 580 nm light is transmitted through the quarter wave plate coating. The mica surfaces were glued (EPON 1004F, From Exxon Chemicals) with the quarter wave plate coating down onto cylindrical silica disks. The surfaces were placed in a cross cylindrical configuration in the SFA, which corresponds to a sphere-on-flat configuration.

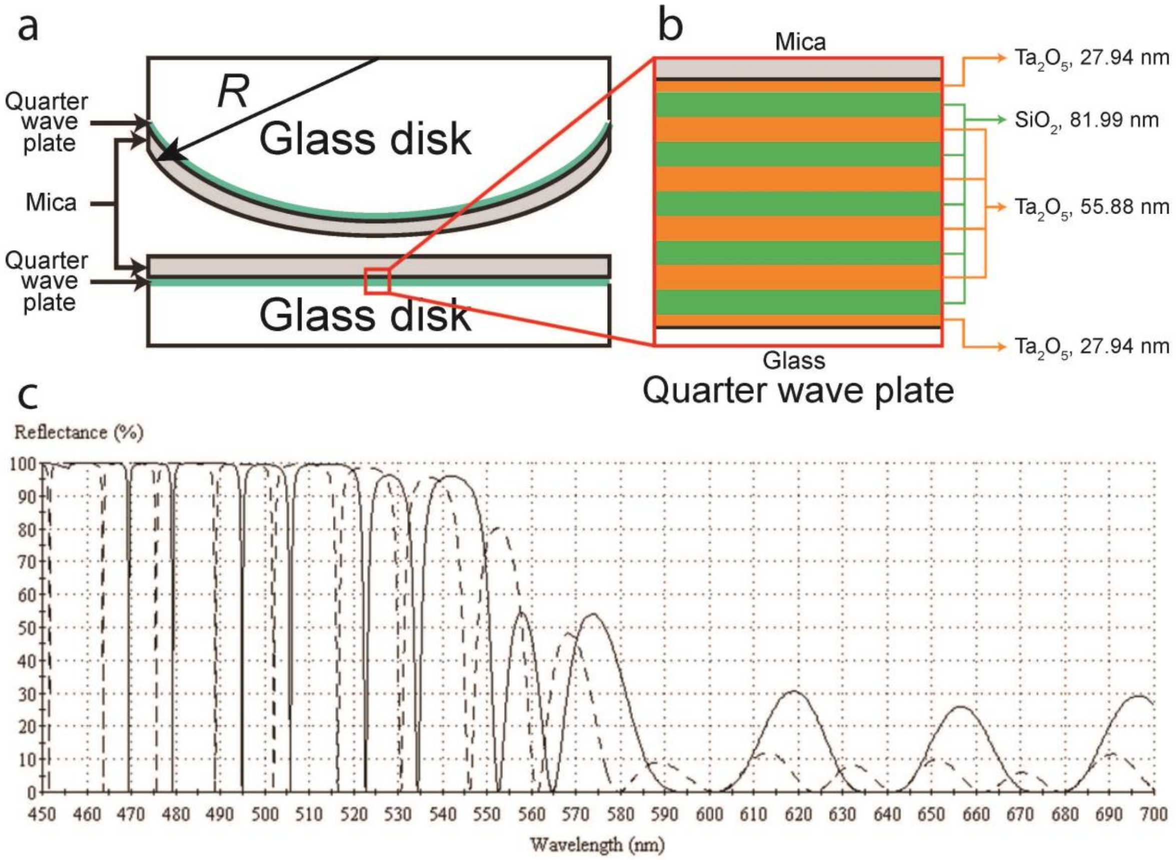

Figure 4.2 Schematic of quarter wave plate and its reflectance plot as a function of wavelength. **(a)** The mica sheets are glued with the deposited quarter wave plate down on the glue layer. **(b)** Eleven alternating layers of Ta_2O_5 and SiO_2 form the quarter wave plate, and were deposited using Ion Beam Deposition at a rate of 1.2 Å s^{-1} and 0.8 Å s^{-1}, respectively. **(c)** Using the Essential Macleod software with quarter wave plates with layer thicknesses given in **b**, the solid line shows that the reflectance through the whole system (quarter wave plate – 3 μm mica – 100 nm air – 3 μm mica – quarter wave plate) is high up to 580 nm and low below that value (and highly transmittive above 580 nm). The dotted line shows the reflectance from the same stack, but with a 10 nm air gap instead of 100 nm. The transition from reflective to transmittive at 580 nm was confirmed using an Optical Film Thickness tool (Filmetrics) and the Multiple beam interference technique.

4.1.3.4 Substrate preparation and transfer to an SFA

Lipid bilayers were deposited on the mica substrates (prepared as above), using the Langmuir-Blodgett (LB) deposition technique[19] at room temperature. First, the prepared mica surfaces were dipped into MilliQ water using a dipper attached to the LB trough. The air-water interface was carefully cleaned with a suction pipette to remove any existing dust particles at the interface. As a first layer, 100 μl of 1 mg ml^{-1} DPPE solution was slowly spread onto the air-water interface and the solvent was allowed to evaporate for 15 minutes. Starting from a total area of ~755 cm^2, the DPPE monolayer was compressed slowly (10 cm^2 min^{-1}). After reaching the target surface pressure, Π = 35 mN m^{-1}, which gave a molecular area of A=42 $Å^2$ (Fig. 4.3), the mica surfaces were raised at 1 mm min^{-1}. After the first monolayer deposition, the substrates were stored in vacuum for 12 hrs. Having the solid-like DPPE as the supporting layer is advantageous as follows: (i) It eliminates the long range Helfrich undulation force which may affect distinguishing between the other forces (e.g., electrostatic, steric, hydrophobic); (ii) it greatly reduces the mobility of the free (unstressed) lipid domains (L_o) which is advantageous for focusing only on the lipid domains at the contact, and (iii) inter-leaflet domain coupling can be excluded since the DPPE monolayer at room temperature is in the solid phase, and also not expected to phase separate. As a second layer, 100 μl of 1 mg ml^{-1} 1:1:1 (mol/mol) DOPC:BSM:CHOL+1 wt% TR-DHPE mixture was spread on to a previously prepared buffer. The deposition conditions and compression and dipper velocities for the second (outer) DOPC:BSM:CHOL monolayer were the same as for the supporting (inner) DPPE monolayer except that the dipping direction was reversed and the target surface pressure was Π =30 mN m^{-1} (A=41 $Å^2$ per molecule, Fig. 4.3B). After the deposition, without exposing the surfaces to air, the surfaces were placed into small glass Petri dishes filled with buffer. The Petri dishes were transferred to the SFA chamber which was filled with degassed saturated lipid solution (buffer in contact with lipid crystals for 12 hrs, and degassed 2-3 hrs with a vacuum pump), and the surfaces were mounted to upper and lower disk holders for the experiments.

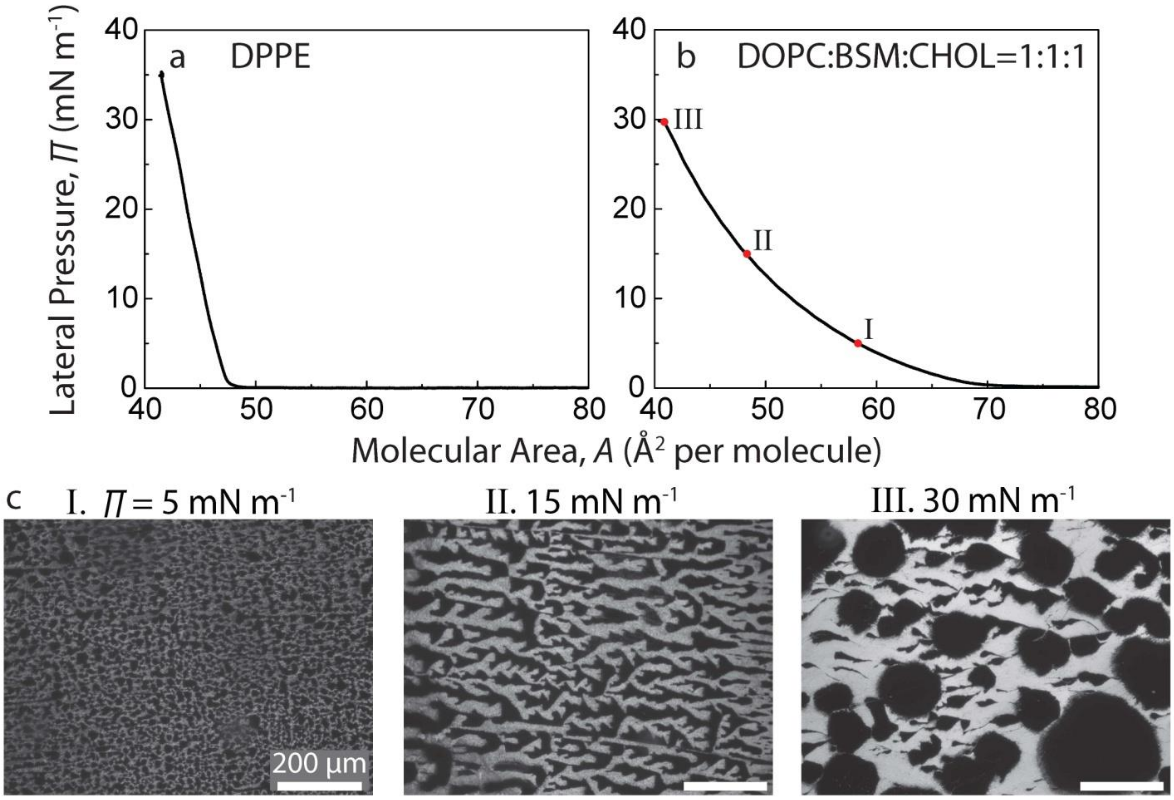

Figure 4.3 Lateral pressure (Π) - Molecular Area (A) isotherm of (**a**) DPPE, and (**b**) DOPC:BSM:CHOL = 1:1:1 mixture. (**c**) Fluorescence images showing lipid domains in DOPC:BSM:CHOL=1:1:1 mixture which was LB deposited at three different pressures (5, 15 and 30 mN m^{-1}) on to DPPE monolayer.

4.1.3.5 Fluorescence Surface Forces Apparatus (FL SFA) experiments

The force runs were performed statically using a fine control motorized micrometer, with step sizes of 2-3 nm and equilibration time of 5-10 seconds at each point. During the high compression experiment, after approaching surfaces to an F/R value of 8 mN m^{-1} with a fine control motorized micrometer, a medium control micrometer was used to compress the surfaces even further (30 µm, which corresponds to F/R=1150 mN m^{-1}). During the separation after high compression, the medium control micrometer was used to separate the surfaces and measure adhesion force. Force runs were performed in the order as mentioned in the main text, followed by four or more repeat experiments (see Figures. 4.5, 4.8 and 4.10) with different bilayers and/or contacts. Fluorescence imaging was performed simultaneously with force runs, especially focusing on the images before compression, right after compression, during hemifusion, and after separation.

During the waiting time (under compression), FECO and fluorescence images are continuously monitored (when drastic fast changes in the bilayer images are observed; Fig. 4.11), or intermittently imaged every 30-60 min (when slow changes are observed). Optimized fluorescence images required 5-10 seconds of exposure time. During the time *between* imaging, the mercury light for fluorescence imaging and white light for FECO imaging was blocked to protect the fluorophore from photobleaching. All experiments were performed at room temperature.

4.1.4 Results

4.1.4.1 Lipid domain visualization in the FL SFA

Figure 4.4A shows the schematic of the bilayer substrates used for the experiments. Briefly, asymmetric lipid bilayers were deposited onto freshly cleaved mica surfaces using Langmuir Blodgett (LB) deposition (see methods). 1,2-dipalmitoyl-*sn*-glycero-3-phosphoethanolamine (DPPE) was deposited onto mica as a supporting first monolayer (Fig. 4.3A). As a second layer, a 1:1:1 mixture of 1,2-dioleoyl-*sn*-glycero-3-phosphocholine (DOPC), Brain sphingomyeiln (BSM), and cholesterol (CHOL), with a trace amount (1 wt%) of Texas Red® 1,2-Dihexadecanoyl-sn-Glycero-3-Phosphoethanolamine, Triethylammonium Salt (TR-DHPE), was deposited onto the DPPE monolayer (Fig. 4.3B), and readily forms lipid domain structures (Fig. 4.3C).

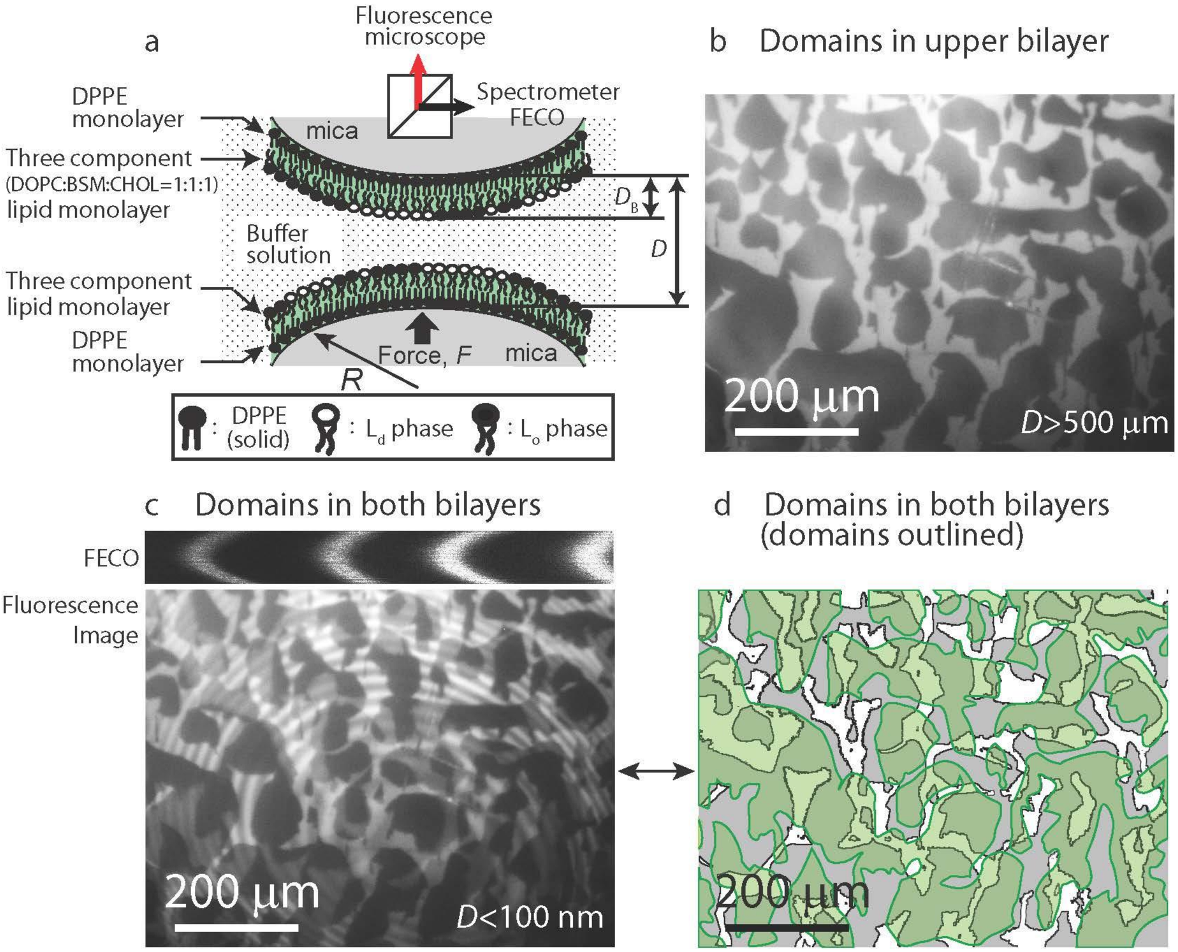

Figure 4.4 Schematic of experimental setup and obtained lipid domain images. (**a**) Two asymmetric bilayers deposited on mica surfaces using LB deposition technique, and (**b, c, d**) images of lipid domains obtained with FL-SFA. (**b**) Lipid domains of only upper bilayer, (**c**) lipid domains in both bilayers, and (**d**) outlined and shaded lipid domains.

Using the FL-SFA, bilayers containing lipid domains were imaged inside the SFA (Fig. 4.4 and 4.5). When the bilayers are positioned far apart (mica-mica separation distance *D*>500 μm), only the upper bilayer is visible (Figure 4.4B), because the lower bilayer is out of focus. The dark regions indicate the liquid-ordered phase (L_o) of lipid bilayers, conventionally referred to as lipid domains, which are rich in BSM and cholesterol[20,21]. The bright regions, where TR-DHPE is selectively localized, are in the liquid-disordered phase (L_d) of lipid bilayers and rich in DOPC[20,21]. Non-circular and large domains are observed, while others observed circular and smaller domains in similar systems[22,23]. The irregular domain shapes observed here are primarily due to the presence of calcium ions in the subphase during the LB deposition, which are known to bind strongly to the bilayer, induce phase separation, presumably make larger and irregularly shaped domains, and also lower the energy barrier to membrane fusion[24,25]. The domain size and shape at different lateral pressures (Π=5, 15 and 30 mN m^{-1}) are shown in Figure 4.3. When the bilayers are positioned closer to each other (D<5 μm), lipid domains (L_o) in both bilayers are observed (Fig. 4.4C) along with Newton's interference rings. Here, dark, grey, and white regions indicate domain-domain overlap between upper and lower bilayers (L_o-L_o), isolated domains only in one bilayer (L_o-L_d), and no domains in both bilayers (L_d-L_d), respectively. By comparing the images of the upper bilayer (Figure 4.4B) and both bilayers (Figure 4.4C), domains (L_o) in the lower bilayer can be identified as well (Figure 4.4D).

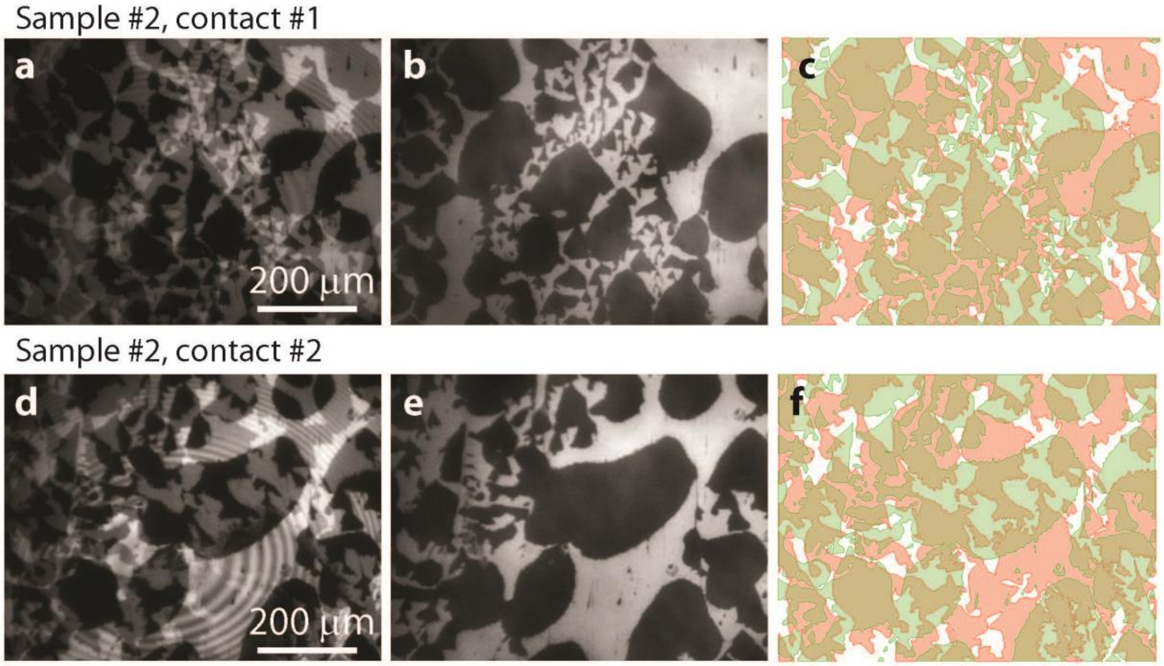

Figure 4.5 Domains in bilayers (repeat experiments); (**a, d**) overlapped domains, (**b**, **e**) domains in upper bilayer, and (**c**, **f**) distinctively pseudo-colored domains (upper domains as green, and lower domains as red). The ring formations observed in **a** and **d** are Newton's rings, where the center of the rings is the point of closest approach between the two curved surfaces.

4.1.4.2 Force and thickness measurements between hemifusing bilayers

Interaction forces (F/R) between the bilayers were measured as a function of separation distance (D) with simultaneous fluorescence imaging (Figure 4.6). Three distinct force runs (FRs) were performed where the bilayers were brought into contact under low compression (F/R=8 mN m^{-1}) and then separated after a contact time (t_c): (i) Force Run 1 (FR1): t_c=0 min, (ii) FR2: t_c=19 hrs, and (iii) FR3: t_c=0 min, but at a previously hemifused contact region.

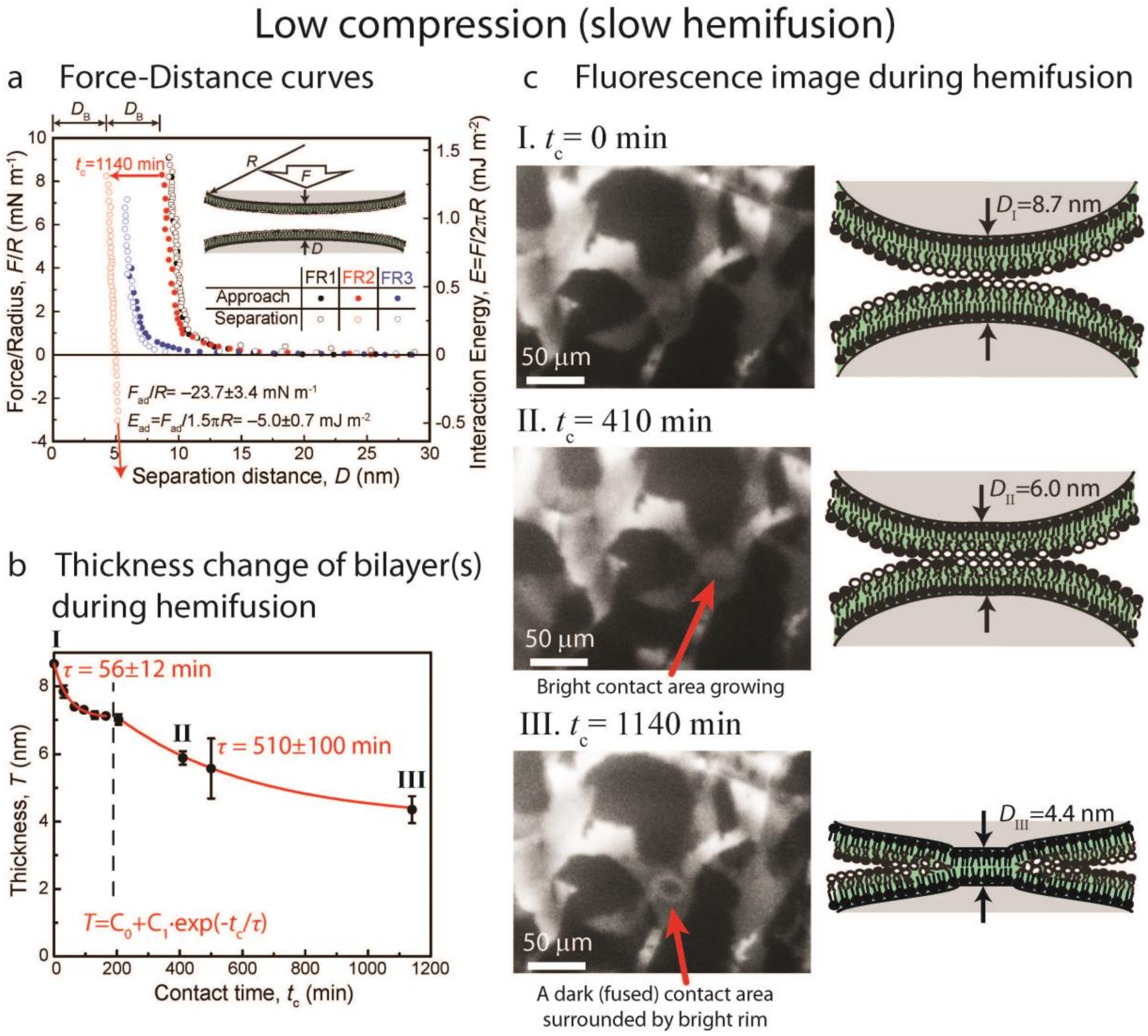

Figure 4.6 Low compression SFA results. (**a**) Force distance (*F*-*D*) curve measured between two bilayers performed under low compression (F/R=8mN m^{-1}). The error value is the standard deviation from the repeats of at least four experiments performed with different bilayers and contacts. (**b**) The bilayer thickness change, during *slow* hemifusion of two bilayers during a contact time of 1140 min, and (**c**) lipid domain reorganization during hemifusion.

The force curve (FR1) shows no hysteresis between approach and separation, and a steric (hard) wall thickness (D at F/R=8mN m^{-1}) similar to the thickness, T, of two bilayers ($T=2D_B$). The approach run of FR2 is similar to FR1 with the same steric hard wall thickness; however, during 19 hrs of contact, *slow* hemifusion of the bilayers is observed. The thickness of two bilayers ($T=2D_B$=8.7 nm) decreases down to one bilayer thickness ($T=D_B$=4.4 nm) over time (Figure 4.6B). The thickness decrease was fitted with an exponential decay equation, $T=C_0+C_1\cdot\exp(-t_c/\tau)$ where C_0 and C_1 are constants and exhibits two different regimes (Figure 4.6B),. In the first regime ($t_c<200$ min), the thickness decreases with a characteristic time, τ, of 56±12 min (± values are the standard deviation of at least three different replicates), while the second regime ($t_c>200$ min) has τ =510±100 min. The first regime is governed by the compression and thinning of the outer monolayer, while the second regime is likely related to the hydrophobic interaction and hemifusion of the lipid bilayers.

The approach curve (FR2) was fitted to a previously developed interaction potential between two bilayers[13], which includes electrostatic, Van der Waals, and hydrophobic interaction potentials (Fig. 4.7). Comparison of the theoretical model with previous work indicates that bilayer thinning and hydrophobic interactions lead to fusion[13]. Separation after slow hemifusion of the bilayers leads to an adhesion force of $F_{ad}/R=-24\pm3$ mN m^{-1}, which can be converted to adhesion energy using the Johnson-Kendall-Roberts (JKR) model[26,27], $W_{ad}=F_{ad}/1.5\pi R=-5.0\pm0.7$ mJ m^{-2}. The inter-leaflet hydrophobic attraction energy is much smaller compared to the expected value for fully hydrophobic surfaces –100 mJ m^{-2} [28], which is due to segregation of curvature-favoring lipids (i.e., DOPC) at the boundaries of the stalks, as discussed later. After FR2, a third FR on the same contact revealed that the steric hard wall was shifted down from 8.7 to 5.6 nm, slightly larger than the thickness of a single bilayer. However, during separation, no adhesion force was measured, indicating that lipid molecules partially mended the damaged bilayers.

4.1.4.3 Theoretical analysis of hemifusion

As measured previously[13,14], hemifusion occurs when the hydrophobic core of the bilayer is exposed, causing attractive hydrophobic forces to overwhelm repulsions due to electrostatics and steric forces. Therefore, the theoretical analysis presented here uses equation 4.1 shown below that includes contributions from elastic deformations of the membrane, hydrophobic, electrostatic, and steric-hydration interactions, which was previously derived for light-responsive bilayers[13].

$$W_{\text{total}} = 2\gamma_i \frac{{a_0}^2}{a(d)^2} - 2\gamma_i - 2\gamma_i \left(1 - \frac{a_0}{a(d)}\right) e^{-d/D_{\text{H}}} + \frac{C_{\text{ES}}}{a(d)} e^{-\kappa d} + \frac{C_{\text{SHR}}}{a(d)} e^{-d/D_{\text{SHR}}} \quad \text{(Eqn. 4.1)}$$

This equation is derived fully in previous work, but briefly, the first term accounts for the elastic bending energy of the membrane, the second term is the reference state energy at D → ∞, the third term is the hydrophobic attraction, the fourth term is the electrostatic repulsion, and the final term is the steric hydration repulsion. In these experiments, representative values are used for the equilibrium headgroup area, a_0 = 50 Å^2, interfacial tension γ_i = 50 mJ m^{-2}, hydrophobic decay length D_H = 1 nm, and steric hydration decay length D_SHR = 1 nm. Fitted parameters are C_ES = 1.3x10^{-21} J, κ^{-1} = 2 nm, and C_SHR = 3x10^{-20} J. The area per molecule is a function of distance that arises from minimizing the energy and is calculated from

$$a(d) = a_0(1 - e^{-d/D_{\text{H}}})^{-1/2}. \quad \text{(Eqn. 4.2)}$$

The theoretical energy is calculated as a function of bilayer separation distance, *d*. The bilayer thinning is accounted for by plotting the calculated energy as a function of mica-mica separation, *D*, where $D = d + 2T$, where $T = v_0/a(d)$ and $v_0 = a_0 \cdot L_0$. Thus, the thickness of the bilayers varies as a function of separation distance, and the final hardwall has the thickness of a single bilayer.

As shown in Figure 4.7, the theoretical analysis described above quantitatively accounts for the long range and short range forces during bilayer hemifusion. The black curve shows the theoretical curve while the red points are the same experimental points shown in

Fig. 4.6. The theoretical breakthrough occurs at a distance of about D = 8.8 nm, close to the thickness of two bilayers, $2D_B$ = 9 nm. The fitted parameters are similar to those in previous work, indicating that the mechanism for fusion is likely the same, i.e., compression results in thinning and spreading of the bilayer, resulting in hydrophobic pores and hydrophobic attraction between the bilayer interiors on opposite surfaces. The measured force barrier is larger than the predicted barrier at equilibrium, reflecting that the hemifusion processes of compressing the bilayers and molecular rearrangements within the bilayer occur slowly and dynamically.

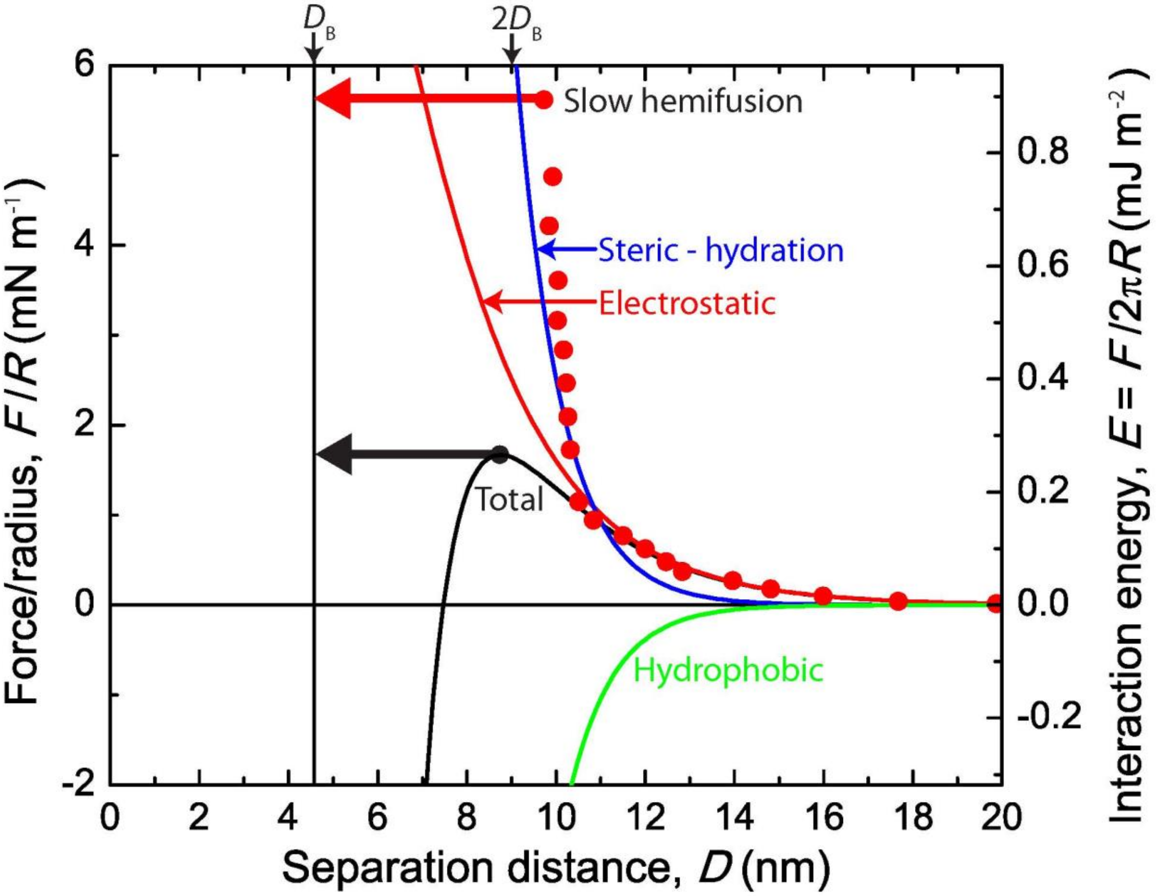

Figure 4.7 Measured F-D curve during hemifusion of bilayers (red points, also shown in main text, FR2 in Fig. 3) and theoretical analysis for hemifusion. The overall model (black curve) includes contributions from hydrophobic interactions (green curve), steric-hydration repulsion (blue curve), and electrostatics (red curve). The model predicts hemifusion at the turning point in the curve (where it changes from attractive to repulsive), indicated by the thick black arrow. The thick red arrow is the point at which slow hemifusion was measured (see Fig. 6). The theoretical curve predicts the “equilibrium” fusion barrier, while the measured barrier reflects the slow rearrangements.

After FR3, a high compression (F/R=1150mN m^{-1}) experiment was performed (Fig. 4.8) with t_c=23 hrs. High compression induces *fast* hemifusion, which was completed in 1 hr (from Figs. 4.9G to 4.9J). Immediately after compression, the central, previously hemifused region (during FR2), exhibited the thickness of a single bilayer, while the edge region had a thickness of two bilayers (Fig. 4.9G). Within 1 hr, the edge also completely hemifused to a single bilayer (Fig. 4.9J). On separation after t_c=23 hr, W_{ad}=–22.9 mJ m^{-2}(F_{ad}/R=–108 mN m^{-1}) was measured; still smaller than the expected value of –100 mJ m^{-2} [28], but similar to previously measured W_{ad} of –20 mJ m^{-2} between two hemifused trans-azobenzene trimethylammonium bromide (azoTAB) bilayers[13]. To check whether the hemifusion of a pristine bilayer (which was not fused before) also initiates from the center of the contact, we repeated the high compression experiment without an initial low compression (Fig. 4.10); again, hemifusion started at the center. This behavior indicates that hemifusion initiates because of the maximal local pressure at the center of the JKR contact. The measured adhesion energy was also similar to what was measured in FR4 (Fig. 4.8).

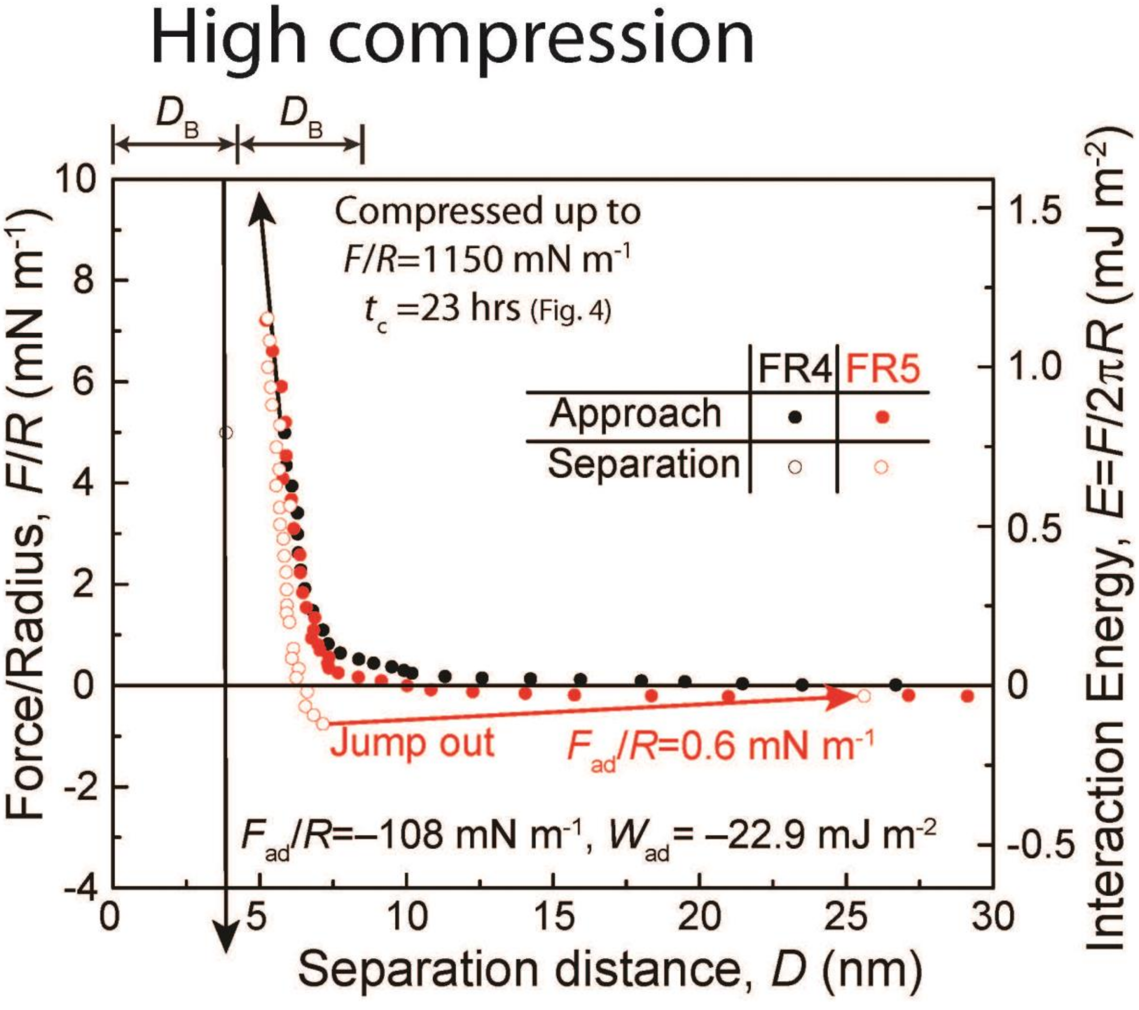

Figure 4.8. High compression induced hemifusion (FR4) and consequent force runs (FR5) performed after FR3 (Fig. 4.6A). Hemifused bilayers resulted in adhesion energy, W_{ad}=-22.9 mJ m^{-2}.

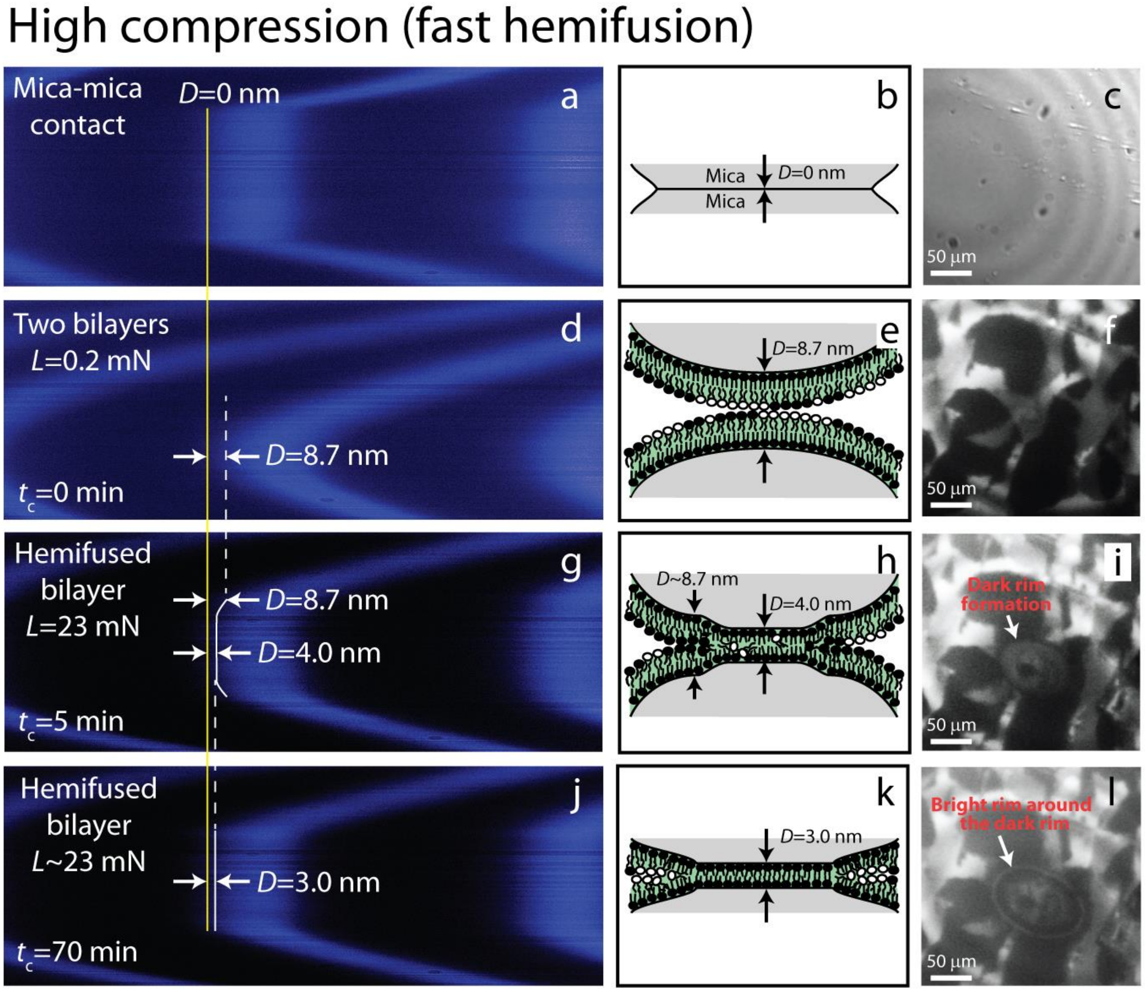

Figure 4.9 Simultaneous monitoring of the FECO (**a, d, g, j**), normal optical microscope showing Newton's rings **(c)**, and lipid domain localization (**f, i, l**) using FL-SFA before and during the contact time of FR4 (see Fig. 4.6B), and their schematics (**b, e, h, k**). (**a**, **b**, **c**) bare mica-mica contact; (**d**, **e**, **f**) two bilayers before FR2; (**g, h, i**) hemifused bilayers right after high compression; and (**j, k, l**) hemifused bilayers at t_c~70 min.

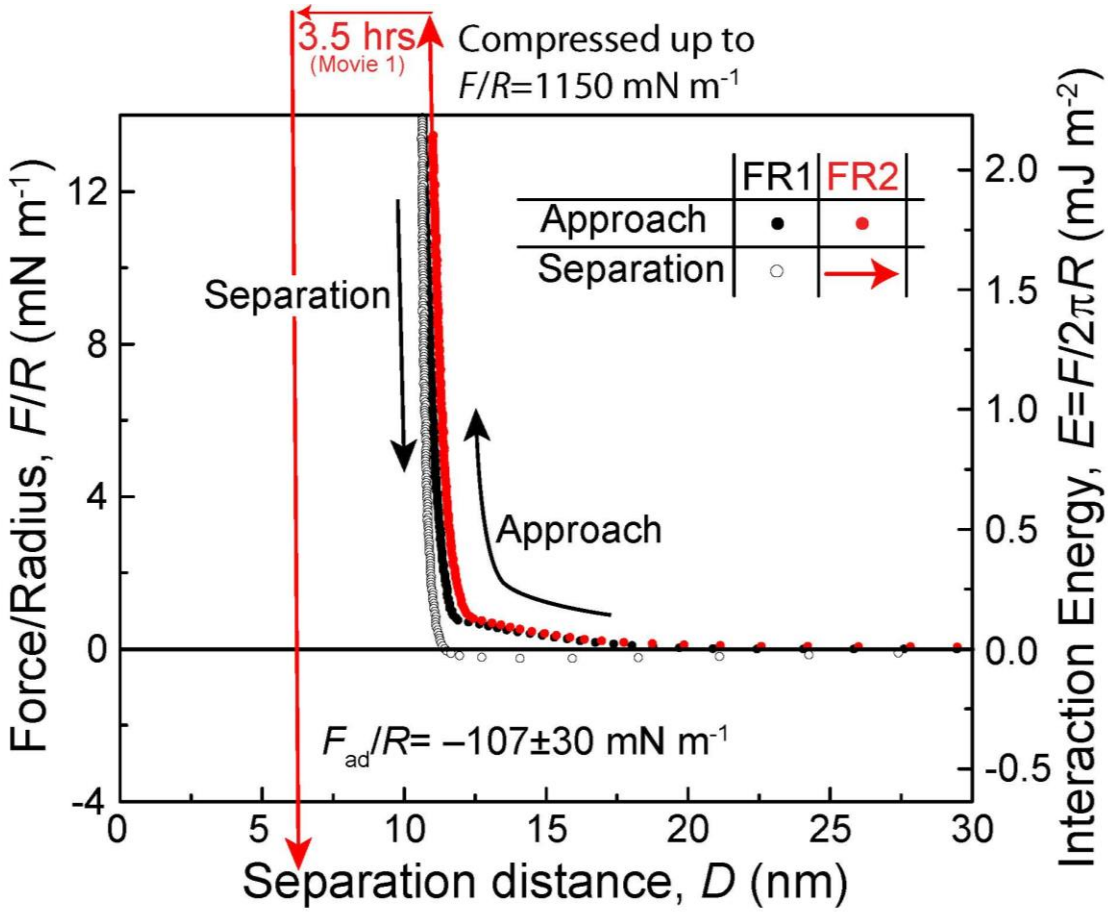

Figure 4.10 High compression (FR2) control experiment *without* the addition of fluorophores and without the initial hemifusion due to low compression. Similar force curves were observed as in Figure 4.6A except that there is hysteresis between approach and separation possibly due to the control experiment being performed under dynamic loading and unloading conditions.

4.1.4.4 Lipid domain rearrangements during hemifusion

From the initial membrane-membrane contact to the complete hemifusion of lipid bilayers, significant reorganization of lipid domains (L_o) was observed as displayed in Figures 4.6C, 4.6F, 4.6I, and 4.6L. Both low and high compression displays similar domain reorganization behavior, although the time scale of hemifusion is different. The reorganization of lipid domains (L_o) during high compression was investigated in detail (Fig. 4.11), and can be summarized as follows:

(i) First, the L_o phase is depleted from the contact (in at least one bilayer), rapidly diffusing out and forming a dark (L_o-L_o) rim surrounding the bright (L_d-L_d) and gray (L_d-L_o) contact and also slowly disappearing by lipid molecules mixing with the L_d phase. The average L_o phase disappearance rate was ~100 □m^2 min^{-1} (see Fig. 4.12A) after applying a constant load (L= 23 mN) and at t_c=14 min, the L_o phase was fully depleted from the contact in at least one bilayer.

(ii) The hemifusion of two lipid bilayers initiates near the center of the contact, where the stress is the highest and the two L_d phases (L_d-L_d, which has the lowest energy barrier for fusion) were in contact. The hemifused region reveals itself as a dark spot inside the contact, which is surrounded by a bright (L_d-L_d) rim.

(iii) The hemifused area propagates and grows logarithmically with t_c (see Fig. 4.12B), to the size of the initial contact (or even slightly larger due to higher adhesion), which results in completely hemifused bilayers. The final image shows the dark ellipsoidal (or circular) contact with a bright (L_d-L_d) rim surrounding it.

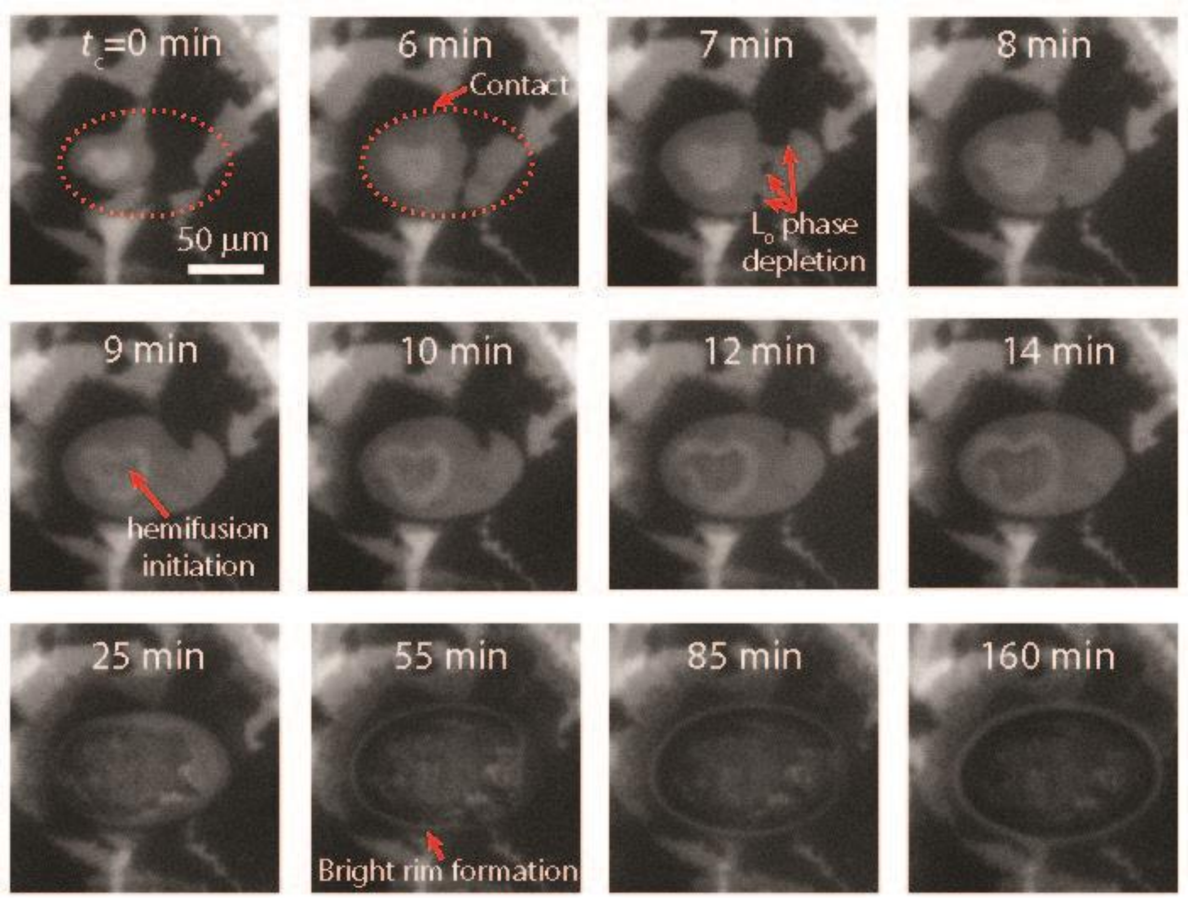

Figure 4.11 Fluorescence image of a contact (Sample #2, contact #1 Figure 4.5) as a function of time, immediately after high compression (F/R=1150 mN m^{-1}).

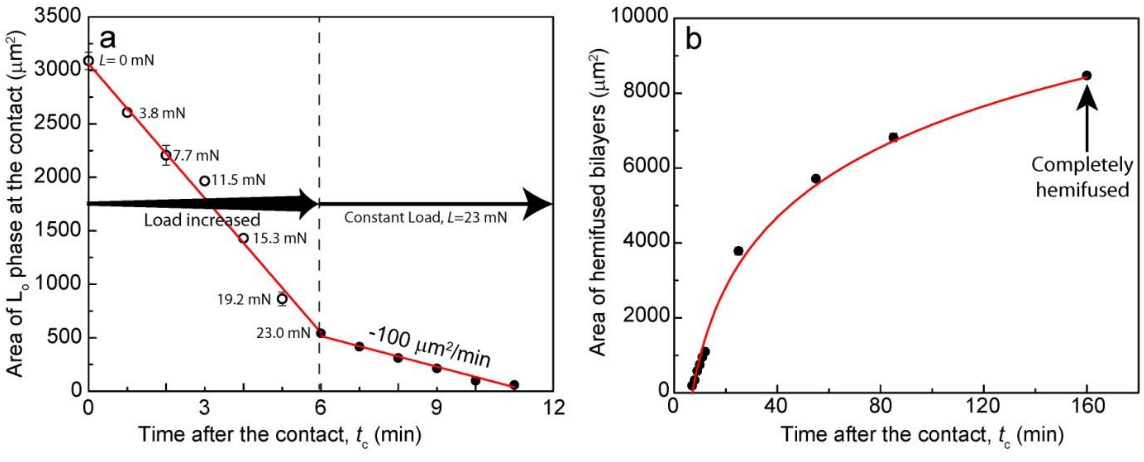

Figure 4.12 Area change in (a) L_o phase and (b) hemifused bilayers with contact time (t_c), analyzed from Figure 4.11 Open circles indicate the load increasing regime, and closed circles indicate constant load regime.

4.1.5 Discussion

Under low compression, hemifusion took almost 19 hrs to complete, while under high compression the bilayers hemifused in 2.5 hrs (1 hr for the previously fused bilayers, Fig. 4.9; and 2.5 hrs for the pristine bilayers, Fig. 4.11). The dynamics of domain rearrangements contribute to slow hemifusion. Localization of the L_d phase at the contact lowers the energy barrier for hemifusion, due to a larger area per molecule exposing more hydrophobic groups[13,14]. The rate of the L_o phase depletion is proportional to the applied load. Nevertheless, the hemifusion processes here are much slower than *in vivo* during membrane trafficking which takes milliseconds to minutes[10]. The difference in the time scale of fusion originates from the differences in the energy barrier to fusion, which is significantly affected by the membrane curvature diameter (centimeters vs. tens of nanometers), the mobility of lipids (supported vs. free-standing), and the temperature (room temperature vs. body temperature).

The L_d phase, which forms within 2.5 hrs at the edge of the stalk, as indicated by the bright rim in Fig. 4.11, is stable (or at least metastable) for more than 12 hrs, so long as the bilayers are kept under pressure in the hemifused state, i.e. not detached from each other. If the bright rim observed after the hemifusion was just a pile-up of lipids (which includes dye containing lipids), the thick pile-up would be easily observable as a deformation of FECO fringes. However, the FECO fringes show no noticeable deformation (Fig. 4.8J), thus we conclude that the bright rim is indeed a selective localization of the L_d phase. Previous studies on lipid membranes[20,29] have shown that BSM-rich membranes (L_o) have a higher bending rigidity compared to the DOPC-rich membranes (L_d). In order to lower the bending energy, the L_d phase is enriched in high-curvature membrane regions, as observed by the formation of the bright rim around the edge of the contact region (Fig. 4.11). When the hemifused bilayers are separated and relaxed, the bright L_d phase rim becomes delocalized and disappears (Fig. 4.13), providing further evidence that the bright L_d phase rim stabilizes the energetically unfavorable stalk edge.

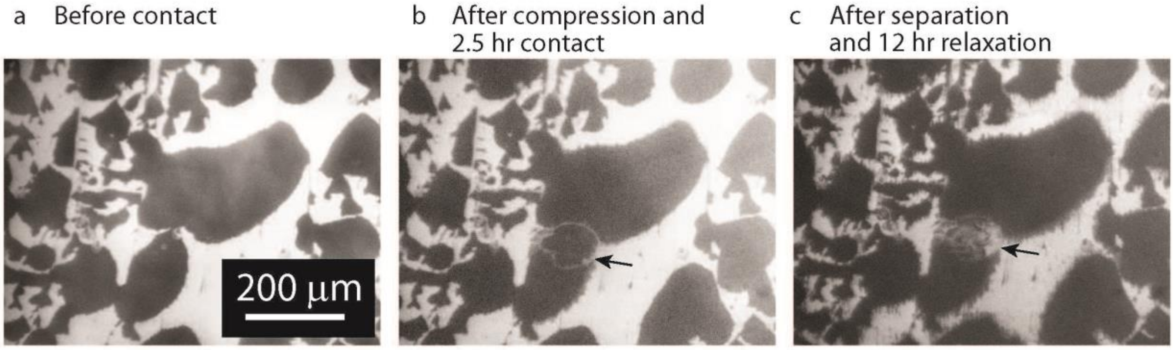

Figure 4.13 Domains at the upper surface of Sample #2, contact #2, (**a**) before compression, (**b**) after 2.5 hr compression (note the contact near the center of the image indicated with arrow has dark – L_o state with a white rim – L_d state), and (**c**) after 12 hr relaxation showing rearrangement of the previous contact area and roughening of other domain boundaries.

Here, using the FL-SFA, domain reorganization has been imaged in real time during hemifusion. The migration of the L_d region to the edge of the contact zone, combined with the small measured values for W_{ad}, show that the domains (L_o) rearrange into their lowest energy state during fusion. The fusion rate (and rate of rearrangement of the domains) is much faster at larger applied pressures, suggesting that the extra energy input into the system activates faster mixing of the leaflets. These results highlight the role and molecular mechanisms of lipid domains (L_o) during hemifusion of model membranes, indicating that domains can rearrange to decrease the energy barrier and increase the rate of fusion in membrane processes.

The use of the FL-SFA can be extended further to monitor dynamic transformations in systems where lipid domains are likely or known to occur (including pathological biological membranes) and gather previously unobtainable fundamental insights. In addition to model membrane systems, the FL-SFA has a wide range of potential applications for studying dynamic rearrangements/adsorption and forces of various interacting/non-interacting materials during and after confinement. These materials could include surfactant mono- and bi-layers, biomolecules, colloidal particles, nanoparticles, polymers, and smart materials. In these natural and engineered systems, close proximities and dynamic changes often occur, which can now be studied in greater detail using the FL-SFA.

4.2 Future Directions of the Fluorescence SFA

The combination of the traditional SFA with fluorescence microscopy yields uncharted territory in the field of interfacial science. The new ability to visualize lateral (in-plane) distribution and rearrangements while measuring forces and distances between surfaces in confinement leads to endless possibilities of systems to study and insight to generate. Although the fluorescent SFA was successful in coupling traditional SFA and FECO measurements with fluorescence microscopy, the entire setup was cumbersome with sensitive optical alignment and complex operability. To make the setup easier to operate and yield higher spatial resolution, a system needed to be developed that incorporated pre-aligned optics and multiple ports for splitting the light path to simultaneously capture FECO and fluorescent images. Thus, we designed and built a miniature SFA that can be mounted onto an optical microscope as seen in Figure 4.14. In this setup, all optical components are aligned inside the microscope, and the light beam can easily be filtered and split to different ports: (1) to the spectrometer to perform FECO measurements and (2) to the CCD camera that can capture images of the fluorescently excited molecules.

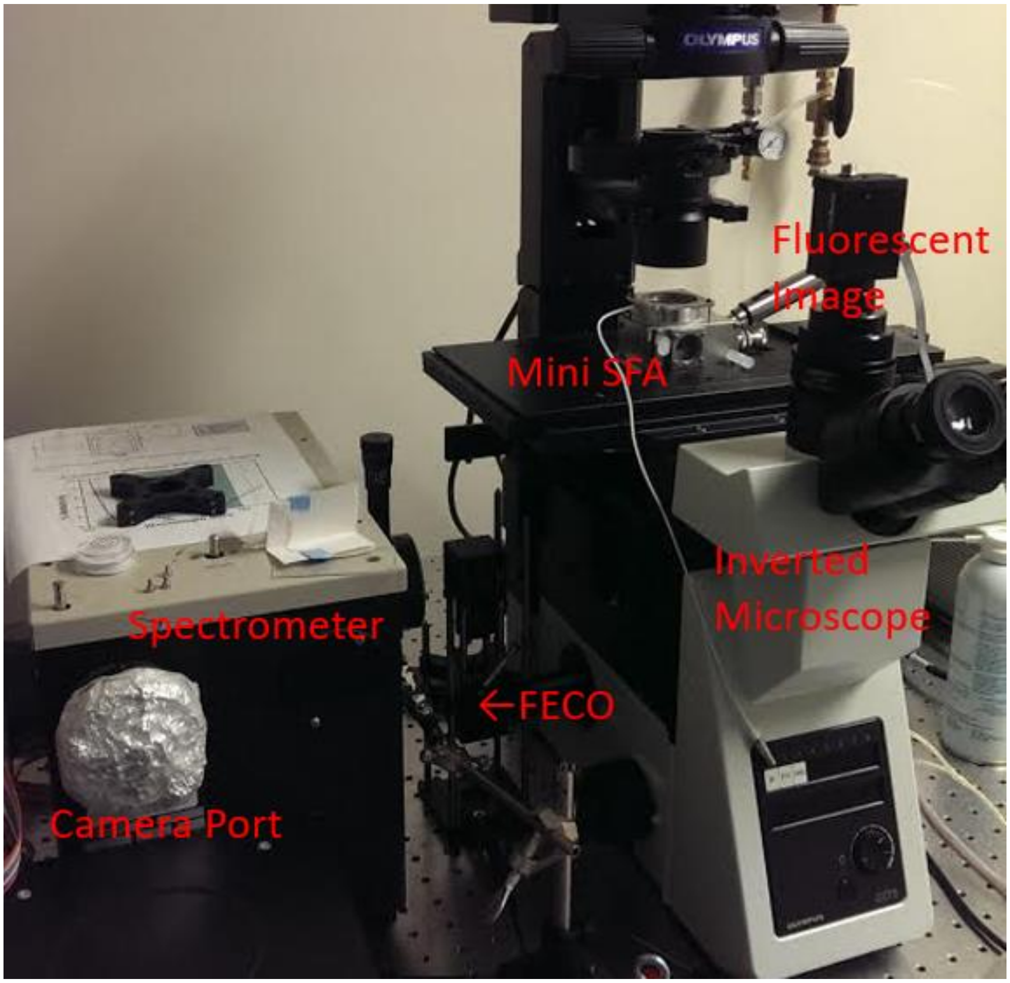

Figure 4.14 Fluorescent SFA setup. The miniature SFA is mounted on an inverted microscope equipped with fluorescence with viewing ports to both a spectrometer for FECO imaging as well as a CCD camera for fluorescence imaging.

4.2.1 Design Considerations and Objectives

Three separate characterization techniques are simultaneously combined in the miniature fluorescent SFA. First, normal optical and interference fringes of equal chromatic order (FECO) imaging is required to measure the separation distance between surfaces, the area of contact between the two surfaces, and to visualize real time deformations, adsorption, or desorption of molecules on the surfaces with angstrom scale resolution. Second, fluorescence microscopy is required to characterize the size, shape, and density distribution, and to measure diffusion and redistribution of confined molecules (or other species) between or on each surface. Third, normal and lateral displacement and thus force measurements of the surfaces must be included to allow for 3-D force mapping of interactions including adhesion, repulsion, and friction/lubrication between the surfaces in study.

Miniaturizing the SFA required a few significant adjustments to be made. Most of the mechanical controls were reconfigured to house the lower surface stage with double cantilever springs. This required a full redesign of the mount, anti-backlash springs, motor, and micrometer positioning control. Other electrical connections, fluid inlet and outlet ports, sample insertion ports, and viewing windows were also optimized to enable ease of handling and access during SFA operation. Lastly, and one of the more important requirements and significant changes to previous versions of the SFA was reducing the distance between the objective and the sample to allow for shorter focal length fluorescence objectives with high spatial resolution. A schematic of the miniature SFA is shown in Figure 4.15.

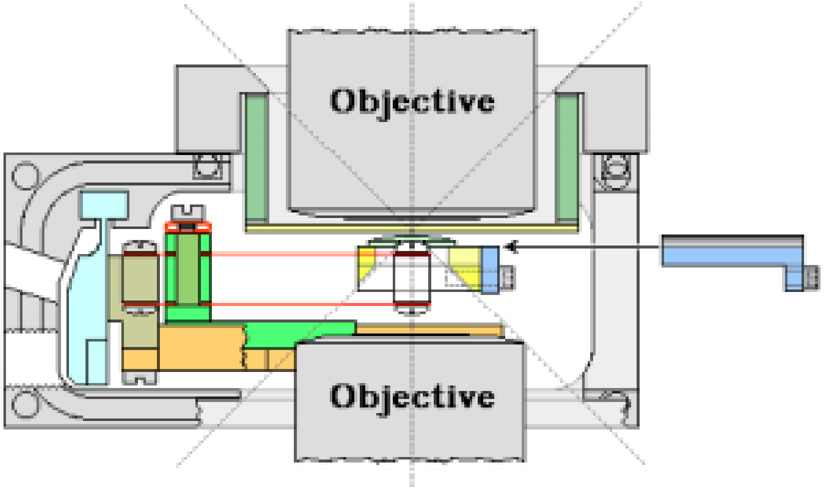

Figure 4.15 Front view of the miniature Fluorescence SFA. The miniaturization allows the device to sit on a microscope stand and dual objectives allow for simultaneous FECO (distance and force measurements) and fluorescence microscopy. The size can be compared to Figure 1.1 where all of the positional controls have been scaled down and simplified.

4.2.2 Exploring Potential Uses of the Fluorescence SFA

Building off the previous work with lipid domain rearrangement during hemifusion[30] there are many biological systems worth studying with the newly developed SFA technique. There are currently many open questions in the field regarding how cell membranes interact with each other given their complexity of lipid and intermembrane protein composition associated with different diseases as well as when introducing drug delivery vehicles such as nanoparticles or other small molecules into membrane systems.

4.2.2.1 Fluorescence SFA as a Disease Biomarker Detector

The fluorescence SFA could serve as a new approach for early detection, diagnosis, marking, and tracking (during treatment) of pathological tissue membranes, and more generally identification of membrane defects in a broad class of diseases. A new method for monitoring disease progression can be tested by measuring certain biophysical properties of membranes isolated from blood cells, plasma or other tissues. Such properties include membrane structure, adhesion, fusion or hemifusion, especially of macro- and nano- lipid domains and lipo-protein plaque morphology.

The mesoscopic morphology of membranes can be 2-dimensionally heterogeneous, where the lipid and protein molecules that constitute membranes can laterally separate into various domains, including 2-dimensional micelles, plaques, patches, and rafts[31]. The existence of membrane domains has been demonstrated and observed in a variety of biological systems[16,1,32–34]. Recent investigations have identified mesoscopic defect domains in reconstituted pathological membranes that mimic myelin sheath membranes and lung surfactant monolayers that are different from, or nonexistent in, normal, healthy membranes.

These membrane domains are ubiquitous components of biological systems and tend to be concentrated where two membranes contact, implying that the adhesion between these membranes, as well as the overall structure, is significantly impacted by specific interactions that arise from the correlations with opposing domains. Membrane domains have also been shown to play key roles in nerve and synaptic transmission, cytoskeletal organization, membrane transport, protein sorting, and cell apoptosis[6]. Aside from performing biologically useful functions, domains have also been shown to act as gateways and preferential locations for the binding of various pathological infections and disease-associated proteins, including HIV-1, and proteins associated with Alzheimer and Parkinson diseases[35].

Any significant deviations in the healthy (normal) distribution of membrane domains, including the development or growth of defect domains (for example, into plaques), would be expected to have a detrimental impact on biological processes and interactions that rely on specific nanoscopic to mesoscopic membrane morphologies. Therefore, changes in the distribution of membrane domains or interaction forces between isolated membranes could be one of the first signs of disease, a finding that would potentially have important implications for early diagnosis and monitoring treatment. However, there is a current lack of experimental techniques that can provide an unambiguous connection between changes in the nano- to meso-scopic membrane morphology and changes in membrane interaction energies/forces and functions (adhesion, structure, water gap thickness, appearance of micro- or macro-scopic lesions or other morphological changes, etc.). The miniature fluorescent SFA could bridge the connection from the nano/meso-scale to the micro/macro-scale with a combined approach of simultaneous fluorescence microscopy and force measurement and can provide more information than these separate measurements can traditionally.

The successful implementation of the mini-SFA should allow for the unambiguous establishment of the relationship between nano- to mesoscopic membrane domain morphology and other membrane-associated interactions and potentially markers of diseases. To this end its possible to use reconstituted and extracted membrane lipids/proteins (e.g., from blood cell ghosts), or actual ghost membranes, that can be deposited (by Langmuir Blodgett deposition or from solution), or 'softly-supported', on mica or other suitable polymeric or conducting substrate surfaces.

Both the nano- to mesoscale domain morphology of, and interaction forces between, healthy and diseased myelin membranes are known to differ[16,25], which leads to the hypothesis that changes in membrane morphology play a key role in the progression of certain diseases. Similar qualitative connections have been made between the presence of membrane domains and the progression of other debilitating diseases. For example, tau proteins have been hypothesized to preferentially bind at defect domains in neural membranes, also implicating defect domains and/or plaques in the progression of Alzheimer's disease. However, there has been no direct link between changes in membrane domains and changes in membrane structure (morphology) and function in any one comprehensive experimental setup, and the comparison of experiments performed using multiple different techniques leaves the relationship between membrane domains and membrane functions somewhat ambiguous.

Multiple Sclerosis (MS) and Alzheimer's Disease (AD)

Myelin is an asymmetric multilamellar membrane wrapped around the axons of the central nervous system (CNS) and consists of alternating extracellular and cytoplasmic leaflets[16]. The bilayer associated proteins, mainly myelin basic protein (MBP) and proteolipid protein (PLP), play an essential role in stabilizing and maintaining the myelin structure. The bilayers are in close contact (~3 nm separation between lipid headgroup-water interfaces), providing a low dielectric constant through the compact bilayers, which is essential for efficient and fast saltatory propagation of nerve impulses. Any structural changes of the myelin sheath in the CNS – including lesion formation, loss of adhesion, the swelling of the water gaps, vacuolization, vesiculation and complete delamination (demyelination) of the myelin sheath[16,33,17] – are signatures of several inflammatory neurological disorders.

Multiple Sclerosis (MS) is one of the most common demyelinating diseases which results in a broad spectrum of neurological symptoms such as physical and cognitive disabilities. The primary cause of MS is still under debate, and consequently early detection and treatment are difficult. In monolayer and SFA studies with model lipid membranes having the composition of 'diseased' membranes at different stages of MS, changes in lipid composition led to swelling of the water gap thickness, a reduction or complete loss of intermembrane adhesion (involving myelin basic protein), and large changes in the sizes and distributions of domains[16,17]. Recent lipidomic studies have further shown that MS leads to altered lipid metabolites in the blood stream[36,37]. These studies have shown that the lipids/lipid bilayers could be strong candidates as an early diagnostic marker detecting the impending onset and progression of MS. Lipids from blood serum, blood cell samples, or myelin could be extracted and the bilayers reconstituted on a solid substrate with a fluorescent dye. The shapes and sizes of lipid domains present in the reconstituted bilayers could be quantified and possibly correlated with progression of MS.

Similar studies could also be conducted with reconstituted membranes composed of lipids (and potentially beta-amyloid and tau proteins) from patients with Alzheimer's Disease, where plaque formation is currently the only marker for the disease, yet detectable only at advanced stages of Alzheimer's. There is also significant potential for correlating Alzheimer's progression with membrane domains from various blood cell samples and cell fragments[38]. For example, platelet membranes from Alzheimer's patients have been shown to have alterations in raft composition with increased cholesterol and ganglioside GM1[39]. These domains are likely to be evident on the macro-scale.

4.2.2.2 Using the Fluorescence SFA to Analyze Nanoparticle-Membrane Interactions

The next system discussed involves using the fluorescence SFA to understand how nanoparticles or small molecules interact when confined between biomembranes and has potential impacts in drug delivery and nanomedicine. The general aim would be to develop new and unique experimental techniques to measure, quantify, and understand the dynamic interactions among nanoparticles and biomembranes at the sub-nanometer scale and the impacts of nanoparticles on biomembrane interactions, structures, and function.

The adjustable size- and composition-dependent optical, mechanical, and transport properties of nanoparticles lead to interesting applications in medicine[40] (e.g., as drug delivery and contrast agents), friction/tribology[41] (e.g., as lubrication additives), and other diverse applications (e.g., sunscreens, solar cells, LEDs). Further development of nanoparticles for biological and biomedical applications requires a better fundamental understanding of the molecular-level interactions of nanoparticles with biological environments, some of which are depicted in Figure 4.16.

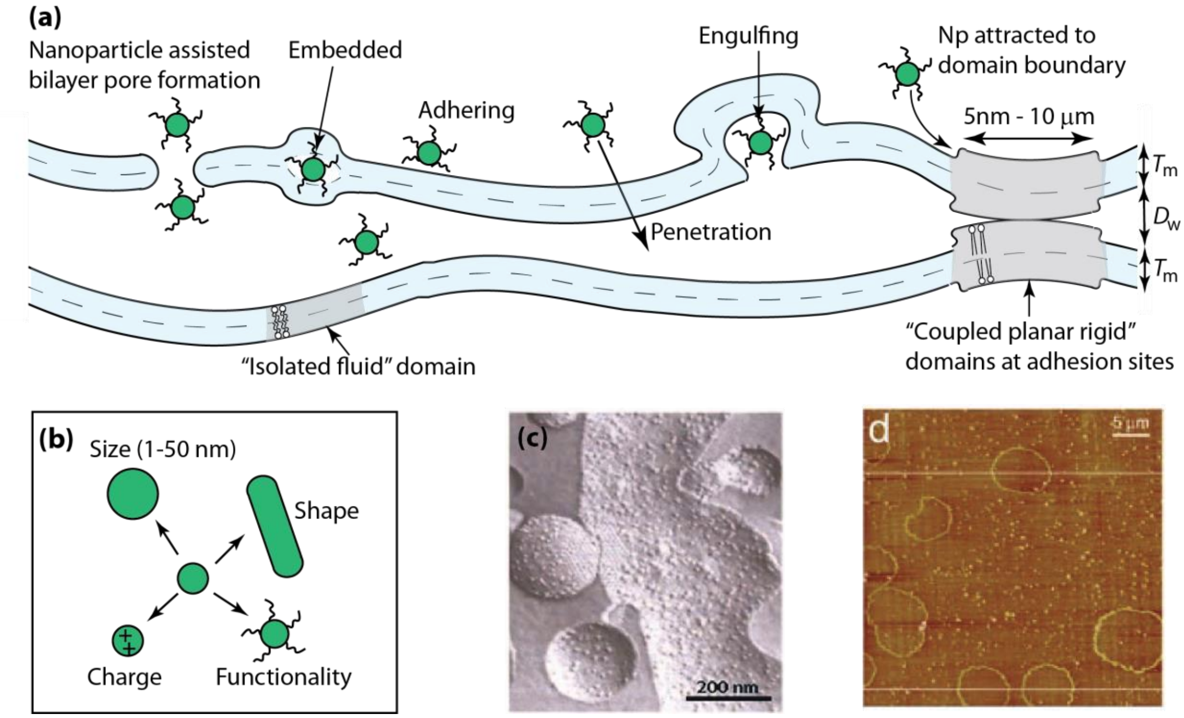

Figure 4.16 (a) Schematic of nanoparticles interacting with a lipid membrane and two membranes interacting through coupled/correlated membrane domains. The nanoparticle-membrane interactions depend on the physiochemical properties of the nanoparticles (such as (b) nanoparticle size, shape, charge, functionality) and the lipid type and composition of the membrane, as well as external parameters such as pH, temperature, ionic strength. Nanoparticles can preferentially bind to membrane features such as domain boundaries. The presence of nanoparticle inclusions and/or coupled membrane domains is expected to impact the equilibrium water gap thickness D_w and adhesion. (c) Freeze fracture cryo-electron micrograph of reconstituted plant thylakoid membranes containing lipids and the two major thylakoid proteins showing membrane domains. (d) AFM image of a myelin bilayer with Myelin Basic Protein (seen as white dots) shows that the protein, which is a biological "nanoparticle", preferentially adheres to the circular shaped domains[42]. Pickering emulsions[4] are another example of a system where nanoparticles stabilize vesicles/membranes.

The interactions of nanoparticles and their environments can differ substantially from well-understood molecular and macroscopic interactions, and depend on various physiochemical properties of the nanoparticles such as size, shape, charge, hydrophobicity or hydrophilicity[43], and surface functionality of the particles. Such interactions impact biological systems such as lipid membranes, proteins, and tissues in ways that are not fully understood theoretically or experimentally. To understand the potential beneficial and adverse[44] aspects of nanoparticles for biological and biomedical applications, a fundamental understanding of the forces that govern the distributions and interactions of nanoparticles with biomolecular assemblies is needed, as well as the nanoparticle behavior under different conditions (e.g., pH, salt concentration) and external influences (e.g., electric and magnetic field, radiation).

The current understanding of the impact of nanoparticles on biological materials has been largely empirical, and there is still much fundamental experimental and theoretical work to be done before such impacts on biological systems and environment are well-understood[45]. The nano-scale regime that the nanoparticle-membrane interactions represent falls between two more well-known regimes – the interaction forces between atoms and small-molecules and the forces between colloidal particles and extended surfaces[26]– and theoretical and experimental connections between these two regimes is currently scarce. For example, assemblies of particles in the size range of 1 – 10 nm have no gas-liquid transition, which exemplifies that there are both qualitative and quantitative differences compared to smaller molecules or larger colloidal particles (> 50 nm) which do undergo such transitions[46]. Nanoparticles have a host of other physiochemical properties that are unique to their size range, which makes them very interesting for applications in nanomedicine, optoelectronics, and diverse mechanical and electrical applications.

The understanding of the impact of engineered nanoparticles on biological material is critical for applications in nanomedicine. Despite a decade long investment of extensive research and financial support in academia and pharmaceutical companies, only a few nanomedicines are currently available. The biggest hurdle for the success of nanomedicine is described in a recent review article as: “(…) the lack of understanding and data concerning the nanoparticle fate and their behavior upon contact with biological media and cell membranes."[45]

The complexity of the nanoparticle-membrane interaction stems from the various physiochemical properties (e.g., shapes, composition, functionality) of nanoparticles, as well as the variability of membrane composition at specific biologically-relevant environmental parameters such as temperature, ionic concentration, and pH. Procedures need to be developed to find commonalities to gain a general understanding of their interactions. For example, a recent study showed that the size of introduced copper particles had a dramatic effect on membrane damage in lung epithelial cells and membrane rupturing of red blood cells (hemolysis). Copper nanoparticles were shown to be more damaging to membranes, while copper microparticles showed no such effect[47]. In contrast, CuO nanoparticles showed no negative effect on cells, which demonstrates the importance of the nanoparticle core composition. However, no complete theoretical or experimental understanding exists regarding the influence of composition, surface structure, and environmental conditions on nanoparticle-membrane interactions, especially the dynamics of such interactions.

Density and distributions of nanoparticles on membranes and of membrane features (e.g., embedded proteins, domains) are typically visualized by fluorescence microscopy, x-ray scattering, or cryo-electron microscopy (as in Fig. 4.16). None of these techniques allow for the simultaneous imaging of the nanoparticles and the membrane features and characterization of either changes in the interactions or forces (adhesion, membrane structure, water gap thickness, etc.) between membranes, or the measurement of dynamic interactions or forces among membranes and nanoparticles. Therefore, while these visualization techniques have been highly-effective for establishing the existence of membrane features, they provide no information regarding the relationship between changes in nanoscopic to mesoscopic membrane morphology due to exposure of nanoparticles and (pathological) membrane properties or functions.

Nanoparticles seek domain boundaries or can even induce domain formation[48]. Proteins bind preferentially to the boundaries of these domains, as it is believed that these domain boundaries expose more of the hydrophobic part of the bilayer which the proteins are attracted to. It's possible that hydrophobic drug-delivery nanoparticle vehicles will also bind preferentially to domain boundaries. The insights provided by analysis in the fluorescence SFA could provide new understandings of the interactions which govern nanoparticle distributions in and on lipid membranes, which will inform the rational design of new drug-delivery methods.

Currently, a qualitative relationship between nanoparticles, membrane morphology and membrane function has been implied by comparing the results from fluorescence microscopy[45], where the distribution of nanoparticles and membrane features, such as lipid domains, can be imaged, to force measurements performed on corresponding membrane systems, where differences in membrane adhesion forces, structure and water gap thicknesses can be directly observed[49]. Importantly, this *ex situ* strategy involves correlating observations obtained with totally different samples and experimental techniques where many important sample and solution conditions can vary, including: the temperature, specific sample preparation conditions, and sample histories.

Establishing *in situ* relations between changes in membrane domains due to nanoparticle exposure, adsorption, and penetration, and membrane interactions or properties will be essential for understanding the impact of nanoparticles on biological materials, such as membranes. Changes in the distributions of nanoparticles and membrane features are expected to be complex and dynamical, i.e., time varying processes where conditions external to the membranes (solution salt type and concentration, pH, temperature, external stresses applied to the membranes, etc.), the structure and compositions of the nanoparticles, and interactions from surrounding membranes are expected to play an important role. Therefore, the fluorescence SFA that combines both fluorescence microscopy and force measuring capabilities is necessary to unambiguously establish a fundamental relation between membrane morphology and interactions with nanoparticles. An example of a proof of concept experiment and typical data that can be acquired with the fluorescence SFA is depicted in Figure 4.17.

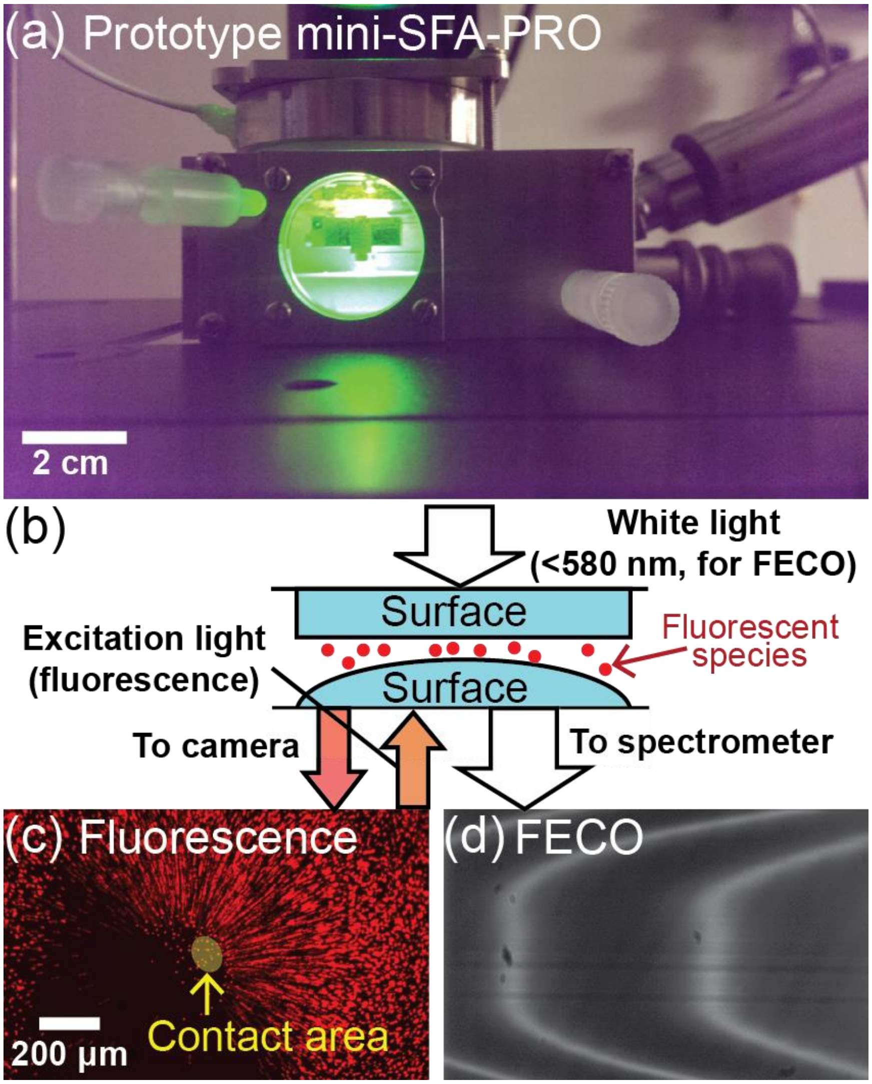

Figure 4.17 **(a)** The mini-SFA in an inverted microscope in fluorescence imaging mode for fluorescence (FL)-SFA. **(b)** Schematic illustration of a FL-SFA experiment. Orange light (589 nm) is used to excite fluorescent species, which emit at red wavelengths. Simultaneously, white light (<580 nm) is reflected between the surfaces. The transmitted light near the point of contact creates Newton's rings which yield fringes of equal chromatic order (FECO), as in a conventional SFA experiment. The combined methods enable *in-situ* **(c)** fluorescence imaging and force-distance measurements by analysis of **(d)** FECO.

References

(1) Lingwood, D.; Simons, K. Lipid Rafts As a Membrane-Organizing Principle. *Science (80-.).* **2010**, *327* (5961), 46–50.

(2) Chamberlain, L. H.; Burgoyne, R. D.; Gould, G. W. SNARE Proteins Are Highly Enriched in Lipid Rafts in PC12 Cells: Implications for the Spatial Control of Exocytosis. *Proc. Natl. Acad. Sci.* **2001**, *98* (10), 5619–5624.

(3) Salaün, C.; Gould, G. W.; Chamberlain, L. H. Lipid Raft Association of SNARE Proteins Regulates Exocytosis in PC12 Cells. *J. Biol. Chem.* **2005**, *280* (20), 19449–19453.

(4) Jahn, R.; Lang, T.; Südhof, T. C. Membrane Fusion. *Cell* **2003**, *112* (4), 519–533.

(5) Ikonen, E. Roles of Lipid Rafts in Membrane Transport. *Curr. Opin. Cell Biol.* **2001**, *13* (4), 470–477.

(6) Simons, K.; Toomre, D. Lipid Rafts and Signal Transduction. *Nat. Rev. Mol. Cell Biol.* **2000**, *1* (1), 31–39.

(7) O'Connell, K.; Martens, J. R.; Tamkun, M. M. Localization of Ion Channels to Lipid Raft Domains within the Cardiovascular System. *Trends Cardiovasc. Med.* **2004**, *14* (2), 37–42.

(8) Mahfoud, R.; Garmy, N.; Maresca, M.; Yahi, N.; Puigserver, A.; Fantini, J. Identification of a Common Sphingolipid-Binding Domain in Alzheimer, Prion, and HIV-1 Proteins. *J. Biol. Chem.* **2002**, *277* (13), 11292–11296.

(9) Lang, T. SNARE Proteins and "Membrane Rafts". *J. Physiol.* **2007**, *585* (Pt 3), 693–698.

(10) Weber, T.; Zemelman, B. V; McNew, J. A.; Westermann, B.; Gmachl, M.; Parlati, F.; Söllner, T. H.; Rothman, J. E. SNAREpins: Minimal Machinery for Membrane Fusion. *Cell* **1998**, *92* (6), 759–772.

(11) Mukai, A.; Kurisaki, T.; Sato, S. B.; Kobayashi, T.; Kondoh, G.; Hashimoto, N. Dynamic Clustering and Dispersion of Lipid Rafts Contribute to Fusion Competence of Myogenic Cells. *Exp. Cell Res.* **2009**, *315* (17), 3052–3063.

(12) Martens, S.; McMahon, H. T. Mechanisms of Membrane Fusion: Disparate Players and Common Principles. *Nat. Rev. Mol. Cell Biol.* **2008**, *9* (7), 543–556.

(13) Donaldson, S. H.; Lee, C. T.; Chmelka, B. F.; Israelachvili, J. N. General Hydrophobic Interaction Potential for Surfactant/lipid Bilayers from Direct Force Measurements between Light-Modulated Bilayers. *Proc. Natl. Acad. Sci. U. S. A.* **2011**, *108* (38), 15699–15704.

(14) Helm, C. A.; Israelachvili, J. N.; McGuiggan, P. M. Molecular Mechanisms and Forces Involved in the Adhesion and Fusion of Amphiphilic Bilayers. *Science* **1989**, *246* (4932), 919–922.

(15) Aeffner, S.; Reusch, T.; Weinhausen, B.; Salditt, T. Energetics of Stalk Intermediates in Membrane Fusion Are Controlled by Lipid Composition. *Proc. Natl. Acad. Sci. U. S. A.* **2012**, *109* (25), E1609-18.

(16) Lee, D. W.; Min, Y.; Dhar, P.; Ramachandran, A.; Israelachvili, J. N.; Zasadzinski, J.

A. Relating Domain Size Distribution to Line Tension and Molecular Dipole Density in Model Cytoplasmic Myelin Lipid Monolayers. *Proc. Natl. Acad. Sci. U. S. A.* **2011**, *108* (23), 9425–9430.

(17) Lee, D. W.; Banquy, X.; Kristiansen, K.; Kaufman, Y.; Boggs, J. M.; Israelachvili, J. N. Lipid Domains Control Myelin Basic Protein Adsorption and Membrane Interactions between Model Myelin Lipid Bilayers. *Proc. Natl. Acad. Sci. U. S. A.* **2014**, *111* (8), E768-75.

(18) Israelachvili, J. . Recent Advances in the Surface Forces Apparatus (SFA) Technique. *Reports Prog. Phys.* **2010**, *73* (3).

(19) Zasadzinski, J. A.; Viswanathan, R.; Madsen, L.; Garnaes, J.; Schwartz, D. K. Langmuir-Blodgett Films. *Science* **1994**, *263* (5154), 1726–1733.

(20) Baumgart, T.; Hess, S. T.; Webb, W. W. Imaging Coexisting Fluid Domains in Biomembrane Models Coupling Curvature and Line Tension. *Nature* **2003**, *425* (6960), 821–824.

(21) Dietrich, C.; Bagatolli, L. A.; Volovyk, Z. N.; Thompson, N. L.; Levi, M.; Jacobson, K.; Gratton, E. Lipid Rafts Reconstituted in Model Membranes. *Biophys. J.* **2001**, *80* (3), 1417–1428.

(22) Stottrup, B. L.; Veatch, S. L.; Keller, S. L. Nonequilibrium Behavior in Supported Lipid Membranes Containing Cholesterol. *Biophys. J.* **2004**, *86* (5), 2942–2950.

(23) Veatch, S. L.; Keller, S. L. Separation of Liquid Phases in Giant Vesicles of Ternary Mixtures of Phospholipids and Cholesterol. *Biophys. J.* **2003**, *85* (5), 3074–3083.

(24) Leckband, D. E.; Helm, C. A.; Israelachvili, J. Role of Calcium in the Adhesion and Fusion of Bilayers. *Biochemistry* **1993**, *32* (4), 1127–1140.

(25) Banquy, X.; Kristiansen, K.; Lee, D. W.; Israelachvili, J. N. Adhesion and Hemifusion of Cytoplasmic Myelin Lipid Membranes Are Highly Dependent on the Lipid Composition. *Biochim. Biophys. Acta - Biomembr.* **2012**, *1818* (3), 402–410.

(26) Israelachvili, J. N. *Intermolecular and Surface Forces: Revised Third Edition*; Academic Press, 2011.

(27) Johnson, K. L.; Kendall, K.; Roberts, A. D. Surface Energy and the Contact of Elastic Solids. *Proc. R. Soc. A Math. Phys. Eng. Sci.* **1971**, *324* (1558), 301–313.

(28) Meyer, E. E.; Rosenberg, K. J.; Israelachvili, J. Recent Progress in Understanding Hydrophobic Interactions. *Proc. Natl. Acad. Sci.* **2006**, *103* (43), 15739–15746.

(29) Sorre, B.; Callan-Jones, A.; Manneville, J.-B.; Nassoy, P.; Joanny, J.-F.; Prost, J.; Goud, B.; Bassereau, P. Curvature-Driven Lipid Sorting Needs Proximity to a Demixing Point and Is Aided by Proteins. *Proc. Natl. Acad. Sci. U. S. A.* **2009**, *106* (14), 5622–5626.

(30) Lee, D. W.; Kristiansen, K.; Donaldson, Jr., S. H.; Cadirov, N.; Banquy, X.; Israelachvili, J. N. Real-Time Intermembrane Force Measurements and Imaging of Lipid Domain Morphology during Hemifusion. *Nat. Commun.* **2015**, *6*, 7238.

(31) Israelachvili, J. Self-Assembly in Two Dimensions: Surface Micelles and Domain Formation in Monolayers. *Langmuir* **1994**, *10* (10), 3774–3781.

(32) Jacobson, K.; Mouritsen, O. G.; Anderson, R. G. W. Lipid Rafts: At a Crossroad

between Cell Biology and Physics. *Nat. Cell Biol.* **2007**, *9* (1), 7–14.

(33) Hollingshead, C. J.; Caspar, D. L.; Melchior, V.; Kirschner, D. A. Compaction and Particle Segregation in Myelin Membrane Arrays. *J. Cell Biol.* **1981**, *89* (3), 631–644.

(34) He, H.-T.; Marguet, D. Detecting Nanodomains in Living Cell Membrane by Fluorescence Correlation Spectroscopy. *Annu. Rev. Phys. Chem.* **2011**, *62* (1), 417–436.

(35) Simons, K.; Ehehalt, R. Cholesterol, Lipid Rafts, and Disease. *J. Clin. Invest.* **2002**, *110* (5), 597–603.

(36) Del Boccio, P.; Pieragostino, D.; Di Ioia, M.; Petrucci, F.; Lugaresi, A.; De Luca, G.; Gambi, D.; Onofrj, M.; Di Ilio, C.; Sacchetta, P.; Urbani, A. Lipidomic Investigations for the Characterization of Circulating Serum Lipids in Multiple Sclerosis. *J. Proteomics* **2011**, *74* (12), 2826–2836.

(37) Quintana, F. J.; Yeste, A.; Weiner, H. L.; Covacu, R. Lipids and Lipid-Reactive Antibodies as Biomarkers for Multiple Sclerosis. *J. Neuroimmunol.* **2012**, *248* (1–2), 53–57.

(38) Mapstone, M.; Cheema, A. K.; Fiandaca, M. S.; Zhong, X.; Mhyre, T. R.; MacArthur, L. H.; Hall, W. J.; Fisher, S. G.; Peterson, D. R.; Haley, J. M.; Nazar, M. D.; Rich, S. A.; Berlau, D. J.; Peltz, C. B.; Tan, M. T.; Kawas, C. H.; Federoff, H. J. Plasma Phospholipids Identify Antecedent Memory Impairment in Older Adults. *Nat. Med.* **2014**, *20* (4), 415–418.

(39) Liu, L.; Zhang, K.; Tan, L.; Chen, Y.-H.; Cao, Y.-P. Alterations in Cholesterol and

Ganglioside GM1 Content of Lipid Rafts in Platelets From Patients With Alzheimer Disease. *Alzheimer Dis. Assoc. Disord.* **2015**, *29* (1), 63–69.

(40) Mitragotri, S.; Stayton, P. Organic Nanoparticles for Drug Delivery and Imaging. *MRS Bull.* **2014**, *39* (3), 219–223.

(41) Kristiansen, K.; Zeng, H.; Wang, P.; Israelachvili, J. N. Microtribology of Aqueous Carbon Nanotube Dispersions. *Adv. Funct. Mater.* **2011**, *21* (23), 4555–4564.

(42) Hu, Y.; Doudevski, I.; Wood, D.; Moscarello, M.; Husted, C.; Genain, C.; Zasadzinski, J. A.; Israelachvili, J. Synergistic Interactions of Lipids and Myelin Basic Protein. *Proc. Natl. Acad. Sci. U. S. A.* **2004**, *101* (37), 13466–13471.

(43) Donaldson, S. H.; Røyne, A.; Kristiansen, K.; Rapp, M. V.; Das, S.; Gebbie, M. A.; Lee, D. W.; Stock, P.; Valtiner, M.; Israelachvili, J. Developing a General Interaction Potential for Hydrophobic and Hydrophilic Interactions. *Langmuir* **2015**, *31* (7), 2051–2064.

(44) Boczkowski, J.; Lanone, S. Potential Uses of Carbon Nanotubes in the Medical Field: How Worried Should Patients Be? *Nanomedicine* **2007**, *2* (4), 407–410.

(45) Rascol, E.; Devoisselle, J.-M.; Chopineau, J. The Relevance of Membrane Models to Understand Nanoparticles-Cell Membrane Interactions. *Nanoscale* **2016**, *8* (9), 4780–4798.

(46) Min, Y.; Akbulut, M.; Kristiansen, K.; Golan, Y.; Israelachvili, J. The Role of Interparticle and External Forces in Nanoparticle Assembly. *Nat. Mater.* **2008**, *7* (7), 527–538.

(47) Cell Membrane Damage and Protein Interaction Induced by Copper Containing nanoparticles—Importance of the Metal Release Process. *Toxicology* **2013**, *313* (1), 59–69.

(48) Montis, C.; Maiolo, D.; Alessandri, I.; Bergese, P.; Berti, D. Interaction of Nanoparticles with Lipid Membranes: A Multiscale Perspective. *Nanoscale* **2014**, *6* (12), 6452–6457.

(49) Min, Y.; Kristiansen, K.; Boggs, J. M.; Husted, C.; Zasadzinski, J. A.; Israelachvili, J. Interaction Forces and Adhesion of Supported Myelin Lipid Bilayers Modulated by Myelin Basic Protein. *Proc. Natl. Acad. Sci. U. S. A.* **2009**, *106* (9), 3154–3159.